

# **Hartmann-based wavefront sensing and multi-contrast imaging with synchrotron and laboratory sources**

Zur Erlangung des akademischen Grades eines

**DOKTOR-INGENIEURS**

von der KIT-Fakultät für Maschinenbau,  
des Karlsruher Instituts für Technologie (KIT)

angenommene

**DISSERTATION**

von

**M.Sc. Andrey Mikhaylov**

geb. in Krasnojarsk, Russland

Tag der mündlichen Prüfung:

Hauptreferent:

Korreferent:

18 Juli 2023

Prof. Dr. Jan Gerrit Korvink

Prof. Dr. Ulrich Lemmer



This document is licensed under a Creative Commons Attribution-ShareAlike 4.0 International License (CC BY-SA 4.0): <https://creativecommons.org/licenses/by-sa/4.0/deed.en>

*The setting of the book takes place in a parallel universe, all coincidences to which are  
nightmarish dreams.*

V. Pelevin



## Kurzfassung

Im Laufe der Jahre haben Methoden, die für Phaseninformationen empfindlich sind, in Wissenschaft und Technik großes Interesse geweckt und sich in Bereichen wie der Materialwissenschaft und der Medizin stetig und schnell weiterentwickelt. Die Entwicklung solcher Techniken im Bereich der harten Röntgenstrahlung verlief ähnlich wie bei der visuellen Lichtoptik, einschließlich der Entwicklung und Anpassung analoger optischer Elemente und Datenverarbeitungsstrategien, um genauere Charakterisierungen zu erhalten. Auch wenn einige Methoden, die auf Welleninterferenz beruhen, eine hohe Winkelempfindlichkeit bieten können, ist die Umsetzung solcher Techniken sehr komplex. Erhöhte Anforderungen an die Lichtquelle in Bezug auf Monochromatizität, Lichtstrom und Kohärenz, zusammen mit anspruchsvoller Mechanik, Ausrichtungsverfahren und langen Belichtungszeiten. Eine hohe Winkelempfindlichkeit könnte je nach Anwendung überflüssig sein, und lange Belichtungszeiten könnten die Anwendbarkeit einschränken. Bei der Überwachung von schnellen Prozessen, niedrigen Flussbedingungen, Vielseitigkeit und Einfachheit der Implementierung von Single-Shot-Methoden könnten daher vorzuziehen sein.

Hartmann-basierte Wellenfrontsensor-Techniken sind in der Astronomie, Atmosphärenforschung und Mikroskopie weit verbreitet. Es handelt sich um ein vielseitiges Instrumentarium, das ergänzende Informationen zu den Intensitätsmessungen liefern könnte. Die hohe Energie der Röntgenstrahlen, ihr hohes Durchdringungsvermögen und ihr niedriger Brechungsindex erfordern jedoch die Anwendung komplexer neuer Lösungen. Die modernsten Strukturierungstechniken wie 3D-Zweiphotonenlithographie, Deep X-ray Lithography und bekannte Methoden wie UV-Lithographie ermöglichen die Herstellung optischer Komponenten mit geeigneten Parametern.

In dieser Arbeit wird die Implementierung des Shack-Hartmann-Wellenfrontsensors auf der Basis eines 2D-refraktiven Linsenarrays und einer invertierten Hartmann-Maske für die optische Messtechnik, die Multikontrastabbildung und die Computertomographie gezeigt.

Mit dem Shack-Hartmann-Wellenfrontsensor wurde eine Multikontrastabbildung der röntgenrefraktiven Diamantlinse durchgeführt. Es war möglich, neben der Intensität auch differentielle Phaseninformationen zu erhalten, um die innere Struktur der Linse und ihre Wellenfrontmodulationsleistung zu untersuchen. Durch die Beibehaltung eines relativ großen Pitch, der eine geringe räumliche Auflösung bedingt, konnte eine Winkelempfindlichkeit von einigen Dezimalen  $\mu\text{radian}$  erreicht werden. Durch die Anwendung des Super-Resolution-Ansatzes auf der Grundlage von Beamlet-Verschiebungen konnte die räumliche Auflösung erhöht werden, was hilfreich sein könnte, wenn man eine höhere Winkel- und Ortsauflösung auf Kosten der Belichtungszeit erreichen möchte.

Die Inspektion der inneren Struktur der mit Glasfasern verstärkten Polymerverbundwerkstoffe war aufgrund der hohen Winkel- und Ortsauflösung, der Kleinwinkelstreuungsempfindlichkeit und der hohen Flux-Effizienz der invertierten Hartmann-Maske möglich. Es wurde gezeigt, dass es möglich ist, eine invertierte Hartmann-Maske für die 2D- und 3D-Abbildung von Materialien mit komplexen Strukturen zu verwenden. Der Bildgebungskanal mit Kleinwinkelstreuung ermöglichte die Verfolgung feiner struktureller Veränderungen wie die Vervielfachung von Mikrobrüchen und die Selbstheilung durch Mikrokapseln in flachen Verbundwerkstoffen. Durch die Kombination eines wenig absorbierenden Substrats und eines invertierten Designs der Hartmann-Maske konnten ähnliche Belichtungszeiten wie bei der konventionellen Röntgenbildgebung erreicht werden, was für tomographische Anwendungen unerlässlich ist. Es war möglich, richtungsabhängige Strukturinformationen aufzunehmen, die unter anderem für die Entwicklung neuer Verbundwerkstoffe wichtig sind.

# Abstract

Over the years, methods sensitive to phase information have attracted great interest in the scientific and engineering communities, evolving steadily and rapidly in areas such as materials science and medicine. The development of such techniques in the field of hard X-rays followed a similar journey to that of visual light optics, including the development and adaptation of analogous optical elements and data processing strategies aimed at obtaining more accurate characterizations. Even though some methods that rely on wave interference could provide high angular sensitivity, implementing such techniques could be complex. Increased requirements for the light source in terms of monochromaticity, flux, and coherence, along with sophisticated mechanics, alignment procedure, and long exposure times. High angular sensitivity could be redundant depending on a specific application, and long exposure times could narrow applicability. Thus, in monitoring fast processes, low flux conditions, versatility, and simplicity of implementing single-shot methods could be preferable.

Hartmann-based wavefront sensing techniques are widely used in astronomy, atmosphere research, and microscopy. It is a versatile set of tools that could provide complementary information to the intensity measurements. However, the X-rays' high energy, high penetration ability, and low refraction index imply the application of complex novel solutions. The state-of-the-art patterning techniques, such as 3D two-photon lithography, Deep X-ray lithography, and well-known methods, such as UV-lithography, allow for fabricating optical components with suitable parameters.

This thesis shows the implementation of the Shack-Hartmann wavefront sensor based on a 2D refractive lens array and inverted Hartmann mask for optics metrology, multi-contrast imaging, and computed tomography.

Multi-contrast imaging of an X-ray refractive diamond lens was performed using the Shack-Hartmann wavefront sensor. It was possible to obtain differential phase information alongside intensity to inspect the inner structure of the lens and its wavefront modulation performance. By keeping a relatively big pitch, which imposes low spatial resolution, it was possible to achieve decimals of  $\mu$ radian angular sensitivity. Applying the super-resolution approach based on beamlet shifts allowed to increase the spatial resolution, with could be helpful if one wants to achieve higher angular and spatial resolution at the cost of exposure time.

Inspection of the inner structure of polymer composite materials, reinforced with glass fibers, was possible due to high angular and spatial resolution, small-angle scattering sensitivity, and high flux efficiency of the inverted Hartmann mask. It was shown that it is possible to use an inverted Hartmann mask for 2D and 3D imaging of materials with complex structures. The small angle scattering imaging channel allowed for tracking of fine structural changes such as microfracture

multiplication and microcapsule-based self-healing in flat composites. The combination of a low absorbing substrate and an inverted design of the Hartmann mask allowed achieving similar exposure times to conventional X-ray imaging, which is essential for tomographic applications. It was possible to record direction-dependent structural information, which is important for new composite materials development, among other applications.

# Acknowledgments

I want to express my gratitude to many people who supported me during my Ph.D. In both scientific/technical questions and private relations.

I would like to thank **Prof. Dr. Jan G. Korvink** for giving me an opportunity to do my Ph.D. at the Institute of Microstructure Technology. I also thank **Prof. Dr. rer. nat. Uli Lemmer** for being my co-referent.

From the bottom of my heart, I thank my direct supervisor, **Dr. Danays Kunka**, for supporting me on every single step of this journey. Without you, it would not be possible at all.

I am grateful to **Dr. habil. Anton Plech** and **Dr. Stefan Reich** for the help with the experiments, providing scripts, and giving insights on the paper drafts. I thank **Sabine Bremer** and **Marcus Zuber** for their time and patience during beamtimes at the Topo-Tomo and CT/CL-lab.

I want to thank all IMT staff, especially **Dipl.-Ing. (FH) Jürgen Benz**, for all the help during these times. I am thankful to **Dr. Klaus Bade**, **Stefan Hengsbach**, and **Florian Rupp** for helping me with 3D-DLW patterning and design discussions. Special thanks to **KNMF facility** for providing facilities. I thank **Karlsruhe House of Young Scientists (KHYS)** for funding the first two years of my Ph.D. studies. Many thanks to the staff of **cSAXS, PSI** for providing me with beamtimes. Special gratitude to **Dr. Ana Diaz** for help, insights, and spending time.

I want to thank my dearest friends, whom I have met at the IMT or knew beforehand: **Margarita Zakharova** and **Vitor Vneska**, who are amazing friends, ready for fun nights and always ready to help; **Anna Zakhurdaeva**, my partner, who helped me to overcome difficulties and remind me to enjoy life; **Norbert Kunka**, who was always supportive and open for another photography journey; **Emil Mamleyev**, **Eduard Madirov**, **Dr. Michael Oldenburg** and **Natalia Kiseleva**, who are always ready to have fun; **Heike Fornasier** and **Alexandra Moritz**, who can always advise on any question related to IMT; special feature **Tomsk squad**, who helped me with programming and good mood; **Dr. Roman Laptev**, my former supervisor and good friend, for fruitful discussions and help; **Dr. Dmitry Karpov**, for all help and discussions related to either photography or cSAXS beamtimes. Additionally, I would like to express my gratitude to team of **Schmidt's Katze** and especially **Bree**.

I have the deepest gratitude to my grandmother, **Saveleva Larisa**, who raised me as her own son, sacrificing her own time and opportunities to give them to me. Every open door, all chances in life that I have is because of You.

Big gratitude to my last neuron for surviving these years. tnx, man.



# Contents

<b>Kurzfassung</b> . . . . .	<b>iii</b>
<b>Abstract</b> . . . . .	<b>v</b>
<b>Acknowledgments</b> . . . . .	<b>vii</b>
<b>1 Introduction</b> . . . . .	<b>1</b>
<b>2 Basics of wave propagation, X-ray-matter interaction and X-ray imaging</b> . . . . .	<b>5</b>
2.1 Propagation of X-rays in free space . . . . .	5
2.2 The interaction of X-rays with matter . . . . .	8
2.3 Single-shot multi-contrast X-ray imaging with Hartmann-based sensors . . . . .	10
2.4 Absorption based X-ray imaging . . . . .	12
2.5 Phase contrast X-ray imaging . . . . .	12
2.6 Scattering contrast X-ray imaging . . . . .	13
2.7 Interleaving super-resolution approach . . . . .	15
2.8 Contrast retrieval . . . . .	15
2.8.1 Single beamlet fitting with 2D Gaussian . . . . .	16
2.8.2 Spatial harmonic analysis . . . . .	17
2.9 The basics of tomography . . . . .	18
2.10 Chapter 2 conclusion . . . . .	23
<b>3 Shack-Hartmann wavefront sensor based on 2D refractive lens array</b> . . . . .	<b>25</b>
3.1 Design evolution and manufacturing of the Shack–Hartmann wavefront sensors based on 2D refractive lens arrays . . . . .	25
3.1.1 SHSX design based on continuous hollow cylindrical lenses . . . . .	26
3.1.2 SHSX design based on continuous hollow parabolic lenses . . . . .	26
3.2 Characterization of produced arrays . . . . .	26
3.2.1 Average gain and focus definition . . . . .	27
3.2.2 Surface roughness impact on gain . . . . .	28
3.2.3 Average spot size and astigmatic aberration quantification . . . . .	29
3.2.4 Homogeneity investigation: gain and visibility maps . . . . .	31
3.2.5 Degradation of polymer lens arrays under continuous X-ray illumination . . . . .	32
3.3 Multi-contrast imaging performance of SHSX v2.0 and v2.1 . . . . .	34
3.4 Chapter 3 conclusion . . . . .	35
<b>4 Inverted Hartmann mask made by deep X-ray lithography</b> . . . . .	<b>37</b>
4.1 Inverted Hartmann masks fabrication by deep X-ray lithography . . . . .	37

4.2	Characterization of manufactured inverted Hartmann masks . . . . .	39
4.2.1	Laboratory setup . . . . .	39
4.2.2	Scanning electron microscopy and visibility measurements . . . . .	40
4.3	Multi-contrast imaging performance of inverted Hartmann mask . . . . .	40
4.4	Polymer composite preparation for multi-contrast X-ray imaging and tomography . . . . .	44
4.4.1	Polymer composite preparation: flat fiber-reinforced composites . . . . .	45
4.4.2	Polymer composite preparation: bulk fiber-reinforced composites . . . . .	46
4.5	Chapter 4 conclusion . . . . .	46
<b>5</b>	<b>Application of Shack-Hartmann sensor and inverted Hartmann mask for single-shot multi-contrast imaging and tomography . . . . .</b>	<b>49</b>
5.1	Super-resolution X-ray multi-contrast imaging of a diamond lens with Shack-Hartmann X-ray sensor using synchrotron light source . . . . .	49
5.1.1	Super-resolution imaging setup and data processing strategy . . . . .	49
5.1.2	Super-resolution X-ray multi-contrast imaging of a diamond lens with Shack-Hartmann . . . . .	50
5.2	Multi-contrast X-ray imaging of the polymer composite materials with self-healing properties . . . . .	51
5.3	Multi-contrast X-ray imaging and tomography of the bulk polymer composite materials . . . . .	54
5.3.1	Setup and data processing strategy . . . . .	54
5.3.2	Multi-contrast single-shot X-ray imaging . . . . .	55
5.3.3	Absorption and scattering tomography of the polymer composite . . . . .	57
5.4	Chapter 5 conclusion . . . . .	60
<b>6</b>	<b>Summary and Outlook . . . . .</b>	<b>63</b>
<b>A</b>	<b>Phase-contrast and scattering contrast imaging of the diamond lens . . . . .</b>	<b>67</b>
<b>B</b>	<b>Super-resolution scattering contrast imaging of the diamond lens . . . . .</b>	<b>69</b>
<b>C</b>	<b>Shack-Hartmann patterns generation routine . . . . .</b>	<b>71</b>
<b>D</b>	<b>Shack-Hartmann patterns generation routine with propagation to the lens focal plane . . . . .</b>	<b>79</b>
	<b>List of Figures . . . . .</b>	<b>85</b>
	<b>List of Tables . . . . .</b>	<b>91</b>
	<b>Peer-reviewed publications . . . . .</b>	<b>93</b>
	<b>Bibliography . . . . .</b>	<b>95</b>

# 1 Introduction

The single-shot phase-sensitive methods for visible light have been well known for around 120 years since Johannes Franz Hartmann introduced his approach for spectrometry applications [Hartmann 1900, 1904]. The Hartmann masks, as an array of holes, are being used successfully in astronomy applications until nowadays. In the late 1960s, US Air Force approached Optical Sciences Center (OSC) at the University of Arizona with the problem of improving the image quality of satellites taken from the earth's surface. The OSC director, an astronomer, Dr. Aden Mienel, proposed the idea of measuring the Optical Transfer Function of the atmosphere simultaneously with imaging a satellite. He tried to use a standard Hartmann test that used arrays of holes made of wooden or cardboard panels. However, the two major problems raised were the weak intensity of the projected spots and the accuracy of the centroid measurements [Platt and Shack 2001]. At this point, Dr. Ronald Shack was involved in the study and proposed to use a lens array instead of an array of holes. Dr. Shack gave a task to the Research Associate, Dr. Ben Platt, who was helping him set up the Optic Testing Lab to purchase an appropriate lens array to test the idea. Unfortunately, at that time, the industry could not design and manufacture an array consisting of lenses with appropriate focal lengths and sizes. After trying several different approaches, Dr. Platt has developed his way of fabricating a lens array in his wife's kitchen. Dr. Shack and Dr. Platt initially presented the results of their work as an oral presentation at the 1971 Spring Meeting of the Optical Society of America [Shack 1971].

From the discovery of the X-rays by Wilhelm Conrad Röntgen on 22<sup>nd</sup> of December 1895 until these days, X-ray science passed through similar steps as the visual light optics but on a much shorter timescale. Similar optical elements were introduced in the X-ray regime, such as mirrors, gratings, phase plates, lenses, etc. However, plenty of necessary adjustments and sometimes not very trivial modifications were implemented due to much shorter wavelengths, high energies, refractive index smaller than unity, and the ability to be harmful to human bodies. The simplest example is that for hard X-rays concave lens is a converging lens contrary to the visible light.

Similarly to the visual light case, scientists and engineers were interested in the phase information of the incoming X-rays for wide variety of application: medical [Momose 2003, Momose et al. 2003, Pfeiffer et al. 2008], material science [Davis et al. 1995, Prade et al. 2017, Senck et al. 2017, Morimoto et al. 2020, Glinz et al. 2021], industrial metrology [Olivo et al. 2008, Miller et al. 2013], scientific purposes [Dean et al. 2006, Saha et al. 2010], etc.

In 1965, U. Bonse and M. Hart published a paper named 'An X-ray interferometer,' which was an important breakthrough for phase-sensitive techniques in the hard X-ray regime [Bonse and Hart 1965]. Using copper  $K\alpha$  line and 37.6  $\mu\text{m}$  thick Lucite crystal, they have recorded a phase-shift of

$2\pi$  radians. After that, variety of the phase-sensitive methods were developed including: analyzer-based imaging [Davis et al. 1995], edge-illumination methods [Olivo et al. 2001, 2011, Vittoria et al. 2015], grating-based interferometry [David et al. 2002, Momose et al. 2003], spatial-harmonics imaging [Wen et al. 2008, 2010], etc.

The following criteria have been formulated within the framework of this thesis to find an appropriate approach or a set of them:

1. It shall be comprehensive, robust, and customizable;
2. Simple to implement on the existing facilities;
3. High tolerance for the low coherence and polychromaticity;
4. Optimized in terms of the mechanical stability of the setup (minimal amount of precision mechanics);
5. Low acquisition time;
6. High flux efficiency.

A possible outcome from the above set of criteria is Hartmann-based techniques. The multi-contrast X-ray imaging methods with Hartmann-based optical elements could simultaneously provide absorption, phase, and scattering imaging modalities. They are relatively easy to implement on the existing facilities because of the single optical element configuration. Those techniques can be used with low-coherence polychromatic sources. There are no requirements for scanning the optical element or sample. Yet, the spatial resolution could be lower than the one provided by the interferometry. However, the acquisition rates are reported to be higher than in the case of interferometric approaches [Zakharova et al. 2019b, Mikhaylov et al. 2020, Zakharova et al. 2021]. The high customizability of the Hartmann-based methods allows one to achieve high flux efficiency.

Summarizing, this work aimed **to develop a generalized approach for wavefront monitoring and multi-contrast X-ray imaging founded on the extension of Hartmann-based techniques for hard X-ray regime at both synchrotron and laboratory light sources.**

The solution is split into two similar techniques: a) The **Shack-Hartmann sensor** for hard X-rays as a suitable tool for X-ray optics metrology, wavefront sensing, and solution for low flux conditions; b) the **inverted Hartmann mask** as a general imaging tool for multi-contrast X-ray imaging and tomography.

The main findings of the current work are:

1. Design, fabrication, and characterization of Shack-Hartmann wavefront sensors for hard X-rays;
2. Design, fabrication, and characterization of inverted Hartmann masks made by X-ray LIGA technology;

3. Wave-front monitoring of the diamond refractive X-ray lens with Shack-Hartmann sensor for hard X-rays;
4. Multi-contrast X-ray imaging of flat fiber-reinforced polymer composites with inverted Hartman mask in a laboratory environment;
5. Multi-contrast X-ray imaging and tomography of bulk fiber-reinforced polymer composites with inverted Hartman mask in a laboratory environment.

In chapter 2, the general questions of wave propagation, imaging concepts, contrast formation, and data processing strategies are presented.

Chapter 3 discusses the design evolution, manufacturing, characterization, and imaging performance of Shack-Hartmann sensors for hard X-rays based on a 2D refractive lens array. The chapter is grounded in the peer-reviewed publication "**Shack–Hartmann wavefront sensors based on 2D refractive lens arrays and super-resolution multi-contrast X-ray imaging**", Mikhaylov, A., et al. [Mikhaylov et al. 2020].

Chapter 4 is focused on the design, fabrication, characterization, and assessment of the multi-contrast X-ray imaging of the in-house made phantom of the Hartmann-based sensor based on the inverted Hartmann mask. The results presented in this chapter are part of the peer-reviewed publication "**Inverted Hartmann mask made by deep X-ray lithography for single-shot multi-contrast X-ray imaging with laboratory setup**," Mikhaylov, A., et al. ([Mikhaylov et al. 2022]).

In chapter 5 demonstrates applications on the wavefront sensing of the X-ray refractive diamond lens (for the Shack-Hartmann sensor for hard X-rays), multi-contrast X-ray imaging, and tomography of the flat and bulk fiber-reinforced polymer composites (for the inverted Hartmann mask). The diamond lens wavefront inspection and multi-contrast X-ray imaging of the fiber-reinforced flat composite materials are published in peer-reviewed articles "**Shack–Hartmann wavefront sensors based on 2D refractive lens arrays and super-resolution multi-contrast X-ray imaging**", Mikhaylov, A., et al. [Mikhaylov et al. 2020], "**Inverted Hartmann mask made by deep X-ray lithography for single-shot multi-contrast X-ray imaging with laboratory setup**", Mikhaylov, A., et al. [Mikhaylov et al. 2022]. The multi-contrast X-ray imaging and tomography of the fiber-reinforced bulk polymer composites, currently under review, were submitted to the Journal of Imaging (MDPI Publishing).



## 2 Basics of wave propagation, X-ray-matter interaction and X-ray imaging

This chapter aims to address general questions of X-ray propagation, the interaction of X-rays with matter, multiple X-ray imaging modalities, and tomography.

The simple approach of following each element in the optical path was chosen to guide the reader. X-rays, generated at the source point such as an X-ray tube or synchrotron light facility, propagating in free space (section 2.1) encounter and interact with a matter (section 2.2) in a form of a sample and an optical element (section 2.3) following with the registration by a detection system. After that, a contrast formation of different modalities such as absorption (section 2.4), phase (section 2.5), and scattering (section 2.6), is discussed. At the end of the chapter, the acquisition (section 2.7), data processing strategies for contrast retrieval from a single exposure (sections 2.8.1 and 2.8.2), and tomography reconstruction (section 2.9) are discussed.

### 2.1 Propagation of X-rays in free space

X-rays are high-energy electromagnetic radiation that lies between ultraviolet and gamma radiation in the electromagnetic spectrum. Although there is no precise definition of the spectrum region to which X-rays belong, scientists have identified a range from 10 pm to 10 nm (124 eV to 124 keV). Thus, as a start, we consider the free-space Maxwell equations:

$$\nabla \cdot \mathbf{E}(x, y, z, t) = 0, \quad (2.1)$$

$$\nabla \cdot \mathbf{B}(x, y, z, t) = 0, \quad (2.2)$$

$$\nabla \times \mathbf{E}(x, y, z, t) + \frac{\partial}{\partial t} \mathbf{B}(x, y, z, t) = \mathbf{0}, \quad (2.3)$$

$$\nabla \times \mathbf{B}(x, y, z, t) - \epsilon_0 \mu_0 \frac{\partial}{\partial t} \mathbf{E}(x, y, z, t) = \mathbf{0}. \quad (2.4)$$

Here  $\mathbf{B}$  is the magnetic induction,  $\mathbf{E}$  is the electric field,  $\epsilon_0$  is the electrical permittivity, and  $\mu_0$  is the magnetic permeability. By taking the curl of equation 2.3 and taking into account equations 2.1 and 2.2, we could obtain the vacuum field equation for the electric field (d'Alembert wave equation)

$$\left( \epsilon_0 \mu_0 \frac{\partial^2}{\partial t^2} - \nabla^2 \right) \mathbf{E}(x, y, z, t) = \mathbf{0}. \quad (2.5)$$

Using a similar approach, by taking the curl of equation 2.4 and following the chain of logic, we could obtain the vacuum field equation for the magnetic induction

$$\left( \epsilon_0 \mu_0 \frac{\partial^2}{\partial t^2} - \nabla^2 \right) \mathbf{B}(x, y, z, t) = \mathbf{0}. \quad (2.6)$$

By considering propagation wave as monochromatic plane-wave and solving equations 2.5 and 2.6 one could determine the speed of wave propagation as

$$c = \frac{1}{\sqrt{\epsilon_0 \mu_0}} \quad (2.7)$$

Equations 2.5 and 2.6 state that all components of the free-space electric and magnetic fields are uncoupled and obey a scalar for the d'Alembert wave equation. Thus, from now on, instead of two vector fields, we would consider one scalar field  $\Psi(x, y, z, t)$ . Taking into account equation 2.7, this function is a solution to the d'Alembert equation

$$\left( \frac{1}{c^2} \frac{\partial^2}{\partial t^2} - \nabla^2 \right) \Psi(x, y, z, t) = 0. \quad (2.8)$$

Let's call  $\Psi(x, y, z, t)$  a wave-function. By using Fourier integral, we spectrally decompose this wave-function as a superposition of monochromatic fields

$$\Psi(x, y, z, t) = \frac{1}{\sqrt{2\pi}} \int_0^\infty \psi_\omega(x, y, z) e^{(-i\omega t)} d\omega \quad (2.9)$$

where each monochromatic component is written as a product of a complex function that describes spatial disturbance  $\psi_\omega(x, y, z)$  and harmonic factor  $e^{(-i\omega t)}$  [Paganin et al. 2006]. Substituting equation 2.9 into equation 2.8, we determine the time-dependent equation, known as the Helmholtz equation, that describes the evolution of the spatial wave-function  $\psi_\omega(x, y, z)$  as

$$\left( \nabla^2 + \frac{\omega^2}{c^2} \right) \psi_\omega(x, y, z) = 0. \quad (2.10)$$

One of the particular solutions to the equation 2.10 is a plane wave case

$$\psi_\omega^{PW}(x, y, z) = e^{i(k_x x + k_y y + k_z z)}, \quad (2.11)$$

$$k_x^2 + k_y^2 + k_z^2 = k^2 \quad (2.12)$$

where  $(k_x, k_y, k_z)$  are  $x$ ,  $y$  and  $z$  components of the wavevector  $\mathbf{k}$ , which point in the direction of the plane wave propagation. By isolation  $k_z$ , equation 2.11 could be rewritten as

$$\psi_{\omega}^{PW}(x, y, z) = e^{i(k_x x + k_y y)} e^{[iz\sqrt{k^2 - k_x^2 - k_y^2}]}. \quad (2.13)$$

By setting  $z = 0$  in equation 2.13, one could obtain wave-function at the source position as

$$\psi_{\omega}^{PW}(x, y, z = 0) = e^{i(k_x x + k_y y)}. \quad (2.14)$$

Comparing equations 2.13 and 2.14, one could notice that if the value  $\psi_{\omega}^{PW}(x, y, z = 0)$  is known it is possible to evaluate at distance  $z$  by multiplying it by the so-called *free-space propagator*  $e^{[iz\sqrt{k^2 - k_x^2 - k_y^2}]}$ .

Let  $\mathcal{F}$  denote Fourier transform. Then, the unpropagated field at source plane  $z = 0$  could be decomposed into a linear combination of plane waves using Fourier integral [Paganin et al. 2006], as

$$\psi_{\omega}(x, y, z = 0) = \frac{1}{2\pi} \iint \mathcal{F}(\psi_{\omega}(k_x, k_y, z = 0)) e^{i(k_x x + k_y y)} dk_x dk_y. \quad (2.15)$$

Therefore, we obtain propagated value  $\psi_{\omega}(x, y, z = z')$  by multiplying Fourier decomposition 2.15 by the free-space propagator (some dependencies are omitted)

$$\begin{aligned} \psi_{\omega}(x, y, z = z') &= \frac{1}{2\pi} \iint \mathcal{F}(\psi_{\omega}(k_x, k_y, z = 0)) \\ &\times e^{[iz'\sqrt{k^2 - k_x^2 - k_y^2}]} e^{i(k_x x + k_y y)} dk_x dk_y. \end{aligned} \quad (2.16)$$

Now, let us consider paraxial approximation, i.e., waves propagate at small angles to the optical axis  $z$ . This implies  $k_x$  and  $k_y$  values to be much lower in comparison to  $k_z$ . In this way, we result in

$$e^{[iz'\sqrt{k^2 - k_x^2 - k_y^2}]} \approx e^{ikz'} e^{-\frac{iz'(k_x^2 + k_y^2)}{2k}}. \quad (2.17)$$

combination of equations 2.16 and 2.17 leads to the Fresnel diffraction integral

$$\begin{aligned} \psi_{\omega}(x, y, z = z') &= -\frac{ik e^{ikz'}}{2\pi z'} e^{\frac{ik}{2z'}(x^2 + y^2)} \\ &\times \iint_{-\infty}^{\infty} \psi_{\omega}(x', y', z = 0) e^{\frac{ik}{2z'}(x'^2 + y'^2)} \\ &\times e^{\frac{ik}{z'}(xx' + yy')} dx' dy'. \end{aligned} \quad (2.18)$$

Let us reformulate the chirp function's  $e^{\frac{ik}{2z'}(x'^2+y'^2)}$  argument and define the so-called Fresnel number  $F$  as

$$\frac{k}{2z'}(x'^2 + y'^2) = \frac{\pi(x'^2 + y'^2)}{\lambda z'}, \quad (2.19)$$

$$F := \frac{a^2}{\lambda z'}, \quad (2.20)$$

where  $a$  is the smallest structure of interest, or is the diameter of the region where unpropagated disturbance is non-negligible. Considering large propagation distances  $z'$  (case when  $z' \gg \lambda, a$ ), Fresnel number approaches zero. Thus chirp function's limit approaches one, meaning that Fresnel diffraction integral 2.18 becomes the Fourier transform of the wavefield, also known as Fraunhofer far-field approximation. Similarly, when the Fresnel number approaches unity, it is a case of optical near field.

## 2.2 The interaction of X-rays with matter

Interactions of X-ray photons with an atom could be described as absorption and scattering [Als-Nielsen and McMorrow 2011]. A dense medium consisting of numbers of atoms/molecules is usually treated as a continuum, with an interface to the surrounding air (vacuum, in a more general case). At such interfaces, X-rays are refracted and reflected.

The classical approach to scattering it is to treat it as an *elastic*. It means that there is no act of energy transfer and the incident wave has the same wavelength (or frequency) as a scattered. However, according to the quantum theory, energy may be transferred from an X-ray photon to an electron, resulting in the higher wavelength (lower frequency) of the scattered wave. Such scattering is called *inelastic* or *Compton scattering* [Als-Nielsen and McMorrow 2011]. In the case of dense matter, elastic scattering is the main process because the photon momentum is taken by atoms and the lattice rather than a single electron. Thus, the classical approach is a good approximation. The total mass attenuation coefficient  $\mu$  can be decomposed into contributions from different photon interaction modes as

$$\mu = \mu_R + \mu_p + \mu_C \quad (2.21)$$

where R is designated to Rayleigh (*coherent*) scattering, p to the photoelectric effect, and C to Compton (*incoherent*) scattering [McCullough 1975]. The cross sections of coherent/incoherent X-ray scattering and photoelectric effect depend on photon energy. While *incoherent* X-ray scattering dominates only at very high energies, *coherent* has a lower cross section at a wide range of energies compared to the photoelectric effect. Thus, the photoelectric effect is the main process of absorption. The X-ray attenuation coefficient is highly dependent on the  $Z$  of the material.

Generally, beam attenuation is described by the Beer-Lambert-Bouguer law. For 1D case, it could be represented as

$$I(z) = I_0 e^{-\mu_z z} \quad (2.22)$$

where  $I$  and  $I_0$  are intensities of attenuated and incoming beams, respectively,  $\mu_z$  is a linear attenuation coefficient and  $z$  is the depth from the surface.

Since X-rays are electromagnetic waves, refraction at interfaces phenomena shall be addressed. To describe refraction, similarly to visible light, one should consider the refractive index. In contrast to the visible range, the refraction index of X-rays differs from unity by varying small value [Als-Nielsen and McMorrow 2011]. In general, in the case of X-rays refractive index could be written as

$$n = 1 - \delta + i\beta \quad (2.23)$$

where  $\delta$  is of order  $10^{-5} - 10^{-7}$  and assigned with to refraction, while  $\beta$  is of order  $10^{-8} - 10^{-9}$  and assigned to absorption. Both  $\delta$  and  $\beta$  coefficients are defined as follows:

$$\delta(\mathbf{r}, E) = \frac{r_0 h^2 c^2}{2\pi E^2} \rho(\mathbf{r}) \sim O\left(\frac{1}{E^2}\right), \quad (2.24)$$

and

$$\beta(\mathbf{r}, E) = \frac{hc}{4\pi E} \mu_p(\mathbf{r}, E) \sim O\left(\frac{1}{E^4}\right), \quad (2.25)$$

where  $E$  is the X-ray energy,  $\rho$  is the electron density,  $r_0$  is the classical electron radius. The practical meaning of an index of refraction less than unity is that the X-rays undergo total external reflection below a certain incident grazing angle (critical angle  $\alpha_c$ ). X-rays entering a medium are refracted away from the interface surface normal in contrast to the visible light. Snell's law with applied  $\alpha = \alpha_c$  and  $\alpha' = 0$  and using 2.23 results in

$$\alpha_c = \sqrt{2\delta} \quad (2.26)$$

where  $\beta = 0$  for simplicity. This property of X-rays is widely used for focusing and surface analysis.

## 2.3 Single-shot multi-contrast X-ray imaging with Hartmann-based sensors

Shack–Hartmann sensors (SHS) have been known since the early twentieth century in the visible light range. In 1900, Johannes Hartmann created the first tool to check for approximate focus, and to measure aberrations in the mirrors and lenses of large telescopes [Hartmann 1900]. This tool, called the Hartmann mask or Hartmann sensor (HS), initially consisted of an opaque screen with numerous holes. Each hole acted as an opening to isolate a small group of light beams, which could be traced to determine any deviation in the direction of propagation. This deviation would correspond to the local slope of the wavefront, thus detecting wavefront modifications associated with the quality of the image.

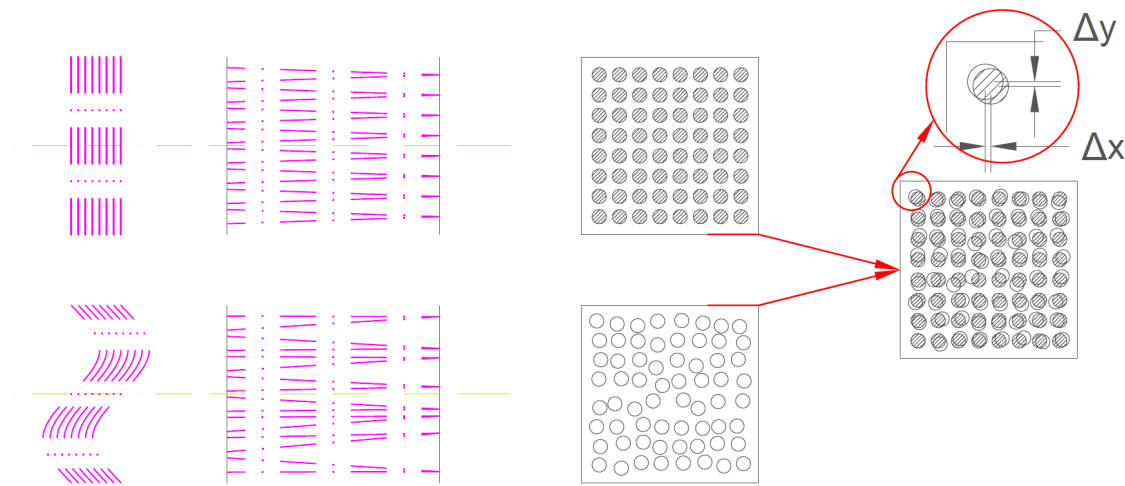


**Figure 2.1:** Basic Hartmann wavefront sensor principle. Two images are required to extract information on the wavefront: a reference image of the projected pattern (co-called flat-field) and a distorted pattern. Measured shifts of the spots are proportional to the first derivative of the phase.

Years later, the HS was modified by replacing the apertures with an array of lenslets, thus increasing the signal-to-noise ratio [Shack 1971]. Since then, HS and SHS have continuously evolved, and the sensors have also been gaining attraction in the X-ray regime [Mayo and Sexton 2004, Reich et al. 2018, Letzel et al. 2019] in the recent past. dos Santos Rolo and collaborators demonstrated the use of a 2D array of cylindrical polymer refractive lenses as a Shack–Hartmann sensors for hard X-rays (SHSX). Furthermore, this made fast single-shot multi-contrast imaging of the dynamics of materials with spatial resolution in the micrometre range possible [dos Santos Rolo et al. 2018].

To illustrate the general idea of analysis of the HS or SHS patterns, let us consider an individual beamlet formed by an aperture or lens. Presence of absorbing (Figure 2.2a), refractive (Figure 2.2b) or scattering (Figure 2.2c) media in the beam path change in intensity, position, and broadening of an each beamlet respectively could be recorded. Mostly, during imaging experiment one could record mixed signal that simultaneously represent all three types of contrasts (Figure 2.2d). Figure 2.3 shows simulated data of reference pattern and final pattern with given wavefront.

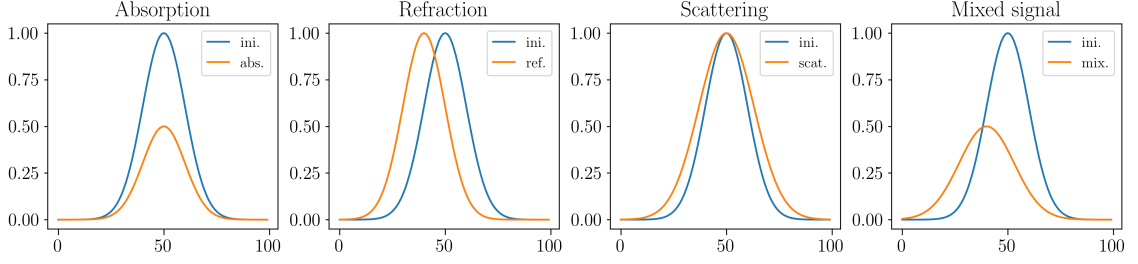


**Figure 2.2:** Illustration of the presence of absorptive, refractive, scattering, and mixed media on shape and location parameters of the single beamlet.

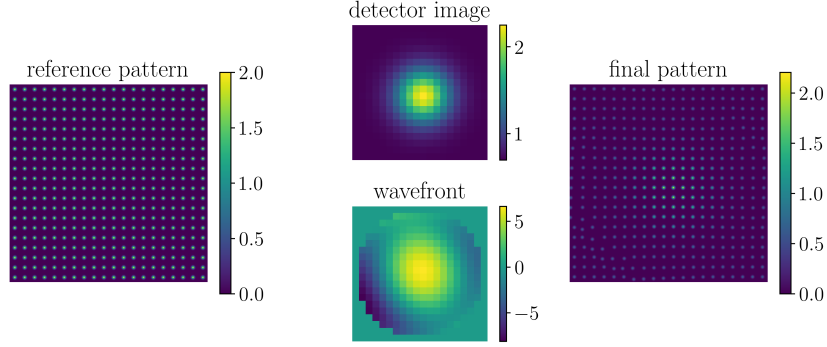


**Figure 2.3:** Simulated Shack-Hartmann patterns for flat wave (reference pattern) and aberrated wave (final pattern).

Multi-contrast retrieval procedure could be performed by single beamlet fitting [Vittoria et al. 2015, dos Santos Rolo et al. 2018] or by spatial harmonic analysis [Wen et al. 2010] (discussed in section 2.8).

The inverted Hartmann Mask is a periodic two-dimensional pattern of gold pillars without supporting structures on a low-absorbing substrate. It has a lower attenuation, which improves the flux efficiency and provides a higher signal-to-noise ratio for measurements, crucial for low-brilliance sources like X-ray tubes [Zakharova et al. 2018, 2019a,b, Gustschin et al. 2021]. The method showed higher measurement visibility than multi-grating imaging schemes due to a lower average absorption [Zanette et al. 2010, Vila-Comamala et al. 2018, Seifert et al. 2018, Romano et al. 2020, Vila-Comamala et al. 2021].

Inverted Hartmann Mask being introduced in the beam path modulates the wavefront of the incoming wave. Wavefront modulation strongly depends on the percentage of the X-rays absorbed by periodic gold patterns. In the previous paper, we demonstrated the capabilities of phase-contrast imaging with UV lithography-made inverted Hartmann Mask in a laboratory setup with the X-ray tube operated at 40 kVp with a peak energy of 24 keV [Zakharova et al. 2019a]. To extend the imaging capabilities of the method towards higher spatial resolution and higher energy applications, we used Deep X-ray lithography as a tool to produce the aforementioned masks with higher pillars and smaller periodicity. Deep X-ray lithography is a well-known technique that allows high aspect ratio structures patterning over a wide area [Saile et al. 2009, Guckel 1998, Park et al. 2019]. Recent advances in deep X-ray lithography enable pattern structures down to sub-micrometer sizes [Mappes et al. 2007, Faisal et al. 2019].

## 2.4 Absorption based X-ray imaging

Almost immediately after the Röntgen discovered the X-rays, on 22<sup>nd</sup> of December 1895, the first-ever radiography image, known as *Hand mit Ringen* (Hand with Rings), was acquired. It was an image of Röntgen's wife, Anna Bertha. The image shows highly absorbing materials, such as bones and metal rings, relatively clearly, while soft tissue appears blurry and barely visible. This date could be considered the 'Birthday' of modern radiography or, generally, X-ray imaging.

As stated in section 2.2, absorption coefficient  $\mu$  has a strong dependency on material properties and energy of X-rays. Let us consider a three-dimensional object illuminated by a perfectly narrow X-ray beam and X-rays propagation axis is named  $z$ . For generalization, we assume the absorption coefficient  $\mu(x, y, z)$  of the object to be non-uniform. In that case, according to Beer-Lambert-Bouguer law (equation 2.22), intensity recorded by a detector [Als-Nielsen and McMorrow 2011] located right behind the sample is

$$I = I_0 e^{-\int \mu(x,y,z) dz}. \quad (2.27)$$

The projection equation 2.27 could be rearranged as follows

$$-\ln\left(\frac{I}{I_0}\right) = -\ln(T) = \int \mu(x, y, z) dz. \quad (2.28)$$

## 2.5 Phase contrast X-ray imaging

A phase change  $\phi(\mathbf{r}_\perp)$  for a wave propagating along the  $z$ -axis is given by

$$\phi(\mathbf{r}_\perp; z, k) = -k \int_{-\infty}^z \delta(\mathbf{r}_\perp, z'; k) dz' = -\frac{2\pi r_0}{k} \int_{-\infty}^z \rho(\mathbf{r}_\perp, z') dz' \sim O\left(\frac{1}{E}\right) \quad (2.29)$$

where  $\delta$  and  $\rho$  are explained in section 2.2. For single-shot non-interferometric imaging with Hartmann and Shack-Hartmann sensors, shifts of the separate beamlets are proportional to the first derivative of the phase shift. An angular deviation in  $x$  and  $y$  directions for small phase changes can be expressed as

$$\Delta\alpha_{x,y} = -\frac{1}{k} \frac{\partial\phi(x, y)}{\partial x, y} \approx -\frac{1}{k} \frac{\Delta x, y}{L} \sim O\left(\frac{1}{E^2}\right). \quad (2.30)$$

where  $\Delta x, y$  are the beamlet shifts and  $L$  mask/lens array to detector distance.

There are two general types of wavefront reconstruction approaches for Hartmann-based sensors which are preferable for different applications: algebraic, most popular for metrology applications and FFT-based, widely used in imaging applications. In turn, algebraic methods could be divided into modal and zonal approaches. The modal approach based on approximation of the wavefront gradients using set of derivatives of 2D polynomials such as Chebyshev or Zernike polynomials.

This approach allows one to access different polynomial modes associated with known wavefront aberrations. However, modal reconstruction has one drawback: calculation of polynomial derivatives is calculation intense process. Especially for circular polynomials as Zernike polynomials in Cartesian coordinates. One of the ways how to solve that is to calculate derivatives and store them. Nevertheless, one need to be sure that sufficient amount of derivatives of a higher modes are stored.

In contrast, zonal reconstruction does not depend on any pre-calculations. Zonal reconstruction approaches usually employ one of three geometries: Southwell, Hudgin, or Fried [Southwell 1980]. Zonal methods are iterative methods and sometimes could be calculation intensive. However modern algorithms do not require a high amount of iterations. As an example, the modified Southwell algorithm reported in [Pathak and Boruah 2014] shows stabilization after 10 iterations.

Similarly, FFT-based algorithms could be divided into iterative least-square minimization [Roddier and Roddier 1991] that uses equation 2.31 and noniterative complex plane integration [Kottler et al. 2007, Morgan et al. 2011] that uses equation 2.32.

$$\phi_{integrated}(x, y) = \mathcal{F}^{-1} \left[ \frac{v_x \cdot \mathcal{F}\left(\frac{\partial\phi}{\partial x}\right)[v_x, v_y] + v_y \cdot \mathcal{F}\left(\frac{\partial\phi}{\partial y}\right)[v_x, v_y]}{v_x^2 + v_y^2} \right] \quad (2.31)$$

$$\phi_{integrated}(x, y) = \mathcal{F}^{-1} \left[ \frac{\mathcal{F}\left(\frac{\partial\phi}{\partial x}\right)[v_x, v_y] + i \cdot \mathcal{F}\left(\frac{\partial\phi}{\partial y}\right)[v_x, v_y]}{v_x + i \cdot v_y} \right] \quad (2.32)$$

The basic assumption for this approach is that wavefront function is differentiable everywhere [Bon et al. 2012].

## 2.6 Scattering contrast X-ray imaging

The Harmann-based approach's scattering imaging modality is closely related to Small-Angle X-ray Scattering (SAXS). The scattering contrast is often attributed to small-angle scattering on electron density variation of structures which are not resolved in the standard for single-shot multi-contrast imaging setup conditions [Wen et al. 2008, Yashiro et al. 2010, Lynch et al. 2011, Prade et al. 2016, Strobl 2014]. However, there are more contributions to the scattering signal. This section covers only contributions relevant to the results discussed in chapter 5, such as unresolved phase signals [Yashiro and Momose 2015, Koenig et al. 2016, **Mikhaylov** et al. 2022], second-order phase derivative [Yang and Tang 2012], wavefront curvature [Wolf et al. 2015], inelastic scattering [Pelzer et al. 2016] etc.

Here i will mention only such contributions that are relevant for the results discussed in chapter 5 such as unresolved phase signal [Yashiro and Momose 2015, Koenig et al. 2016, **Mikhaylov** et al. 2022], second order phase derivative [Yang and Tang 2012], wavefront curvature [Wolf et al. 2015], inelastic scattering [Pelzer et al. 2016] etc.

For SAXS, scattering intensity  $I^{SAXS}(q)$  normalized by incoming flux could be described as follows:

$$I^{SAXS}(q) = \left| \int_V f \rho_{avg} e^{i\mathbf{q}\cdot\mathbf{r}} dV \right|^2, \quad (2.33)$$

where  $f$  is the atomic scattering factor and  $\mathbf{q}$  is the scattering vector with the magnitude

$$|\mathbf{q}| = \frac{2}{k} \sin\left(\frac{\theta}{2}\right) \approx \frac{1}{k} \theta, \quad (2.34)$$

where  $\theta$  is half of the scattering angle.

In the standard for single-shot multi-contrast imaging setup, maximum and minimum values for scattering angles and scattering vectors in case the of a monochromatic parallel beam could be written as

$$\theta_{min} \approx \frac{d_{pix}}{L} \quad \text{and} \quad \theta_{max} \approx \frac{P}{L}, \quad (2.35)$$

$$q_{min} \approx \frac{d_{pix}}{kL} \quad \text{and} \quad q_{max} \approx \frac{P}{kL}, \quad (2.36)$$

where  $d_{pix}$  - detector pixel size,  $P$  - mask/lens array period and  $L$  - object detector distance. The autocorrelation length [Lynch et al. 2011, Prade et al. 2016] could be defined as

$$\xi = \frac{\lambda L}{P}, \quad (2.37)$$

which has an obvious relation with  $q_{max} = \frac{2\pi}{\xi}$ . Figure 2.4 shows normalized scattering intensity distribution of monochromatic X-rays with an energy of 15 keV ,  $L = 15$  cm on spheres with diameter distribution from 10 to 1500 nm for the same autocorrelation length  $\xi \approx 124$  nm.

The maximum scattering intensity is located at approx.  $1.77\xi$ . The analytical equation for the Dark-Field (Scattering) Extinction Coefficient  $\mu_d$  was proposed in [Lynch et al. 2011] and could be written as

$$\mu_d = \frac{3\pi^2}{\lambda^2} \phi |\Delta\chi|^2 \begin{cases} D - \sqrt{D^2 - \xi^2} \left( 1 + \frac{1}{2} \left( \frac{\xi}{D} \right)^2 \right) + \\ \left( \frac{\xi^2}{D} - \frac{\xi^4}{4D^3} \ln \left[ \frac{1 - \sqrt{1 - \left( \frac{\xi}{D} \right)^2}}{1 + \sqrt{1 - \left( \frac{\xi}{D} \right)^2}} \right] \right), \text{ for } \xi < D; \\ D, \text{ for } \xi \geq D. \end{cases} \quad (2.38)$$

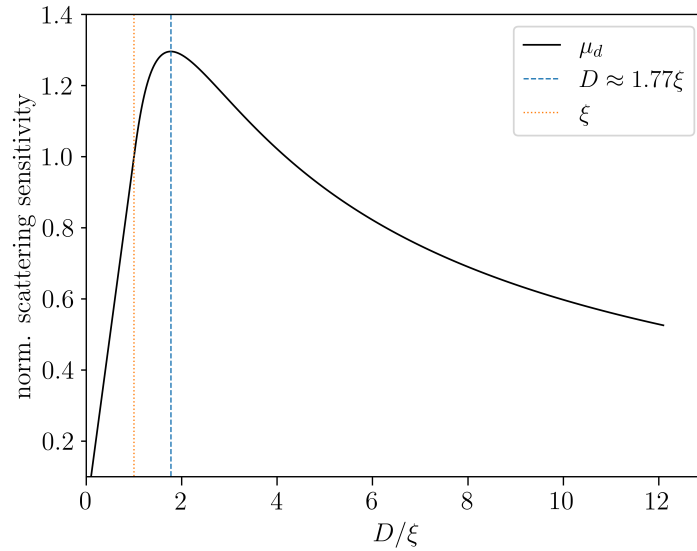


**Figure 2.4:** Dark-Field (Scattering) Extinction Coefficient calculated according to [Lynch et al. 2011] for  $E=15$  keV,  $L = 15$  cm,  $P = 100 \mu\text{m}$  and diameters of spheres 10-1500 nm.

## 2.7 Interleaving super-resolution approach

Spatial resolution in single-shot non-interferometric imaging techniques based on Hartmann and Shack-Hartmann sensors is defined by mask/lens array period, point spread function of the imaging system, and indirectly by detector pixel size. Each beamlet shall be resolved by at least 3 pixels according to the Kotelnikov theorem (or Nyquist-Shannon theorem). Thus, even though masks/lens arrays with much smaller pitches can be manufactured, there is a limit based on detector pixel size and, in the case of cone beam configuration, magnification of the setup.

To increase the limited spatial resolution interleaving super-resolution approach can be employed. Figure 2.5 shows the basics of the proposed approach. Direct projection of the beamlets onto a circular object has poor spatial sampling. It is possible to increase the sampling rate by shifting the sample or mask/lens array. Practically, sample shifting is preferable due to the wavefront's inhomogeneity. By keeping the optical component in the same position in the beam, you need just one flat field image and there is no statistical error accumulation.

## 2.8 Contrast retrieval

The contrast retrieval procedure can be performed by several algorithms, depending on the setup conditions, optical element, and needs [Wen et al. 2010, Vittoria et al. 2015, dos Santos Rolo et al. 2018, Reich 2019]. Within this work, only two algorithms were used: least-square single beamlet 2D Gaussian fitting (2DG) and Fourier spatial harmonic analysis (FSHA). The main advantage of the 2DG approach is a direct access to beamlet parameters which can be used for lens array characterization in the case of the Shack-Hartmann sensor. However, the FSHA routine allows

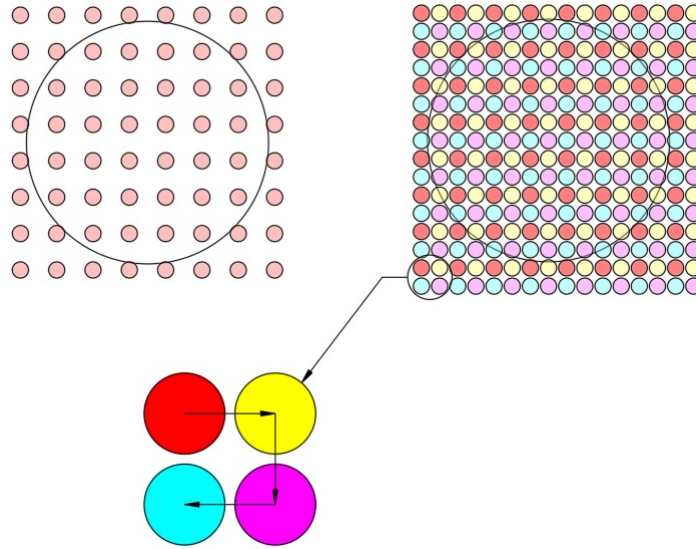


**Figure 2.5:** Interleaving super-resolution approach. Colors red, yellow, magenta, and light blue represent the sequential image acquisitions.

retrieving all three contrast much faster using Fast Fourier Transformation, less sensitive to noise, and does not show increased values for phase contrast measurements.

### 2.8.1 Single beamlet fitting with 2D Gaussian

To perform contrast retrieval using the 2D Gaussian approach, each spot of the recorded reference (or flat field) and experimental patterns are separately fitted by 2D Gaussian as follows:

$$g(x, y) = h \cdot \exp\left(-\left(\frac{(x - \mu_x)^2}{2\sigma_x^2} + \frac{(y - \mu_y)^2}{2\sigma_y^2}\right)\right) + o \quad (2.39)$$

where  $h$  is the height,  $o$  is the offset,  $\sigma_{x,y}$  are the width values and  $\mu_{x,y}$  are the peak positions in the horizontal and vertical directions, respectively. To extract transmission  $T$ , differential phase in horizontal  $dP_x$  and vertical  $dP_y$  directions and scattering contrast in horizontal  $S_x$  and vertical  $S_y$  directions, the following expressions were used (indices  $s$  and  $f$  denote sample and flat field, respectively):

$$T = \frac{h_s}{h_f} \quad (2.40)$$

$$dP_{x,y} = \mu_{x,y,s} - \mu_{x,y,f} \quad (2.41)$$

$$S_{x,y} = \sigma_{x,y,s} - \sigma_{x,y,f} \quad (2.42)$$

The height parameter  $h_f$  allows one to assess gain values of the produced lens arrays by comparing the recorded pattern with a flat beam. The width parameters  $\sigma_{x,f}$  and  $\sigma_{y,f}$  are used in the focal distance  $f$  determination, assuming width of the beamlets to be minimal at the focal position.

## 2.8.2 Spatial harmonic analysis

Due to the design of optical elements in Hartmann-based techniques, which acts as a wavefront modulator, the recorded projected patterns have a spatial periodicity. When an object is inserted into the beam path, the periodicity of the projected pattern is disturbed. The Fourier approach allows one to quantify disturbance of the periodicity in a fast and precise way [Wen et al. 2010, Reich 2019].

As mentioned above, the optical element in Hartmann-based methods acts as a wavefront modulator and periodically samples it. Due to that, the spatial frequency spectrum or Fourier image of the recorded pattern contains a number of sharp peaks at  $(\frac{2\pi m}{P}, \frac{2\pi n}{P})$ , where  $m, n$  are integer numbers, and  $P$  is the projected period of the optical element (figure 2.6). They are commonly referred as the harmonic peaks and are labeled  $(m, n)$ .

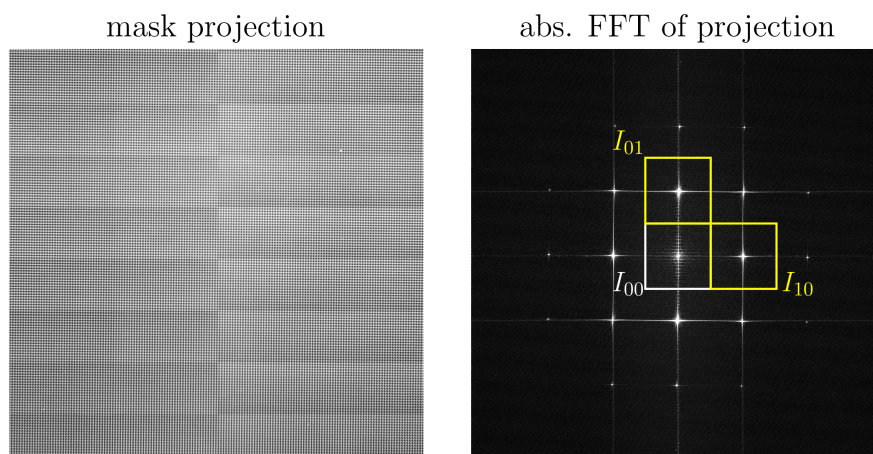


**Figure 2.6:** Example of mask projection and the absolute value of its Fourier transform. Experimental data were acquired in cone beam configuration with  $10 \mu\text{m}$  period mask,  $\approx 140\times$  magnification and detector Perkin Elmer XRD 1621.

A reference (or flat field) pattern is required to retrieve all three contrasts, similarly to the 2DG approach. Both, sample and reference images are multiplied by a Hann window function and transformed to the spatial frequency domain. The central harmonic  $(0, 0)$  does not contain wavefront modulation, representing absorption-only image. Additionally, Fourier analysis, in that case, acts as a low pass filter [Reich 2019]. Transmission contrast is defined as follows, with indices  $s$  and  $f$  denoting sample and flat field, and  $\mathcal{F}^{-1}$  denotes the inverse Fourier Transform:

$$T = \frac{\mathcal{F}^{-1}\{I_s^{0,0}\}}{\mathcal{F}^{-1}\{I_f^{0,0}\}}, \quad (2.43)$$

Differential phase contrast is defined as a shift of the beam pattern and could be quantified by the difference in the complex angle of the back-transformed first harmonic peaks (0,1) and (1,0):

$$d\Phi = \angle \mathcal{F}^{-1}\{I_s^{m,n}\} - \angle \mathcal{F}^{-1}\{I_f^{m,n}\}. \quad (2.44)$$

Intensity of those first harmonic peaks correspond to the amplitude of the projected pattern fringes and influenced by both absorption and scattering. Due to that, there is a need for correction by the transmission  $T$ :

$$S_{m,n} = -\ln \left[ \frac{\mathcal{F}^{-1}\{I_s^{m,n}\} / \mathcal{F}^{-1}\{I_f^{m,n}\}}{T} \right] = -\ln \left[ \frac{\mathcal{F}^{-1}\{I_s^{m,n}\} \cdot \mathcal{F}^{-1}\{I_f^{0,0}\}}{\mathcal{F}^{-1}\{I_s^{0,0}\} \cdot \mathcal{F}^{-1}\{I_f^{m,n}\}} \right]. \quad (2.45)$$

FSHA is well known to have a crosstalk between transmission and scattering contrast channels in the case of materials with relatively high absorption [Kaeppler et al. 2014, Vittoria et al. 2015]. Thus, decorrelation procedure proposed by [Kaeppler et al. 2014] based on polynomial dependence can be used to overcome that.

## 2.9 The basics of tomography

As shown in section 2.4, in conventional absorption-based X-ray imaging, only a projection of the object is taken, leading to a lack of relevant details. To overcome this constraint, one could perform tomographic scan, conventionally referred as a CT. By recording a set of projections with respect to the rotation of the sample or by rotating the source and detector around the sample, it is possible to reconstruct a three-dimensional distribution of absorption coefficients, equivalent to the Radon transform of the object. The most widely adopted approach for tomography reconstruction is to use Fourier methods to inverse Radon transform. For a better understanding of the reconstruction process, let us discuss the Fourier Central Slice (FCS) theorem.

Consider a two-dimensional function  $f(x, y)$  which is projected along axis  $y$  and generates a one-dimensional function of  $x$  as

$$p(x) = \int f(x, y) dy. \quad (2.46)$$

It is worth mentioning that equation 2.46 is a general form of equation 2.28. Now, let us define the Fourier transform of function  $f(x, y)$ , evaluate its central slice ( $q_y = 0$ ), and Fourier transform of projection  $p(x)$  as

$$F(q_x, q_y) = \iint f(x, y) e^{i(q_x x + q_y y)} dx dy, \quad (2.47)$$

$$F(q_x, q_y = 0) = \int \left[ \int f(x, y) dy \right] e^{iq_x x} dx, \quad (2.48)$$

$$P(q_x) = \int p(x) e^{iq_x x} dx. \quad (2.49)$$

Combining equations 2.50, 2.48, and 2.49, one could obtain the following equation

$$F(q_x, q_y = 0) = \int p(x) e^{iq_x x} dx = P(q_x). \quad (2.50)$$

Equation 2.50 shows the equality of Fourier transforms of the projections in a particular direction and slices through the origin of the Fourier transform of  $f(x, y)$  in the direction of propagation. Thus, by recording projections of a two-dimensional object under a set of different angles, taking the one-dimensional Fourier transforms of them, and aligning in the accordance with rotation angles, one could sample an object in the Fourier space. Later, the object could be reconstructed by taking the two-dimensional inverse Fourier transform, as shown in figure 2.50.

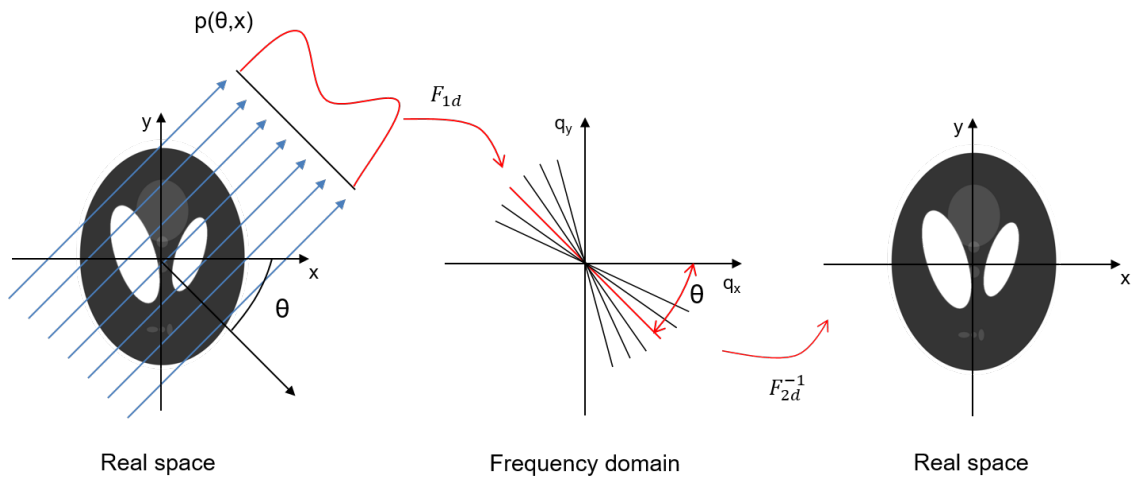


**Figure 2.7:** Fourier Central Slice Theorem states the equality between one-dimensional Fourier transforms of the object projection and the slice through the origin of two-dimensional Fourier transform of the same object parallel to the projection line.

Such reconstruction approach is called Direct Fourier Reconstruction and can be summarized in the following algorithm.

---

**Algorithm 1** Direct Fourier Reconstruction algorithm, 2D case with 1D projections

---

- 1: Apply 1D FFT to all the available projections taken as angles  $\theta_i$ ;
  - 2: Utilizing the FCS theorem arrange 1D Fourier images of the projections in the frequency domain to obtain an approximated 2D Fourier image  $\tilde{F}$  of initial function  $f$ ;
  - 3: Perform reconstruction of the initial function by taking  $\mathcal{F}_{1d}^{-1} \tilde{F}$ .
- 

However, Direct Fourier Reconstruction leads to severe artifacts and dis-balance in the low/high frequency representation in the final image: one could notice a higher sampling in the lower

frequency range than in the higher frequency of the Fourier space. One of the ways to solve that is to use the Filtered Backprojections (FBP) approach.

To obtain the reconstruction formula, let us rewrite the inverse 2D FT of the Fourier image of function  $f$ .

$$\begin{aligned}
 f(x, y) &= \int_{-\infty}^{\infty} dv \int_{-\infty}^{\infty} d\xi F(\xi, v) e^{j2\pi(\xi x + v y)} \\
 &= \int_0^{\pi} d\phi \int_{-\infty}^{\infty} d\nu F(\nu, \phi) |\nu| e^{j2\pi\nu(x\cos\phi + y\sin\phi)} \\
 &= \int_0^{\pi} d\phi \int_{-\infty}^{\infty} d\nu P(\nu, \phi) |\nu| e^{j2\pi\nu(x\cos\phi + y\sin\phi)}
 \end{aligned} \tag{2.51}$$

where  $\xi, \nu$  are the coordinates of the 2D frequency domain,  $d\xi d\nu = |\nu| d\nu d\phi$ , and  $|\nu|$  is the Jacobian determinant of the cartesian to signed cylindrical coordinates transformation. By applying the convolutional theorem, this equation can be rewritten as:

$$f(x, y) = \int_0^{\pi} d\phi \int_{-\infty}^{\infty} dx' p(x', \phi) h(x\cos\phi + y\sin\phi - x') \tag{2.52}$$

In equation 2.52,  $h$  denotes the co-called "ramp filter" or Ram-Lak filter:

$$h(x') = \int_{-\infty}^{\infty} d\nu |\nu| e^{j2\pi\nu x'} \tag{2.53}$$

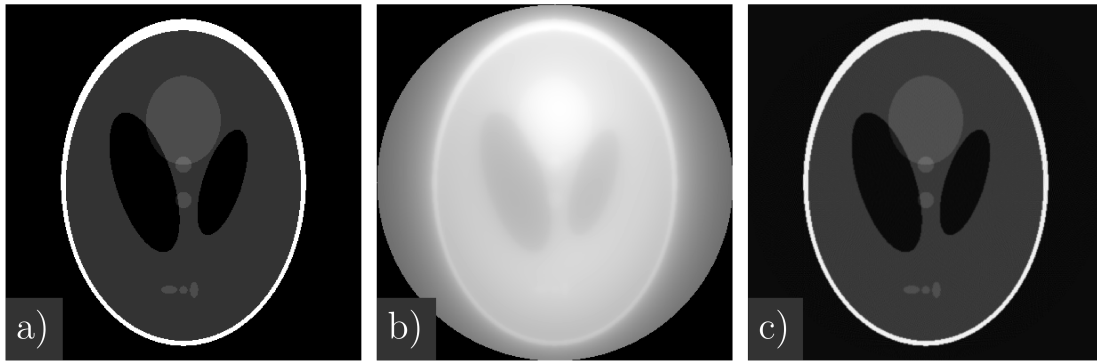


**Figure 2.8:** Backprojection (BP) vs. Filtered Backprojection (FBP): a) - ground truth of the object, b) - BP, c) - FBP with ramp filtration.

As one can see from figure 2.8 ramp filtering effect on the final reconstruction quality. Figure 2.8a represents the Shepp-Logan phantom, one of the standard test images used in the tomography algorithms performance tests. As mentioned before, higher sampling of the low frequencies in the Fourier space leads to blurry images in the absence of the filtration step. It is due to the fact that

those frequencies form smooth surfaces. In contrast, the high frequencies, responsible for sharp contours and boundaries, are more prominent after filtering.

Figure 2.9 represents the standard sinogram and sinogram with applied ramp filter obtained over  $\pi$  angle of rotation with 400 steps.

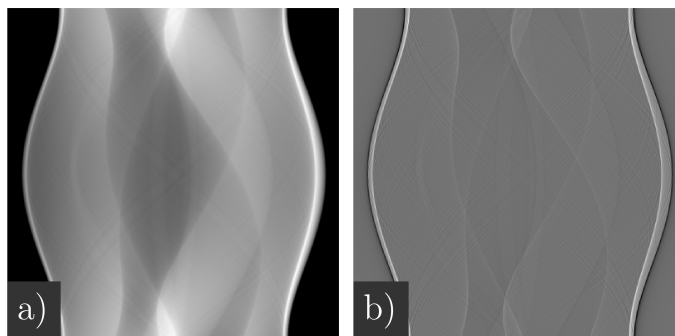


**Figure 2.9:** Ramp filtration effect on sinograms: a) - initial sinogram, b) - ramp filtered sinogram.

Generally, we can summarize the Filtered Backprojection algorithm as follows:

---

**Algorithm 2** Filtered Backprojection, 2D case with parallel beam

---

- 1: Transform projections to a sinogram and compute a row-by-row 1D Fourier image of it;
  - 2: Compute the discrete filter kernel  $\tilde{H}$  of your choice. The standard choice is ramp-filter;
  - 3: Apply the 1D filter to the sinogram row-by-row in the frequency domain and compute the filtered sinogram using inverse 1D Fourier transform;
  - 4: Perform reconstruction of the initial function by backprojecting each row of the filtered sinogram.
- 

Algorithms 1 and 2 are suitable for parallel beam geometry. In the case of cone beam geometry, one needs to take into account geometrical magnification and finite source size. One of the common approaches for tomography reconstruction with a laboratory cone beam is the modification of Filtered Backprojection algorithm made by Feldkamp, Davis, and Kress usually referred to as FDK algorithm. The basic idea behind the mentioned algorithm is that for moderate axial apertures of the detected cone beam, the acquisition geometry shall not be much different from a multi-fan beam geometry with compensation factor.

Let  $u, v$  and  $\beta$  denote cone beam coordinate system with spatial coordinates of detector and gantry angle, respectively. Moreover, let us rewrite the FBP reconstruction formula in cylindrical coordinates  $r$  and  $\varphi$  where  $r \in [0, \infty]$  and  $\varphi \in [0, 2\pi]$ :

$$f(r, \varphi) = \frac{1}{2} \int_0^{2\pi} d\phi \int_{-\infty}^{\infty} dx' p(x', \phi) h[r \cos(\phi - \varphi) - x'] \quad (2.54)$$

consequently, replace the Radon coordinates  $x', \phi$  with the coordinates of fan/cone beam geometry:

$$x'(u) = \frac{D_1 u}{\sqrt{D_1^2 + u^2}}, \quad (2.55)$$

$$\phi(u, \beta) = \beta - \tan^{-1} \frac{u}{D_1}. \quad (2.56)$$

Now let us consider the auxiliary function  $U$  weighting factor  $W_{BP}$ :

$$U(r, \varphi, \beta) = D_1 + r \sin(\varphi - \beta) \Rightarrow W_{BP}(r, \varphi, \beta) = U^2(r, \phi, \beta) \quad (2.57)$$

Thus, adding coordinate  $v$  and considering  $z = 0$ , we end up at:

$$\tilde{f}_{FDK}(\mathbf{x})|_{z=0} = \frac{1}{2} \int_0^{2\pi} \frac{1}{U^2} d\beta \int_{-\infty}^{\infty} du \left( \frac{D_1}{\sqrt{D_1^2 + u^2}} \right) g(u, 0, \beta) h'(u' - u). \quad (2.58)$$

Away from the midplane, one could notice that the line integrals in the tilted fan beam are scaled by a factor

$$\frac{\sqrt{D_1^2 + u^2 + v^2}}{\sqrt{D_1^2 + u^2}} \quad (2.59)$$

with respect to those passing from the central row of the detector. Thus, we can approximate reconstruction for  $z \neq 0$  as:

$$\begin{aligned} \tilde{f}_{FDK}(\mathbf{x}) &= \frac{1}{2} \int_0^{2\pi} \frac{1}{U^2} d\beta \int_{-\infty}^{\infty} du \left( \frac{D_1}{\sqrt{D_1^2 + u^2}} \frac{\sqrt{D_1^2 + u^2}}{\sqrt{D_1^2 + u^2 + v^2}} \right) g(u, v, \beta) h'(u' - u) \\ &= \tilde{f}_{FDK}(\mathbf{x}) = \frac{1}{2} \int_0^{2\pi} \frac{1}{U^2} d\beta \int_{-\infty}^{\infty} du \left( \frac{D_1}{\sqrt{D_1^2 + u^2 + v^2}} \right) g(u, v, \beta) h'(u' - u). \end{aligned} \quad (2.60)$$

For further simplification of the steps in the algorithm table, let us define the pre-weighting factor as:

$$\omega_{FDK}(u) = \frac{D_1}{\sqrt{(D_1^2 + u^2 + v^2)}}. \quad (2.61)$$

Finally, we can summarize the FDK algorithm as follows.

---

**Algorithm 3** The Feldkamp-Davis-Kress (FDK) method, cone beam geometry

---

- 1: Multiply the cone beam projections  $g$  by the weighting factor  $\omega_{FDK}$ ;
  - 2: Transform the weighted projections to a sinogram and compute row-by-row 1D Fourier image of it;
  - 3: Apply the 1D filter to the weighted sinogram row-by-row in the frequency domain and compute the filtered sinogram using inverse 1D Fourier transform;
  - 4: Backproject each weighted cone beam projection  $\tilde{q}/W_{BP}$  and multiply by 0.5.
-

It is important to mention how acquisition and processing factors affect the final quality of the image in the cone beam configuration. In the x-y scan plane, the spatial resolution depends on several geometrical factors: X-ray source size, scan geometry, pixels size, and movement factor. Let the  $s_F$  be X-ray source spot size,  $r_D$  and  $r_S$  is a source to sample and sample to detector distances, respectively. In that case, blur is caused by the finite size of the focal point and the impossibility of achieving a true point source:

$$b_F = \frac{r_S}{r_D + r_S} s_F \quad (2.62)$$

Taking into account blur  $b_M$  introduced by movement, acquisition blur could be summed up as follows:

$$b_{acq} = \sqrt{b_F^2 + b_M^2} \quad (2.63)$$

To calculate total blur  $b_{total}$ , one should consider sampling and image reconstruction factors:

$$b_A = c_A \cdot \Delta s \quad (2.64)$$

where  $\Delta s$  is the sampling distance and  $c_A$  is a constant representing the used reconstruction algorithm.

$$b_{total} = \sqrt{b_F^2 + b_M^2 + b_A^2} \quad (2.65)$$

## 2.10 Chapter 2 conclusion

Data acquisition and processing strategies can be tuned for the specific imaging\metrology scenario.

In the case of the Shack-Hartmann sensor providing a high flux effectivity, the low spatial resolution is overcome by the interleaving approach with a single Gaussian fitting contrast retrieval. It allows access to complete information about the lens array and imaging modalities at the cost of additional exposure time. For the Hartmann sensor, which has a high spatial resolution, a single-shot approach with the FFT-based Spatial Harmonic Analysis allows one to obtain results of measurements in real-time at the cost of final photon statistics.

Additionally, a tomographic approach allows one to access the three-dimensional distribution of the object parameters associated with the specific contrast modality, such as absorption coefficient for absorption-based tomography, decrement of refractive index  $\delta$  for phase-contrast tomography, and scattering intensity for scattering contrast tomography.



## 3 Shack-Hartmann wavefront sensor based on 2D refractive lens array

In this chapter, the design, manufacturing process (section 3.1), characterization (section 3.2), and multi-contrast imaging performance (section 3.3) of the developed Shack-Hartmann sensors will be addressed.

This chapter is based on peer-reviewed publications: "**Shack–Hartmann wavefront sensors based on 2D refractive lens arrays and super-resolution multi-contrast X-ray imaging**", Mikhaylov, A., et al. [Mikhaylov et al. 2020] and "**2d lens array for multi-contrast x-ray imaging**", Mikhaylov, A., et al. [Mikhaylov et al. 2019].

### 3.1 Design evolution and manufacturing of the Shack–Hartmann wavefront sensors based on 2D refractive lens arrays

Shack–Hartmann sensors (SHS) have been known since the early twentieth century in the visible light range. In 1900, Johannes Hartmann created the first tool to check for approximate focus, and to measure aberrations in the mirrors and lenses of large telescopes [Hartmann 1900]. This tool, called the Hartmann mask or Hartmann sensor (HS), initially consisted of an opaque screen with numerous holes. Each hole acted as an opening to isolate a small group of light beams, which could be traced to determine any deviation in direction of propagation. This deviation would correspond to the local slope of the wavefront, thus detecting wavefront modifications associated with the quality of the image. Years later, the HS was modified by replacing the apertures by an array of lenslets, thus increasing the signal-to-noise ratio [Shack 1971]. Since then, HS and SHS have continuously evolved, and the sensors have also been gaining attraction in the X-ray regime [Mayo and Sexton 2004, Reich et al. 2018, Letzel et al. 2019] in the recent past. dos Santos Rolo and collaborators demonstrated the use of a 2D array of cylindrical polymer refractive lenses as a SHSX. Furthermore, this made fast single-shot multi-contrast imaging of the dynamics of materials with spatial resolution in the micrometre range possible [dos Santos Rolo et al. 2018]. In this section, we will discuss the evolution of approaches to implement SHS in a hard X-ray regime and introduce a new parabolic-shaped lens design, consider the overall influence of the lens shape, and present a way to overcome the former limitations of the 3D DLW technology to increase the sensor field-of-view (FoV).

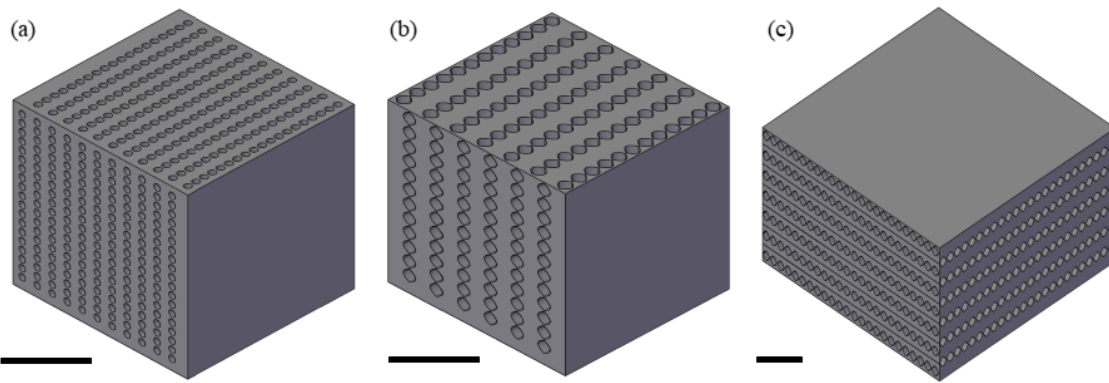


**Figure 3.1:** Evolution of SHSX designs. SHSX v1.0 (a) with circular cylindrical holes of diameter  $40\ \mu\text{m}$  and field-of-view  $1\ \text{x}\ 1\ \text{mm}$ . SHSX v2.0 (b) with parabolic cylindrical holes with apex of parabolas  $20\ \mu\text{m}$  and field-of-view  $1\ \text{x}\ 1\ \text{mm}$ , SHSX v2.1 (c) with similar parameters to v2.0 but different printings strategy leading to increase of field-of-view to  $2\ \text{x}\ 2\ \text{mm}$  (scale bars are  $0.5\ \text{mm}$ ) [Mikhaylov et al. 2020].

### 3.1.1 SHSX design based on continuous hollow cylindrical lenses

The starting pattern developed to study the influence on the lens shape is based on the prototype reported by dos Santos Rolo and collaborators [dos Santos Rolo et al. 2018]. Figure 3.1 shows the SHSX v1.0 design with cylindrical continuous lenses. The 2D focusing lenses are formed by orthogonal oriented cylindrical holes behind each other, where the interception of two perpendicular cylinders is forming a single 2D lens. The holes have diameters of  $40\ \mu\text{m}$ . The pitch of the holes in one direction is  $50\ \mu\text{m}$ . Since the refracting power of one lens is very low, ten lenses are stacked behind each other. Laterally, this results in an array of  $20\ \text{x}\ 20$  compound refractive lenses (CRL) in an area of  $1\ \text{mm}^2$ , which is an improvement of a factor of four compared to dos Santos Rolo et al. ([dos Santos Rolo et al. 2018]). However, this design has some limitations and specific features, in particular the limitation of the FoV to  $1\ \text{x}\ 1\ \text{mm}^2$  and spherical aberration of the lenses. Here we aim to study the effect of the lens shape on the performance of the array, as well as the new approaches to increasing the FoV.

### 3.1.2 SHSX design based on continuous hollow parabolic lenses

It consists of continuous 1D parabolic cavities with a radius at the parabola apex  $20\ \mu\text{m}$  and a pitch of  $170\ \mu\text{m}$ , as shown (fig. 3.1b). The overall volume of  $1\ \text{x}\ 1\ \text{x}\ 1\ \text{mm}^3$  remains, giving a total of  $12\ \text{x}\ 12$  projected spots. A second parabolic-shape prototype was developed, striving to increase the FoV. A prototype with a total volume of  $2\ \text{x}\ 2\ \text{x}\ 1\ \text{mm}^3$  was patterned (fig. 3.1c). The limitation imposed by the 3D DLW technique is bypassed by a different printing approach a prototype with a total volume of  $2\ \text{x}\ 2\ \text{x}\ 1\ \text{mm}^3$  (figure 3.1c) was explored.

## 3.2 Characterization of produced arrays

All X-ray characterization experiments were carried out at the TOPO-TOMO beamline of the KARA synchrotron facility (KIT, Karlsruhe, Germany). Characterization and focal distance

measurements of X-ray lens array were performed using a monochromatic beam with 8.5 keV X-ray energy. The acquisition of radiographic images was performed using the CMOS camera Phantom v2640, lens-coupled to a 50  $\mu\text{m}$  LYSO scintillator. The effective pixel size was 5.3  $\mu\text{m}$  (magnification approx. 2.5). One hundred images were taken for each measurement with a frame rate of 100 fps and an exposure time of 700  $\mu\text{s}$ . Before analysis, each set of 100 images was averaged to increase the signal-to-noise ratio.

### 3.2.1 Average gain and focus definition

The gain of a CRL is defined as the ratio of the on-axis image intensity in the image plane with the lens in place to the corresponding intensity without the lens [Pantell et al. 2001] and the focal length of X-ray refractive lenses [Snigirev et al. 1996] can be calculated using the equations 3.1 and 3.2 respectively:

$$G = \frac{I_{\text{beamlet}}}{I_0} \quad (3.1)$$

$$f = \frac{R}{2\delta N} \quad (3.2)$$

where R is the parabola apex radius, N is the number of stacked biconcave lenses and  $\delta$  is the refractive index decrement. The calculated focal lengths for SHSX v1.0, SHSX v2.0, SHSX v2.1 are 24.6, 41.6 and 41.6 cm respectively ( $\delta = 3.7 \cdot 10^{-6}$  and  $R=20 \mu\text{m}$ ). In this experiment, the focal length was defined as the distance at which the average gain has a maximum value. The experimental focal lengths for SHSX v1.0, SHSX v2.0, and SHSX v2.1 are 29.7 cm, 37.7 cm and 40.7 cm, respectively as shown in figure 3.22.

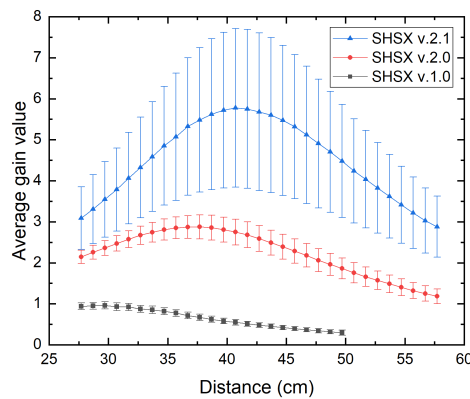


**Figure 3.2:** Dependence of average gain values for different generations of SHSX on scanning distance [Mikhaylov et al. 2020].

For all of the prototypes, the calculated focal lengths have been reproduced well. The remaining difference between the theoretical and experimental focal distances can be explained by the following factors: the refractive index decrement is calculated theoretically and does not take into

account variations in the chemical composition of the commercially available IP-S photoresist; the photoresists used to produce the different generations of SHSX are from different batches with slight variations in properties; the presence of areas with production defects effectively spreads the individual focal lengths in the array. The same arguments could be related to changes in absolute values of visibility and gain between SHSX v2.0 and v2.1 (discussed in section 3.2.4).

### 3.2.2 Surface roughness impact on gain

Figure 3.3 shows the electronic microphotographs of the printed lens array after development and critical point drying. The investigations were carried out using the scanning electron microscope Zeiss Supra 60VP in the secondary electron detection mode. The investigations were carried out using a low voltage of 0.8 kV to reduce the effect of charging the dielectric surfaces of the sample. Distortion of the shape along the edges of the frame in figure 3.3a is related to the low accelerating voltage and a large working distance, which is confirmed by the results presented in figures 3.3b,c,d. In the figures 3.3a and b the edges of the printed blocks are observed. It is necessary to pay attention to the fact that there is a slight shift of subsequently printed blocks relative to each other along the stitching lines. This shift is approximately  $1.2 \mu\text{m}$ . As figure 3.3d shows, there is anisotropy of roughness in horizontal and vertical directions. The inner surfaces of vertically oriented lenses have a much lower surface roughness in comparison with the inner surfaces of horizontally oriented lenses. This is due to the difference in the size of the laser spot in the vertical and horizontal directions, as well as related to the selected values of slicing and hatching. It is possible to use the model proposed in the [Pantell et al. 2001] to estimate the influence of the displacement of printed blocks and surface roughness. According to the calculated results, the influence of misalignment of lenses at low values is insignificant. Thus, the shift of the printed blocks relative to each other and the resulting misalignment of the lenses should not affect the focusing properties of the produced lens array. A periodicity of roughness in parallel to the lens surface direction leads to interference pattern appearing, this, in the end, can affect focusing properties of lenses. As one of the results, authors state that the larger the roughness periodicity dimension the smaller the loss of gain. For quantitative evaluation of a roughness periodicity impact on focus properties proposed following equation 3.3 [Pantell et al. 2001]:

$$p < \frac{2r_0\lambda}{s_0} \quad (3.3)$$

where  $p$  is the roughness period,  $r_0$  the distance between source and lens,  $\lambda$  the wavelength and  $s_0$  the source size in the parallel direction to the lens surface. For the TopoTomo beamline  $r_0=30$  m,  $\lambda$  (8.5 keV) = 0.1458 nm and  $s_{0,hor} = 80 \mu\text{m}$ ,  $s_{0,ver} = 15 \mu\text{m}$ . Thus, the evaluation criterion for horizontally orientated lenses is  $0.11 \mu\text{m}$ , which is undoubtedly less than the roughness period. In the case of vertically oriented lenses, it can be concluded that the roughness periodicity of the surfaces is negligibly small.

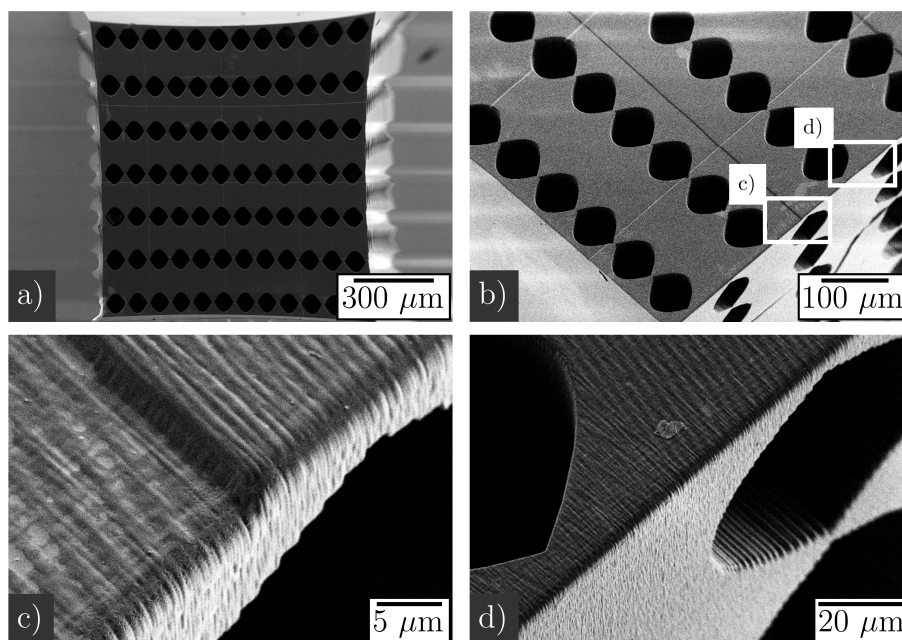


**Figure 3.3:** Scanning electron microscopy of the produced array: a) - overview image (distortion is due to low voltage mode and large working distance); b) - closeup of the edge showing tiled blocks and cylindrical holes; c) - closeup revealing misalignment of the stitching; d) - closeup showing roughness of the surface.

### 3.2.3 Average spot size and astigmatic aberration quantification

According to experimental data (fig. 3a and b), the developed lens arrays have astigmatic type aberrations. The focal planes in the x - and y-directions are located at different distances. Using the relative parameter  $\Delta$  (equation 3.4) [Barannikov et al. 2019], we can quantify the astigmatic aberrations:

$$\Delta = \left| \frac{F_x - F_y}{F_x + F_y} \right|, \quad (3.4)$$

where  $F_x$  and  $F_y$  are focal distances in x- and y-directions. A simple reason is that in the imaging process a finite source at the synchrotron is imaged onto the detector in a caustic, which shortens the horizontal distance to smallest image size [Reich et al. 2018]. A further explanation can originate in the observation that the voxel of the laser used for 3D-DLW does not have spherical symmetry, which results in a difference of lens shapes in the parallel and perpendicular directions to the printing plane. The same effect of printing anisotropy was shown in [Mikhaylov et al. 2019], Barannikov and coauthors [Barannikov et al. 2019] came to similar conclusions.

Minimizing the size of the focal spots will allow a more sensitive wavefront sampling during interleaving measurements (discussed in section 5.1) without beamlet crosstalk through extended tails. The minimum average widths of focal spots for different generations of sensors and distances at which these values were achieved ( $F_x$  and  $F_y$ ), as well as the parameter  $\Delta$ , are presented in table 3.1.

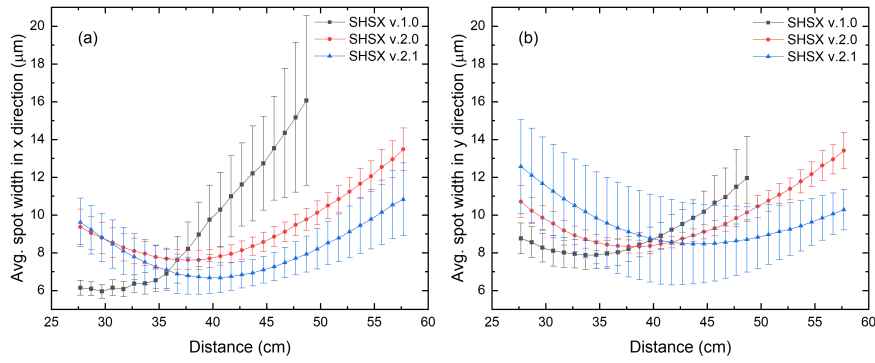


**Figure 3.4:** Dependence of average spot width in x (a) and y (b) directions for different generations of SHSX on scanning distance [Mikhaylov et al. 2020].

Sensor generation	Direction	Min. width in $\mu\text{m}$	Distance in cm	$\Delta$ in %
SHSX v1.0	$F_x$	$5.9 \pm 0.4$	29.7	6.31
	$F_y$	$7.9 \pm 0.8$	33.7	
SHSX v2.0	$F_x$	$7.6 \pm 0.5$	37.7	1.31
	$F_y$	$8.3 \pm 0.3$	38.7	
SHSX v2.1	$F_x$	$6.7 \pm 0.7$	41.7	2.34
	$F_y$	$8.7 \pm 2.1$	43.7	

**Table 3.1:** The minimal average width of focal spots at given distances and the astigmatism parameter  $\Delta$  [Mikhaylov et al. 2020].

Figure 3.5 shows the results of scanning measurements of average visibility depending on the distance from the SHSX to the detector. The results indicate that for each generation of SHSX evolution, the average value has been improved.

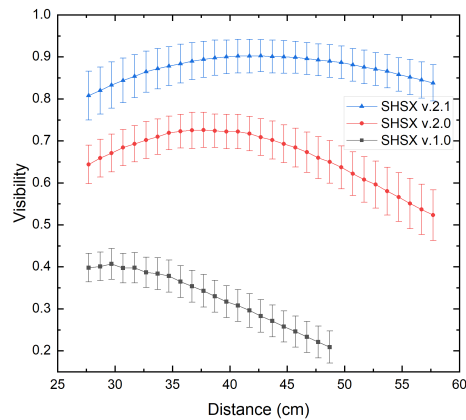


**Figure 3.5:** Dependence of average visibility for different generations of SHSX on scanning distance [Mikhaylov et al. 2020].

### 3.2.4 Homogeneity investigation: gain and visibility maps

As discussed previously in section 3.2.1, different generations of SHSX show different performances, which could be caused by structural variations due to different designs or printing defects. Gain and visibility maps are drawn at the focal points to study the homogeneity of the internal structure, qualitative and quantitative evaluation of SHSX performances. Gain maps for the SHSX v.1.0 and v.2.0 (figures 3.6a,b) show that the produced structures are relatively homogeneous. The gain of all lenses in these SHSX show uniform values with a standard deviation of 0.089 for v.1.0 and 0.293 for v.2.0. At the same time, the gain map for the SHSX v.1.0 indicates that the sensor absorbs more than it amplifies as average gain is 0.962. This is due to the relatively low X-ray energy and an effective material thickness of up to 1 mm. The gain map for SHSX v.2.1 (figure 3.6c) shows that this sensor has the highest peak gain (10.2) and average gain (5.776). However, this sensor has the largest standard deviation of 1.933. Closer to the center of the sensor, a low gain area (LG area) is detected, which is the region where the individual arrays have been stitched. From now on, the area to the right of the LG area will be called the high gain area (HG area).

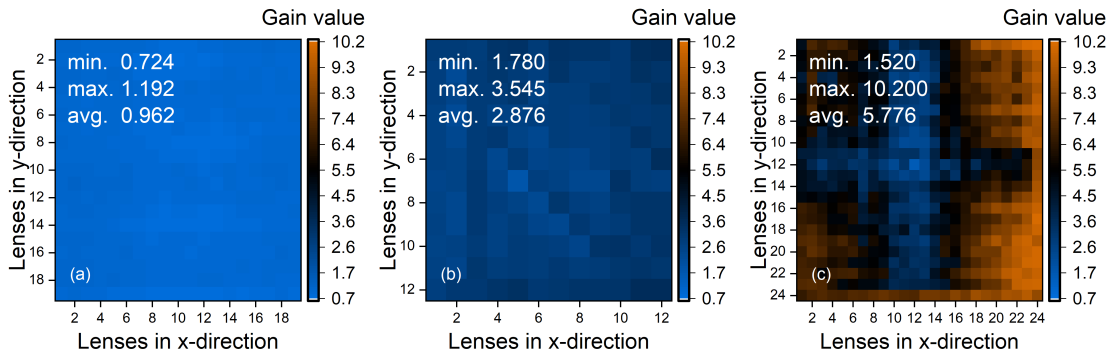


**Figure 3.6:** Gain maps of different generations of SHSX at focal distances: SHSX v.1.0 (a) at 29.7 cm; SHSX v.2.0 (b) at 37.7 cm; SHSX v.2.1 (c) at 40.7 cm [Mikhaylov et al. 2020].

The visibility  $V$  is defined as follows:

$$V = \frac{I_{max} - I_{min}}{I_{max} + I_{min}}, \quad (3.5)$$

where  $I_{max}$  and  $I_{min}$  are the local maximum and minimum intensities. Visibility maps data correlate well with the gain maps. Visibility maps of the sensors SHSX v.1.0 (figure 3.7a) and SHSX v.2.0 (figure 3.7b) show little or no internal structure defects. However, the visibility map for the sensor SHSX v. 2.1, as well as the gain map for this sensor, indicates the above-mentioned manufacturing artifacts. The nature of internal structural defects can be explained by the appearance of imperfections during the printing process, or these areas have been underdeveloped due to difficult access of chemicals, or as a combination of these factors. However, the main contribution should be due to the incomplete development process, as there are regions in SHSX v.2.1 with different focal distances.

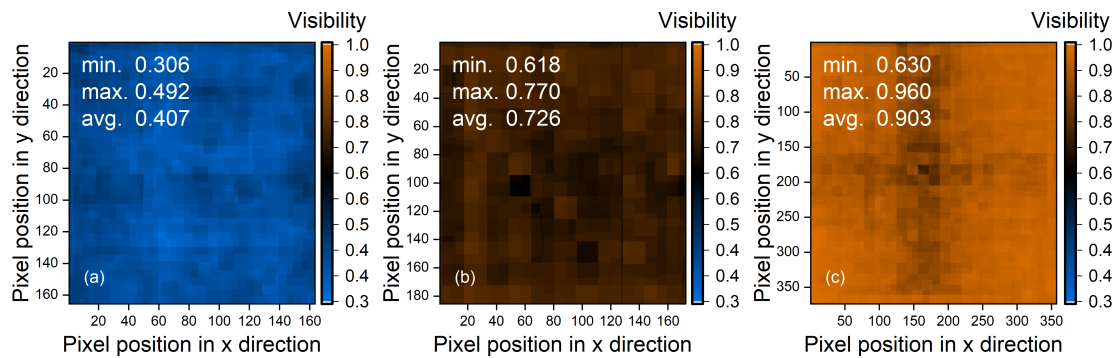


**Figure 3.7:** Visibility maps of different generations of SHSX at specific focal distances: SHSX v.1.0 (a) at 29.7 cm; SHSX v.2.0 (b) at 37.7 cm; SHSX v.2.1 (c) at 40.7 cm [Mikhaylov et al. 2020].

As a result, it can be concluded that the shown SHSX v1.0 acts more like a Hartmann sensor than a Shack-Hartmann. It performs periodic modulations of the wavefront without amplifying the beam intensity at the modulation points (figure 3.7a). Since the aim of this work was to develop the Shack-Hartmann sensors for further applications, the SHSX v1.0 was not used for further imaging performance tests. Nevertheless, before it has been shown that SHSX with cylindrical lenses acts like a SHS with a gain of approx. 8 [dos Santos Rolo et al. 2018].

### 3.2.5 Degradation of polymer lens arrays under continuous X-ray illumination

To determine the durability of the SHSX under continuous X-ray irradiation, long-exposure experiments were performed. For usage of the SHSX as regular optical devices in X-ray beamlines a certain durability is of interest.

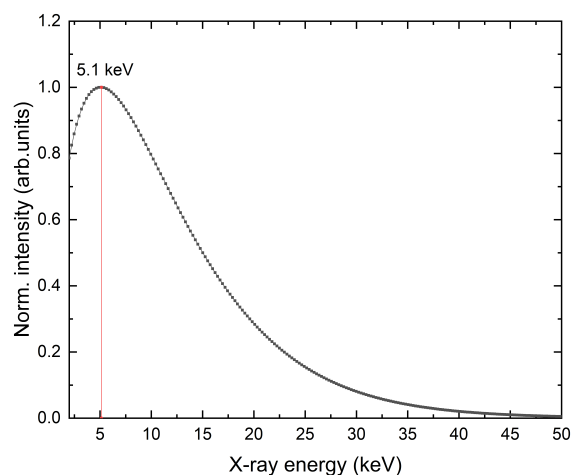


**Figure 3.8:** White beam spectra at the TOPO-TOMO beamline, KARA synchrotron facility. The maximum intensity energy is 5.1 keV [Mikhaylov et al. 2020].

The white beam spectra at the TOPO-TOMO beamline, KARA synchrotron facility is shown in figure 3.8. After an exposure of around 15 hours in white beam, visible shape changes can be observed as shown in figure 3.9. The size of the SHSX decreased leading to a reduced lens periodicity. This effect of negative photoresist shrinkage is well known to the scientific community [Kunka et al. 2014, Koch et al. 2017].

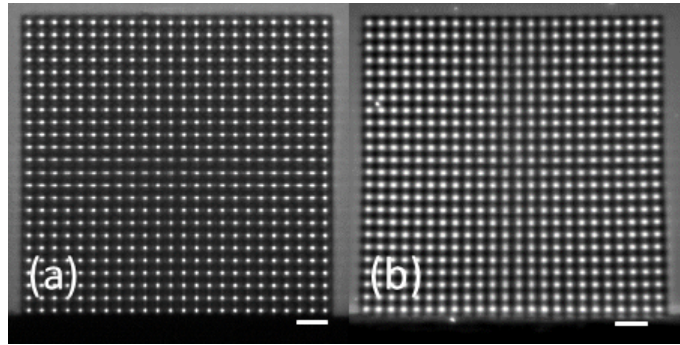


**Figure 3.9:** Images of the SHSX v.2.1 spot pattern in white beam at the beginning (a) and after 15 hours exposure (b) (scale bars are  $200\ \mu\text{m}$ ) [Mikhaylov et al. 2020].

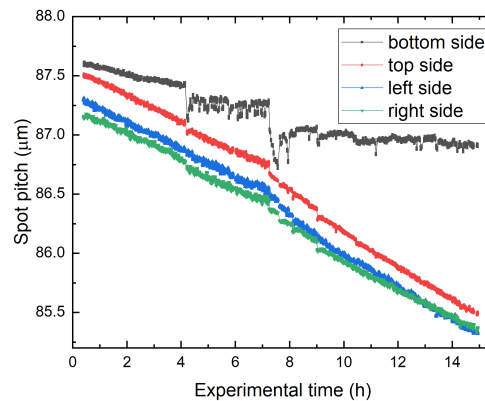


**Figure 3.10:** Evolution of the projected pattern pitch of SHSX v.2.1 after 15 hours in the white beam. The bottom side of the lens array, which was attached to the glass substrate, shows different shrinkage trend. Although average spot pitch is decreasing similarly to the other sides, absolute values are lower and abrupt step-like changes are visible [Mikhaylov et al. 2020].

To determine the shrinkage in more detail, the average spot pitch is shown in figure 3.10 for the four SHSX sides. At the beginning, the SHSX had a comparable good rectangular shape with a pitch of around  $87.5\ \mu\text{m}$ . Receiving the incident direct radiation on the frontal facet, the pitches decrease for all four sides. Apart from the bottom side, all sides have shrunk similarly. The bottom side, where the SHSX was mounted on a holder by gluing, showed less shrinkage. This indicates that the mechanical stability was reinforced due to the external rigid holder. The increased shrinkage rate after half the time is attributed to a higher X-ray flux caused by an increased synchrotron ring current.

Furthermore, the mechanical stress caused by the fixation of the bottom side of the SHSX V2.1 to the holder led to the breakage during its separation from it. This stems from buildup of internal

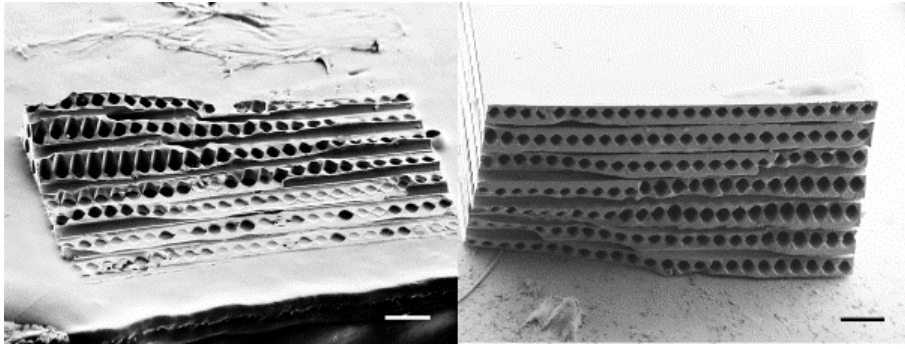


**Figure 3.11:** SEM images of the break site of SHSX v2.1 showing parabolic cylinders in vertical and horizontal directions. (scale bars are 100  $\mu\text{m}$ ) [Mikhaylov et al. 2020].

strain due to the fixed bottom part relative to the freely shrinking upper part. Figure 3.11 shows an SEM microphotograph of the broken plane parallel to the attachment on the holder. Such strain buildup may be reduced by a different mounting scheme, such as single-point attachment. Nevertheless such a shrinking should be considered for data evaluation. Inhomogenous shrinking may affect data analysis, in particular if a Fourier approach is used [Wen et al. 2010].

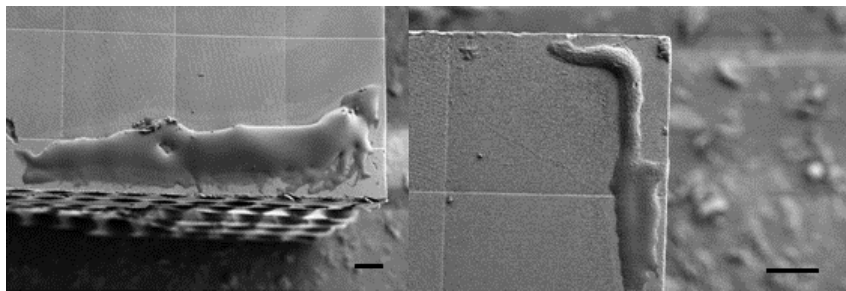


**Figure 3.12:** Influxes of unclear nature on the surface of SHSX v2.1 after 15 hours exposure, which might stems from unreacted chemicals (scale bars are 50  $\mu\text{m}$ ) [Mikhaylov et al. 2020].

Systematic investigation of the behavior of the IP-S resist in the X-ray beams, and the study of the radiation resistance are aims of our future work. We have employed here Gaussian fitting procedure for data processing [Reich et al. 2018], so that changes in the periodicity and lateral dimensions of the array are not so critical. Furthermore, the appearance of an influx of unclear nature was noticed (figure 3.12), which might stems from unreacted chemicals.

### 3.3 Multi-contrast imaging performance of SHSX v2.0 and v2.1

Tests of imaging performance were carried out using a white beam with a 0.2 mm Al filter (figure 3.8). The white filtered beam introduces chromatic aberration, which however is not larger than the imaged source, such that visibility can be largely preserved. As a test object, a diamond parabolic X-ray lens (TISNCM Troisk, Russia) was chosen due to a smooth phase gradient and reported metrology on it [Gasilov et al. 2017, dos Santos Rolo et al. 2018]. That object, as a standard test benchmark in our imaging experiments, allows us to compare new data with previous results [Mikhaylov et al. 2019]. Technological Institute for Superhard and Novel Carbon Materials

(TISNCM) in Troitsk, Russia, manufactured the diamond parabolic X-ray lens for this and previous experiments. Nominal dimensions of the diamond lens are: radius of parabola apex is  $R=200\ \mu\text{m}$ ; geometrical aperture  $A=900\ \mu\text{m}$ ; thickness  $H=500\ \mu\text{m}$  [Gasilov et al. 2017]. The diamond lens (DL) has been placed in between the SHSX and the detector. The distance SHSX to DL was 86.5 cm and DL to detector was 36.7 cm. The location of the SHSX has been chosen as near to the focal point of SHSX v2.0 at 15 keV. In figure 3.13 an example of imaging in absorption-contrast is shown. Phase-contrast and diffraction-contrast pictures can be found in the Appendix A. The lens pitch of SHSX defines the pixel size of imaging. In this experiment, the pixel size of imaging in all types of contrasts is  $85\ \mu\text{m}$ . The multi-contrast retrieval was performed by Gaussian beamlet fitting [Reich et al. 2018]. The angular resolution in differential-phase contrast mode using SHSX v2.0 is  $0.4\ \mu\text{rad}$ , SHSX v2.1 is  $0.29\ \mu\text{rad}$  (determined as the standard deviation in the undisturbed area).

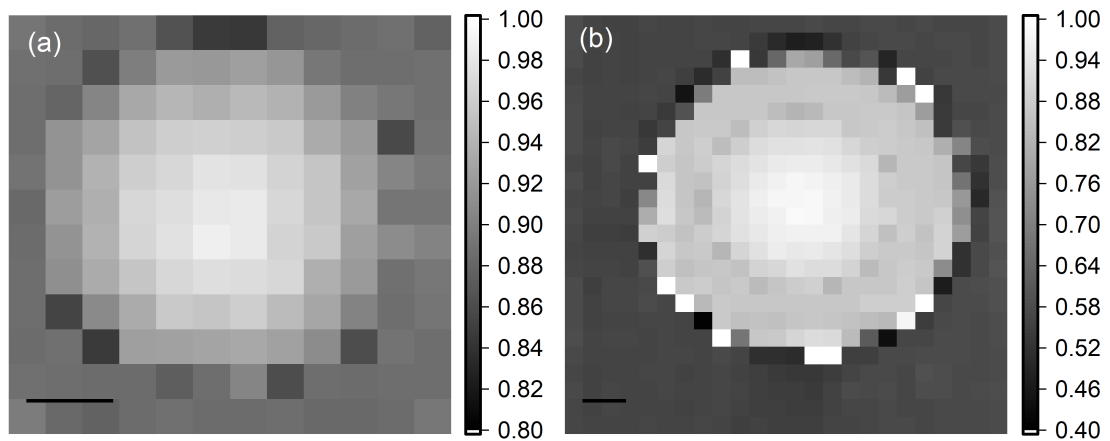


**Figure 3.13:** Images of a diamond lens in absorption contrast acquired using SHSX v2.0 (a) and SHSX v2.1 (b) (scale bars are  $200\ \mu\text{m}$ ) [Mikhaylov et al. 2020].

### 3.4 Chapter 3 conclusion

AThis chapter demonstrates that by changing the printing strategy, it is possible to increase the field-of-view by 4 times, obtaining  $2\times 2\ \text{mm}$  for SHSX v2.1 while keeping the same spot pitch as in the case of SHSX v2.0 ( $85\ \mu\text{m}$ ). Nevertheless, based on the visibility and gain characterization, the development strategy shall be adapted accordingly to reduce the risk of underdevelopment (section 3.2.4). Due to the voxel shape of the two-photon lithographic system, single lenses show a significant amount of astigmatism, which does not induce additional errors in the measurements with the flat field correction procedure. However, additional corrections may be included in the CAD model during the design stage of the lens array to increase the efficiency of the light collection. The parabolic cylindrical holes acting as continuous lenses show higher average gain and visibility, allowing one to utilize that property in case of low brightness sources. A strong effect of radiation damage in the used polymer is clearly shown. The exposure to the white beam illumination for 15 hours led to the shrinkage of the lens array, and the accumulation of the mechanical stress resulted

in the break of the array's bottom side after a slight touch by the tweezers during the detachment from the substrate.

With increased field-of-view, SHSX v2.1 has covered the whole diamond lens leading to the full-field imaging of the sample (absorption contrast imaging shown in figure 3.13). The best achieved angular resolution is estimated to be  $0.29 \mu\text{rad}$  (phase-contrast and diffraction-contrast pictures can be found in the Appendix A).

## 4 Inverted Hartmann mask made by deep X-ray lithography

In this chapter, the manufacturing process (section 4.1), characterization (section 4.2), and multi-contrast imaging performance (section 4.3) of the developed inverted Hartmann masks will be addressed. Additionally, a more complex imaging object with application to the state-of-the-art material science will be proposed (section 4.4) based on the imaging results.

Chapter 4 is grounded in the peer-reviewed publication "**Inverted Hartmann mask made by deep X-ray lithography for single-shot multi-contrast X-ray imaging with laboratory setup**", Mikhaylov, A., et al. [Mikhaylov et al. 2022].

### 4.1 Inverted Hartmann masks fabrication by deep X-ray lithography

The inverted Hartmann masks (iHM) were produced by adapting the X-ray LIGA process developed at the Institute for Microstructure Technology [Backer et al. 1982]. The German acronym LIGA stands for lithography, electroplating, and molding (*Lithographie, Galvanik, und Abformung*). LIGA is used to produce and replicate microstructured polymer and metal components with a high aspect ratio. Within this thesis, the process was adapted and finalized with the polymer photoresist stripping after the electroplating stage. The starting template for the lithography mask was a set of arrays of rectangular pillars with different periodicity and areas: 10  $\mu\text{m}$  period over a 2.5 x 2.5 cm area, 8 and 5  $\mu\text{m}$  periods over a 2 x 2 cm area. Periodic pillar arrays were produced with electron beam lithography (EBPG5200Z, Raith GmbH, Germany) on a 2.7  $\mu\text{m}$ -thick Ti membrane. Feature resolution was inspected using scanning electron microscopy (SEM - Supra VP 60, Carl Zeiss AG, Germany).

As shown in Figure 4.1, the starting lithography mask shows no presence of patterning defects. The arrays of gold pillars are consistent in shape and height over the completely patterned area. The measured periods were 5.01, 7.98, and 9.97  $\mu\text{m}$  (measurement error of 0.02  $\mu\text{m}$ ) with an average pillar height of  $4.10 \pm 0.06 \mu\text{m}$  across all periods compared to the designed 4  $\mu\text{m}$ . The inverted Hartmann masks were patterned on low-absorption substrates to ensure a higher signal-to-noise ratio (SNR) without increasing the exposure time during X-ray imaging with low-intensity sources in a laboratory configuration.

A 70  $\mu\text{m}$ -thick layer of the light-sensitive SU8-based negative photoresist formulation mr-X50 (micro resist technology GmbH, Berlin, Germany) was spin-coated onto a 200  $\mu\text{m}$ -thick polyimide

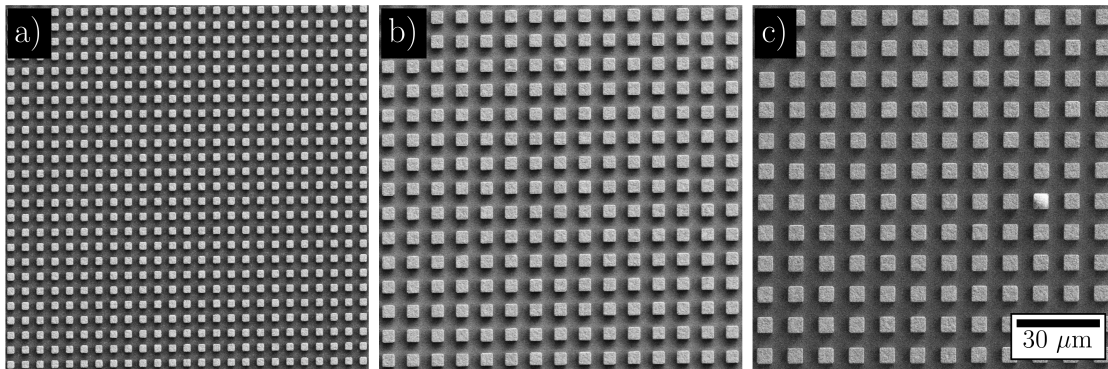


**Figure 4.1:** Scanning electron microscopy images of the lithography mask produced with electron beam lithography: 5  $\mu\text{m}$  period (a), 8  $\mu\text{m}$  period (b), and 10  $\mu\text{m}$  period (c). The scale bar is the same for (a), (b), and (c) [Mikhaylov et al. 2022].

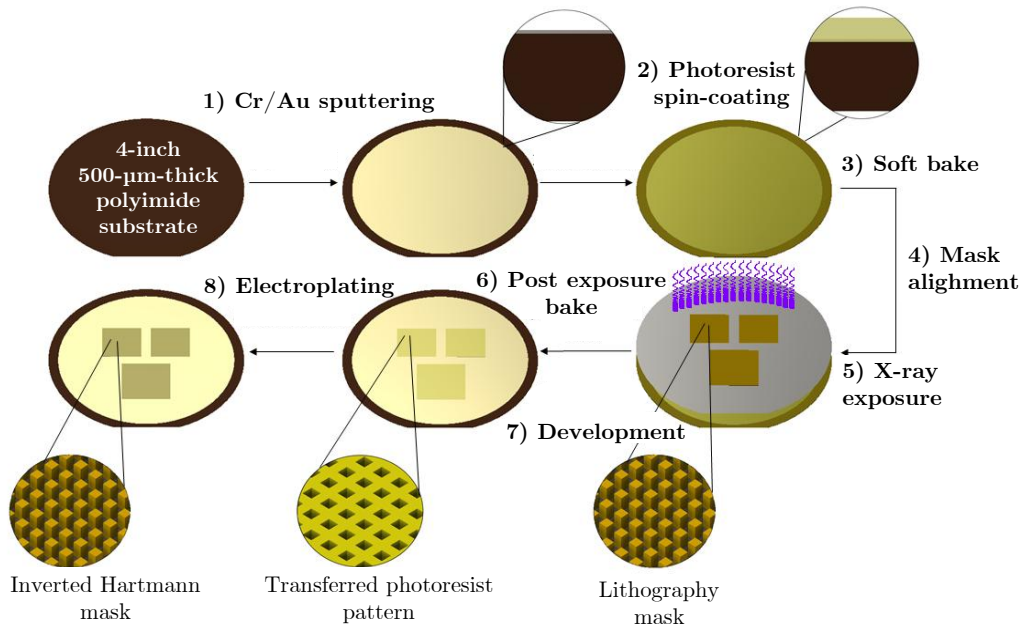


**Figure 4.2:** Deep X-ray lithography schematic sequence for the inverted Hartmann mask manufacturing. The X-ray lithography process was carried out at the LIGA 1 beamline (KARA synchrotron facility, Karlsruhe, Germany) [Mikhaylov et al. 2022].

substrate (DuPont Vespel<sup>TM</sup>), coated with a CrAu (10/70 nm) conductive layer base for electrodeposition (Figure 4.2, steps 1, 2). Soft bake was performed as follows. First, the wafer was slowly heated up to 75 °C and held at this temperature for 1 hour. Second, the wafer was slowly heated up to 95 °C and held at this temperature for 2 hours. Finally, it was cooled down to room temperature for 1 hour (Figure 4.2, step 3). The shadow of the pillar array pattern structured the photoresist using deep X-ray radiation (Figure 4.2, step 5). Then, the wafer was subjected to a post-exposure bake at 75 °C for 2 hours and afterward cooled overnight. The non-exposed parts were dissolved using the propylenglycolmonomethyletheracetat organic developer (PGMEA), rinsed with isopropanol, and then dried in a conventional oven for 4 hours (Figure 4.2, step 7). In the next step, the cavities of the inverted Hartmann mask pattern structures were filled with gold through an electroplating

process (Figure 4.2, step 8). Finally, the residual polymer was stripped using oxygen plasma at the temperature of 22°C and power of 1200 W for 30 minutes.

## 4.2 Characterization of manufactured inverted Hartmann masks

### 4.2.1 Laboratory setup

Characterization of the inverted Hartmann masks made by DXL was carried out using the X-ray setup at the Computed Lamiography/Computed Tomography Lab of the Institute for Photon Science and Synchrotron Radiation (IPS) at the Karlsruhe Institute of Technology (KIT). The laboratory source was a microfocus X-ray tube (X-RAY WorX) with a tungsten target operated at 60 kV with a target power of 3 W to achieve a focal spot size of approx. 1  $\mu\text{m}$ . The detector unit was a Perkin Elmer XRD 1621 flat panel coupled to a Gadox scintillator, with a 200  $\mu\text{m}$  physical pixel size and a 40 x 40 cm area.

Multi-contrast X-ray imaging with large period Hartmann masks made by UV lithography has already been performed with synchrotron radiation [Zakharova et al. 2019b, 2021] and in a laboratory setup [Zakharova et al. 2019a] with a Medipix detector with 55  $\mu\text{m}$  pixel size. A large-area flat panel detector has been used to test whether the method is compatible with accessible imaging detectors for medical imaging and industrial applications.

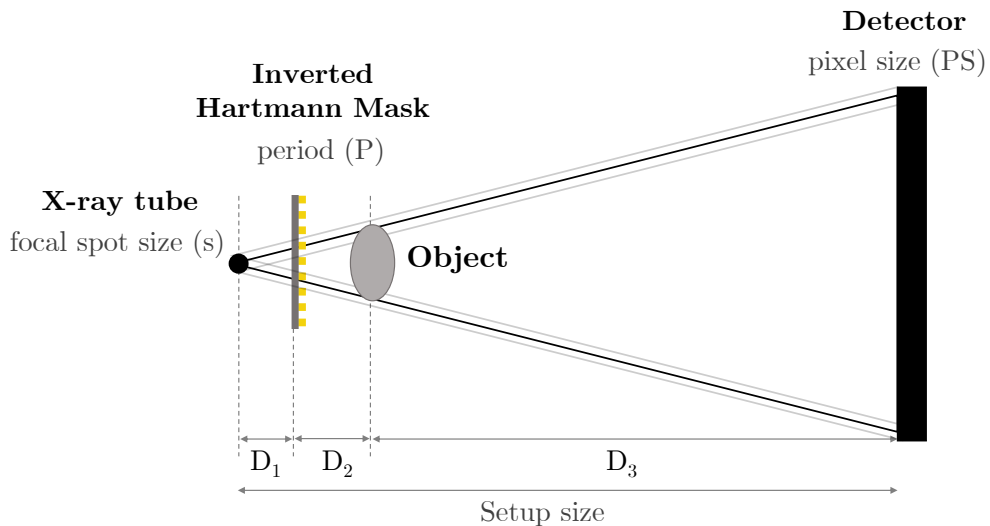


**Figure 4.3:** Experimental laboratory setup with mask-before-sample geometry. X-rays are emitted from the X-ray tube with focal spot size  $s$ . The inverted Hartmann mask with period  $P$  is located at the distance  $D_1$  from the source. The detector with physical pixel size  $PS$  records the overlapped iHM-object image. Gray divergent lines highlight the penumbral blur (see equation 2.62) introduced by the extended source [Mikhaylov et al. 2022].

The spatial resolution of the setup is defined as the period of the mask projected onto the object under investigation. The phase detection limit in such a setup can be estimated from the setup parameters and noise level in differential phase-contrast images as follows:

$$\alpha_{min} = \frac{PS(D_1 + D_2)}{D_3(D_1 + D_2 + D_3)} \cdot I_{noise}, \quad (4.1)$$

where  $\alpha_{min}$  is the minimum detectable refraction angle,  $PS$  is the pixel size,  $D_1$ ,  $D_2$ , and  $D_3$  are the distances in the setup (see Figure 4.3), and  $I_{noise}$  is defined as the standard deviation of the signal in the background (area outside the sample) for differential phase-contrast images.

To achieve the highest spatial resolution with the laboratory setup, we utilized the mask with the 10  $\mu\text{m}$  period, which was placed about 11 mm away from the sources to resolve the mask period. The source-detector distance was 150 cm, and the source-object distance for the imaging of the phantom was set to 35 mm and for the imaging of polymer composite to 26 mm. By benefiting from the magnification offered by the X-ray tube, the mask magnification of 140X and the projected period of 1400  $\mu\text{m}$  were achieved. This resulted in the sampling of 7 pixels per mask period.

## 4.2.2 Scanning electron microscopy and visibility measurements

Qualitative and quantitative characterization was performed to evaluate the structure quality after manufacturing. The scanning electron microscopy inspection reveals a homogeneous set of rectangular pillars of 5.11, 7.97, and 9.96  $\mu\text{m}$  (measurement error 0.03  $\mu\text{m}$ ) periodicity with a duty cycle of 0.5. The average gold height of the 10  $\mu\text{m}$  period Hartmann mask is  $45.92 \pm 0.07 \mu\text{m}$  (Figure 4.4).

Visibility measurements were conducted to assess the wavefront modulation performance of the produced inverted Hartmann masks. Visibility was defined in Equation 3.5 (section 3.2.4). Figure 4.5 a) illustrates a projection of the full region-of-interest and a close-up of the iHM pattern. Projected spots are well resolved and show sufficient wavefront modulation. Figure 4.5 b) presents the visibility map with the average visibility value of 0.46, which is higher than the average visibility range in the case of grating-based interferometry (0.1-0.3) [Vila-Comamala et al. 2018, Romano et al. 2020, Vila-Comamala et al. 2021]. However, the visibility is not uniform over the field-of-view: lower visibility areas are caused by the cone-beam effect due to the short-range proximity between iHM and the source.

## 4.3 Multi-contrast imaging performance of inverted Hartmann mask

To evaluate the performance of the imaging setup, we performed the measurements with a phantom sample. The phantom was tailored to simulate a woven polymer composite comprised of glass fibers and microcapsules of various sizes. To mimic the structure of interest with precise control

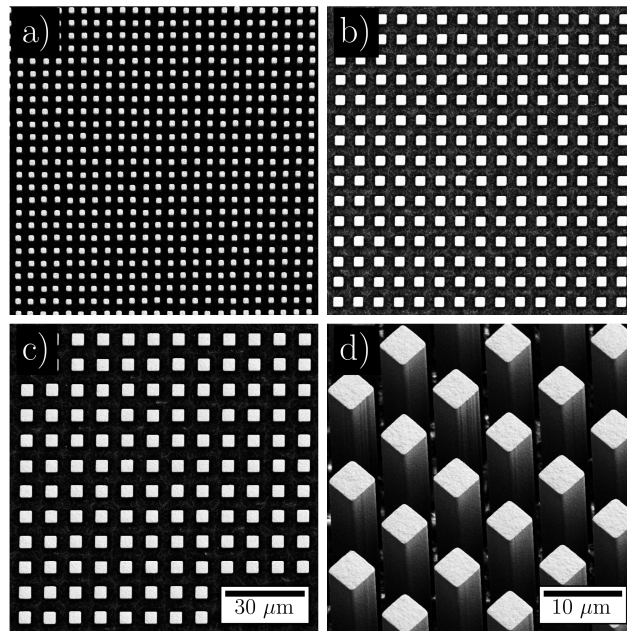


**Figure 4.4:** Scanning electron microscopy images of the inverted Hartmann masks produced with Deep X-ray lithography: 5  $\mu\text{m}$  period (a), 8  $\mu\text{m}$  period (b), 10  $\mu\text{m}$  period (c), isometric view of 10  $\mu\text{m}$  period mask (d). The scale bar for images (a) and (b) is shown in the image (c) [Mikhaylov et al. 2022].

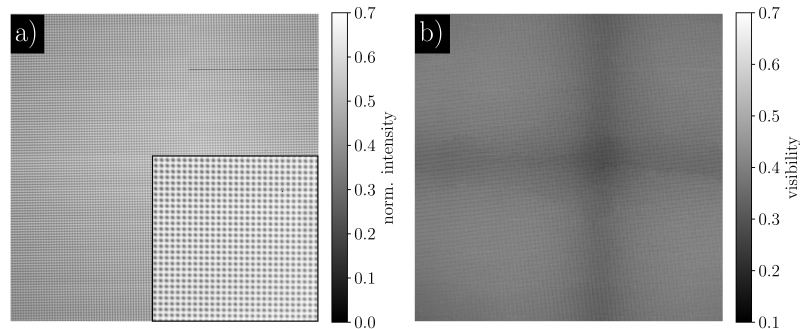


**Figure 4.5:** Inverted Hartmann mask raw projection with a close-up (a) and visibility map (b). The black horizontal stripe visible in the upper right corner of the image (a) is a line defect of defect pixels. The cross-like pattern in the visibility map (b) is caused by pillar shadowing due to the short distance between the mask and the cone-beam source [Mikhaylov et al. 2022].

over the structure size, we employed UV lithography to create polymer meshes and pillars of sizes varying from 5 to 100  $\mu\text{m}$ .

Figure 4.6 shows the outline of the phantom manufacturing process and the images of the microstructures which compose the phantom. The phantom was a tube containing low-absorbing structures (meshes and pillars) of various sizes made by UV lithography. The microstructures were manufactured with a negative photoresist (mrx-10, micro resist technology GmbH, Berlin, Germany). The photosensitive polymer layers were spin-coated on three silicon wafers with smooth surfaces and further exposed to UV light. The cross-linked photoresist patterns were subjected to PGMEA to dissolve the liquid photoresist. The manufactured structures (solid meshes and pillars)

of different sizes (5-100  $\mu\text{m}$ ) were lifted off the wafers and collected in a small vial. The photoresist pillars were put in first, most of them at the bottom of the vial. Some smaller pillars adhered to the tube's sidewalls due to electrostatic forces. After the pillars, the micromeshes were folded and placed in the vial.

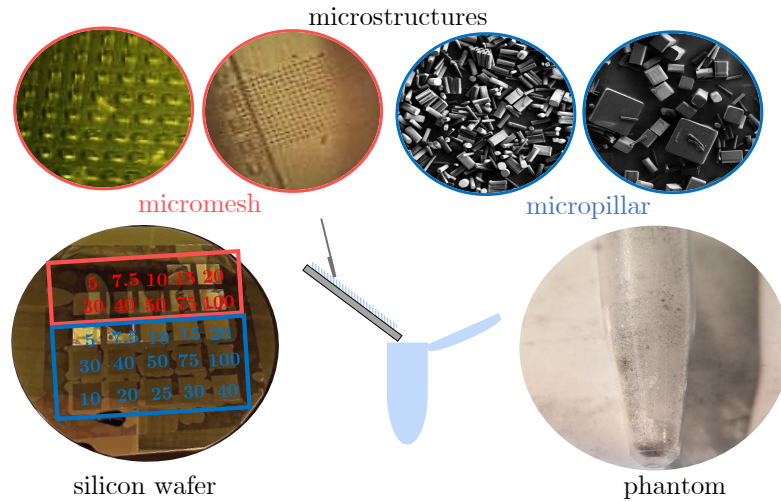


**Figure 4.6:** Phantom manufacturing process. The structures (photoresist meshes and pillars) of different sizes (5-100  $\mu\text{m}$ ) were made by UV lithography on a smooth silicon wafer, as shown in the lower left corner. Meshes and pillars are outlined in red and blue, respectively. The microstructures were lifted off the wafers and collected in a small vial (Eppendorf tube shown in the lower right corner). On top, the optical microscopy and SEM images of the structures are shown, indicating the variability of structure sizes [Mikhaylov et al. 2022].

In the imaging setup described in section 4.2.1, the X-ray imaging of the phantom specimen was performed. The distance between the source and the phantom was 35 mm; both the micromeshes and the micropillars were in the field-of-view. The spatial resolution of the setup was 30  $\mu\text{m}$ , and the phase detection limit was 0.16  $\mu\text{rad}$  (Eq. 4.1).

Figure 4.7 a) is the overlapped projections of the phantom and the periodic mask normalized by the background. The darker area in the lower part of the vial is the hot glue that fixed the phantom on the holder. Figure 4.7 b) represents the absorption image. The phase map shown in Figure 4.7 c) was reconstructed using the differential phase-contrast images in horizontal and vertical directions. Figures 4.7 e) and f) display the scattering contrasts in two directions. The scattering information was also averaged over two directions to illustrate the location of the structures with sizes below the resolution of the imaging setup (Figure 4.7 d).

In Figure 4.7, one can see how different contrast modalities provide information on various sample features. The absorption image has a low signal from the microstructures: the mesh inside and the micropillars are barely distinguishable from the hot glue. In the phase map (Figure 4.7 c), one can observe the vertical lines of the mesh while the horizontal lines are not visible. As the mesh period is at the limit of the achieved resolution, it also appears in the scattering images. In both phase and scattering images, there is a change in the signal where the micropillars are concentrated (indicated by the black arrow in Figure 4.7 e). There is a strong scattering signal from the hot glue.

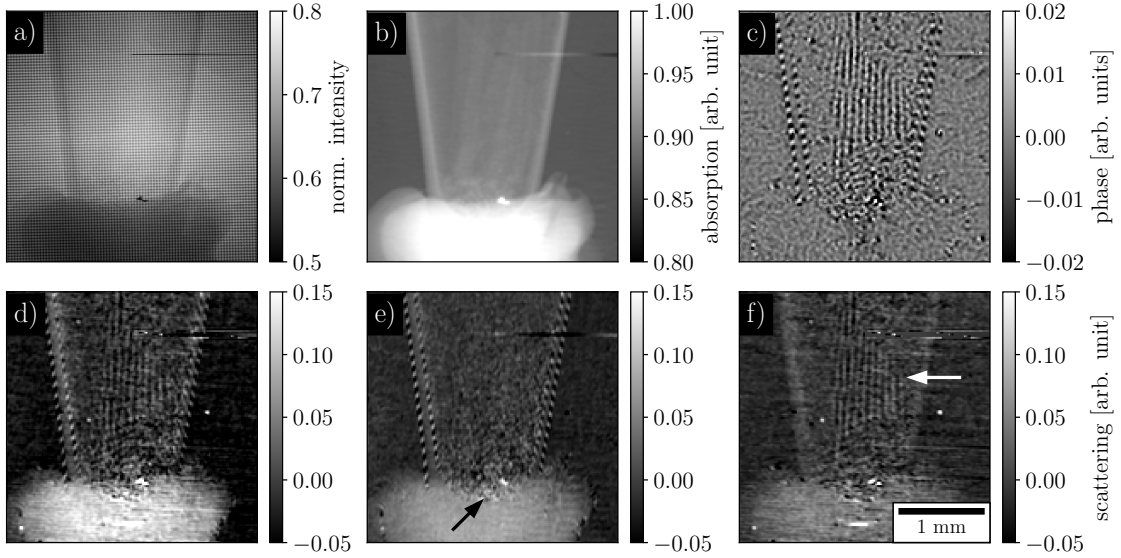


**Figure 4.7:** Imaging of the phantom sample: (a) - raw projection, (b) - absorption, (c) - phase map, (d) - sum of scattering signal, (e,f) - scattering in vertical and horizontal directions. The black arrow indicates the location of the micropillars, and the white arrow the location of the micromeshes [Mikhaylov et al. 2022].

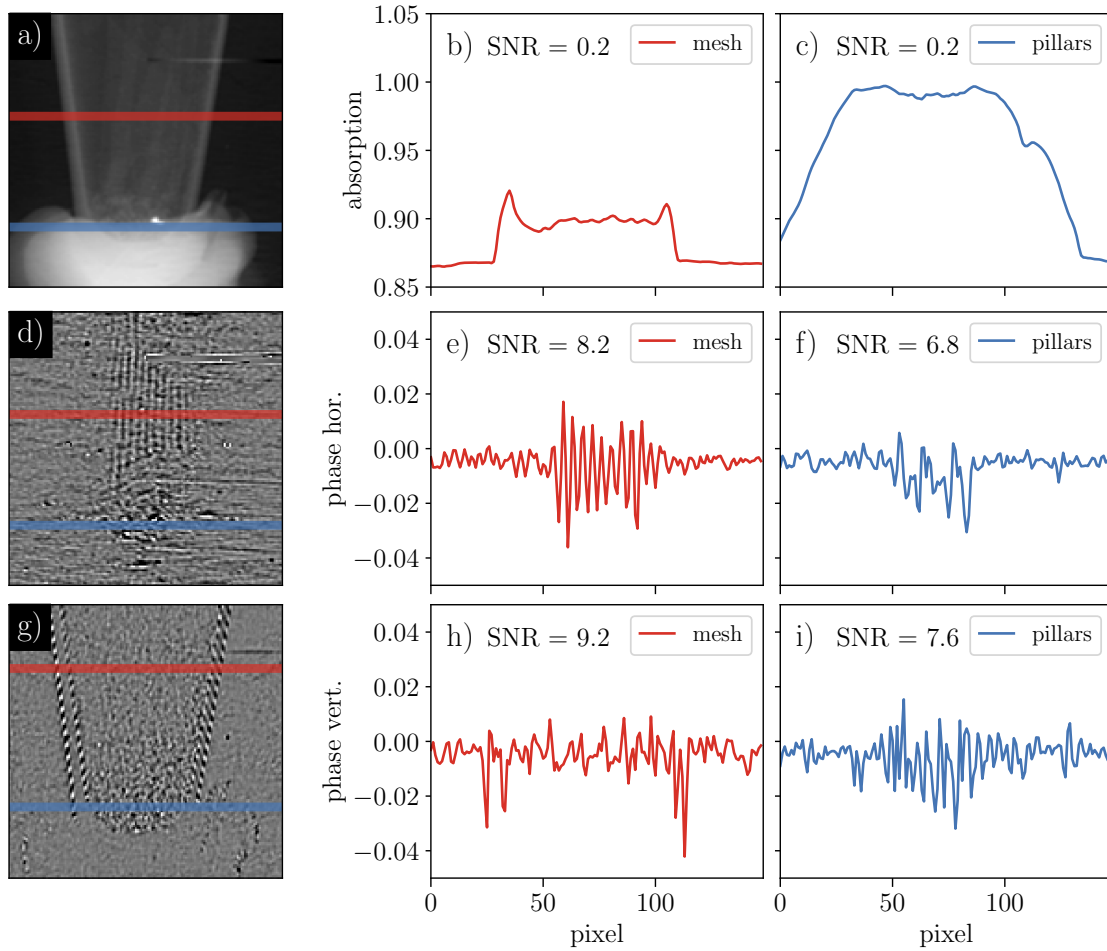
Microbubbles in the glue or an unsuppressed cross-talk between the absorption and the scattering signal can explain such an increase.

Figure 4.8 shows the absorption (a) and the differential phase-contrast images in the horizontal (d) and the vertical (g) directions. Along the blue and red lines indicated in the images, the profiles are plotted for the micromesh (red) and the micropillar (blue) locations. The profile for the horizontal differential phase contrast (Figure 4.8 e) reveals the periodic nature of the signal obtained from the micromesh with a periodicity of  $60 \mu\text{m}$ . The profile in the area where the micropillars were concentrated (blue line) also shows the change in the signal, indicating the presence of a refractive object. For all profiles in Figure 4.8, the SNR values were defined for the phase shift introduced by the micromeshes or the micropillars compared to the background signal outside of the vial:

$$SNR = 10 \log_{10} \left( \frac{\max(|S|)}{|\text{mean}(S)|} \right), \quad (4.2)$$

where  $\max(S)$  and  $\text{mean}(S)$  indicate the maximum and mean intensity of signal  $S$  (gray value) in the profile.

A similar increase in the signal is observed for the micropillars and the micromeshes (SNR between 6.8 and 8.2) since they are composed of the same epoxy-based photosensitive polymer treated in the same conditions (same refractive index). The vial walls introduced the highest phase shift (SNR = 9.2). There is a signal increase for the differential images in both directions due to the random orientations of the micropillars, but with higher background signal (Figure 4.8 f) due to the refraction from the hot glue border. One can see that there is no strong alternation of the vertical differential phase-contrast image for the area where the mesh is located. The reason could be the misalignment between the horizontal mesh lines as the mesh was folded horizontally and placed inside the vial.



**Figure 4.8:** (a) - absorption contrast; (d,g) - differential phase contrast in horizontal and vertical directions; (b,e,h) - profiles for the mesh locations outlined with red lines; (c,f,i) - profiles for the micropillars locations outlined with blue lines. The SNR value is introduced to compare the signals according to Eq. 4.2 [Mikhaylov et al. 2022].

## 4.4 Polymer composite preparation for multi-contrast X-ray imaging and tomography

Based on the imaging capabilities shown in section 4.3, it has been decided to address a more complex imaging object with application to state-of-the-art material science.

The studies of composite materials with tailored structures are of great interest to scientists working in the various areas of material science, such as construction materials development [Saba et al. 2015, Pendhari et al. 2008], bio-inspired materials [Ma et al. 2013, X Gu et al. 2016], new materials for medicine [Ramakrishna et al. 2001, Chua et al. 2021], etc. Polymer composites with glass fibers exhibit high strength and low specific weight, essential material properties for aircraft, ships, automobiles, and sports items, among other applications. The mechanical properties of glass fiber-reinforced polymers are mainly defined by the interaction between the fibers and the matrix. Engineering techniques constantly evolve to improve the material performance, increase the transfer of mechanical stresses from the matrix to the fiber and minimize the risk of failure in

the final product. These technological advances lead to new characterization approaches to study fiber-reinforced polymer composites [Stark et al. 2015, Feng and Guo 2016, Murugan et al. 2014].

The manufactured polymer composite samples could be divided into two general groups: flat samples and bulk samples.

#### 4.4.1 Polymer composite preparation: flat fiber-reinforced composites

Epoxy resin RenLam® M, based on diglycidyl ether of bisphenol A (DGEBA), as well as its hardener (Aradur HY956-2), based on triethyltetramine (TETA), were purchased from Huntsman (Sao Paulo, SP, Brazil). Aminated polydimethylsiloxane (PDMSa), BELSIL®ADM 1650, with a viscosity of ca. 1000 mPa·s and amine number of 0.6 mmol·g<sup>-1</sup>, was kindly provided by Wacker Chemie AG (Burghausen, Bavaria, Germany). Poly(urea-formaldehyde) (PUF) microcapsules filled with the self-healing agent (PDMSa) were produced as described in [Weihermann et al. 2019, Da Costa et al. 2022]. Plain weave-type E-glass fiber fabric (ABCOL Brasil Compósitos Ltda) with 300 g/m<sup>2</sup> and a density of 2.5 g/cm<sup>3</sup> was used as reinforcement.

Epoxy matrix composite specimens were prepared at GRUPOL (UDESC, Brazil) by lamination, using a vacuum bag to create mechanical pressure on the laminate during its cure cycle. Two sample types were produced: ‘Reference Composite’ (RC), composed of ‘plain weave’ glass fiber (GF) and epoxy resin (45/55 m/m, with fiber volume fraction of 26 %), and ‘Self-healing Composite’ (SHC), also composed of GF and DGEBA but with 2.0 wt% of embedded PDMSa-filled PUF microcapsules (fiber volume fraction = 23 %). The samples were produced with dimensions of 15 cm x 15 cm x 1.5 mm and afterwards cut to 35 x 9.5 x 1.5 mm for dynamic mechanical tests and X-ray lithography. RC samples were produced by mixing DGEBA epoxy resin (RenLam® M) with the curing agent (Aradur HY956-2) in a 5:1 (m/m) ratio, as recommended by the manufacturer. The reinforcement, four layers of GF fabric, was cut and placed between two layers of Peel Ply and infusion mesh to ensure the even distribution of the resin. A vacuum bag fixed with tacky tape was used to cover the mold for the vacuum lamination procedure, as presented in Figure 4.9.

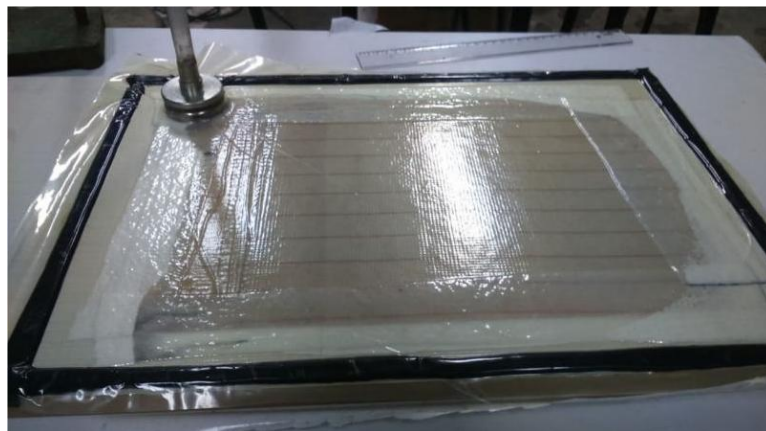


**Figure 4.9:** Preparation of the composite specimens through lamination technique in a vacuum bag [Mikhaylov et al. 2022].

SHC samples were prepared as follows: filled microcapsules were firstly dispersed in the DGEBA epoxy resin under magnetic stirring for 10 minutes. Afterward, the samples were under negative pressure for 1 hour to remove excess air within the mixture. Then, the hardener was added in a 5:1 (m/m) ratio. The lamination and vacuum-infusion procedures were the same as for RC samples. All samples were cured at room temperature under a vacuum for 2 hours, followed by a 24-hour curing period inside the vacuum bag. The laminate was removed, and a post-cure step was carried out at 100°C for 2 hours. Previous collaborative work demonstrated that only microcapsules with a diameter smaller than 60  $\mu\text{m}$  remain intact after curing [Da Costa et al. 2022].

After the post-cure step, dynamic mechanical analyses (DMA) were performed using a Netzsch model DMA 242 equipment (NETZSCH-Gerätebau GmbH, Selb, Germany). The measurements were recorded in the flexural (single cantilever) mode at a frequency of 2 Hz, 10 N force, and an amplitude of 8  $\mu\text{m}$ , in the temperature range from -90°C to 250°C with a heating rate of 2 K·min<sup>-1</sup>.

#### 4.4.2 Polymer composite preparation: bulk fiber-reinforced composites

Epoxy matrix composite specimens were prepared at GRUPOL-UDESC by vacuum-infusion molding. A stainless-steel mold (150 × 150 × 6 mm) was covered with a thin polyvinyl acetate layer. Then, ten layers of plain weave glass fiber fabric, approximately 40% of the total composite volume, were placed on the mold, which was closed with a 25 mm thick tempered glass plate. Polymer composite was composed of plain weave glass fiber (GF) and epoxy resin (60/40 m/m, fiber volume fraction = 39.33%). Composites were produced by mixing DGEBA epoxy resin (RenLam® M) with the curing agent (Aradur HY956-2) in a 5:1 (m:m) ratio, as recommended by the manufacturer. The specimens were produced with dimensions of (50 × 50 × 6 mm) for mechanical measurements and later cut to about (4.40 × 3.46 × 5.26 mm) for X-ray imaging.

### 4.5 Chapter 4 conclusion

This chapter presented the results of laboratory-based phase-contrast X-ray imaging with the inverted Hartmann mask. Adapting the LIGA technology allowed the manufacture of iHM on a low-absorbing polyimide substrate, which does not introduce beam hardening. We obtained the homogeneous arrays of gold pillars with periods of  $5.11 \pm 0.03$ ,  $7.97 \pm 0.03$ , and  $9.96 \pm 0.03$   $\mu\text{m}$  and heights up to  $45.92 \pm 0.07$   $\mu\text{m}$  without supporting structures. The gold pillars of homogeneous height significantly attenuate the polychromatic radiation emitted by the X-ray tube with a broad energy spectrum up to 60 keV. A combination of high gold pillars and low-absorbing substrate ensures sufficient wavefront modulation and high mask visibility (0.46) in a laboratory environment. A customized phantom sample comprised of micromeshes and micropillars was made by UV lithography to mimic the polymer composite structure. Differential phase-contrast images revealed sensitivity to periodic mesh structures and micropillars. Unlike absorption contrast, differential phase-contrast images provided a significantly higher SNR for the signal coming from polymer

microstructures. An increase in the scattering contrast also indicated the areas of microstructure concentration.



## 5 Application of Shack-Hartmann sensor and inverted Hartmann mask for single-shot multi-contrast imaging and tomography

The current chapter is based on the results published in the peer-reviewed publications "**Shack–Hartmann wavefront sensors based on 2D refractive lens arrays and super-resolution multi-contrast X-ray imaging**", Mikhaylov, A., et al. [Mikhaylov et al. 2020]; "**Inverted Hartmann mask made by deep X-ray lithography for single-shot multi-contrast X-ray imaging with laboratory setup**," Mikhaylov, A., et al. [Mikhaylov et al. 2022]; and the manuscript "**Single-shot multi-contrast X-ray imaging and tomography of polymer composites with inverted Hartmann mask and laboratory source**," Mikhaylov, A., et al., currently under review, submitted to the Journal of Imaging (MDPI Publishing).

### 5.1 Super-resolution X-ray multi-contrast imaging of a diamond lens with Shack-Hartmann X-ray sensor using synchrotron light source

#### 5.1.1 Super-resolution imaging setup and data processing strategy

The diamond lens, described in section 3.3, was imaged using the super-resolution approach introduced in section 2.7. With the fourfold interleaving, we obtained a nominal spatial resolution of 21  $\mu\text{m}$ . These sample-shift X-ray imaging experiments were carried out at the KARA synchrotron facility (KIT, Karlsruhe, Germany) using a white beam [Mikhaylov et al. 2019]. The radiographic images were acquired using a CMOS camera PCO.dimax with a 50  $\mu\text{m}$  thick LuAg:Ce scintillator. The effective pixel size with the lens optics is 7.3  $\mu\text{m}$  (magnification 1.5). The distance between the DL and the detector was 16 cm, and the SHSX to DL distance was 91 cm. This configuration has been chosen to achieve a suitable size of focusing spots on the DL and to perform interleaving 4 times in x- and y- directions. For each measurement, 100 images were taken with a frame rate of 0.100 Hz and an exposure time per frame of 1 ms. Before analysis, each set of 100 images was averaged to increase the signal-to-noise ratio.

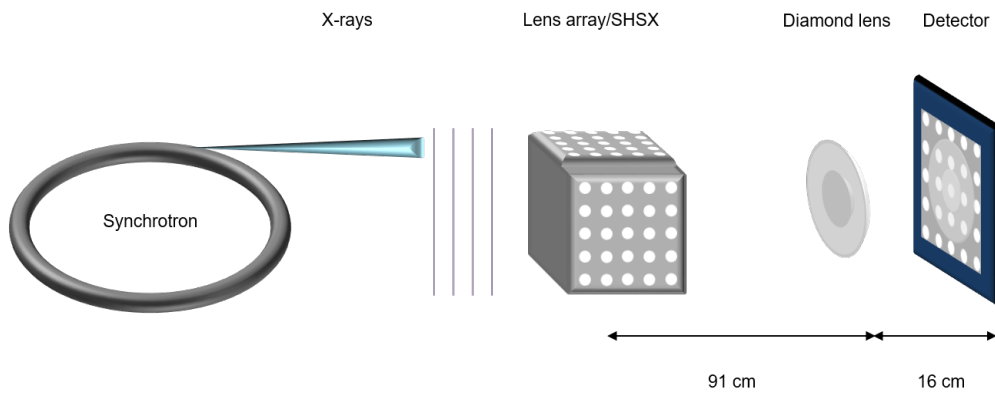


**Figure 5.1:** Experimental setup for super-resolution multi-contrast X-ray imaging with lens array-before-sample geometry. X-rays are emitted by the synchrotron. The Shack-Hartmann sensor with a period of  $85 \mu\text{m}$  is located at a distance of 107 cm from the detector. The diamond lens is located at a distance of 16 cm from the detector.

### 5.1.2 Super-resolution X-ray multi-contrast imaging of a diamond lens with Shack-Hartmann

Figure 5.2 shows super-resolution images of the diamond lens in absorption contrast acquired using SHSX v2.1. The region in the center of the diamond lens paraboloid has an average transmission of  $0.92 \pm 0.04$  with max values of 1.02 and a minimum value of 0.82 associated with the inner rim. The polymer casing around the diamond lens resulted in the low transmission of  $0.45 \pm 0.02$  in the background.

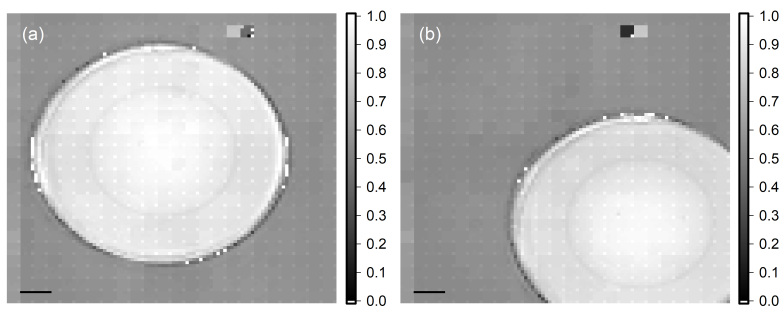


**Figure 5.2:** Super-resolution images of the diamond lens in absorption contrast acquired using SHSX v2.1: LG area (a) and HG area (b) of the SHXS v2.1 (scale bars are  $200 \mu\text{m}$ ) [Mikhaylov et al. 2020].

The angular resolution in differential-phase contrast mode is  $0.6 \mu\text{rad}$  (standard deviation of undisturbed area). In this experiment, the angular resolution is lower than in the experiment shown in section 3.3 since the distance between DL and detector is smaller, and the physical and effective pixel sizes of the used detector are bigger. Dark-field pictures can be found in Appendix B.

The differential phase contrast in all images reproduces the gradient in phase shift across the lens, which should be almost linear for a parabolic lens shape. The resolution, as inspected by the eye, is as high as the oversampling with sharp edges at the rims of the lens. Placing the lens in the center of the SHXS v2.1 produces more erroneous patches, which comprise a full  $4 \times 4$  interleave area. Thus, the error in phase shift can be ascribed to a single faulty lenslet. Nevertheless, it is shown

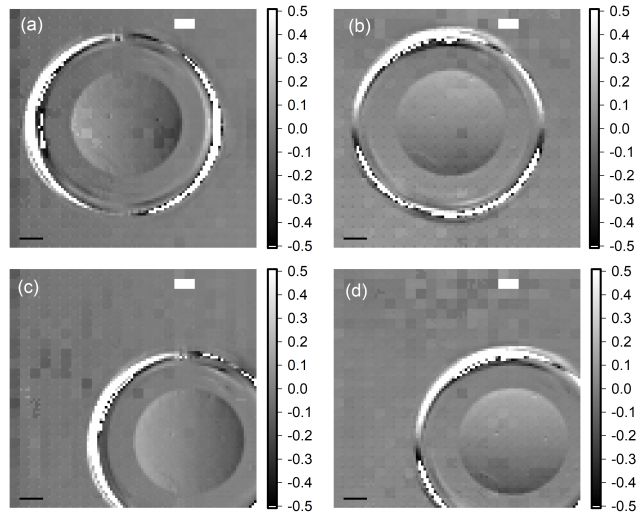


**Figure 5.3:** Super-resolution images of diamond lens in differential phase contrast acquired using SHSX v2.1: LG area (a) and HG area (b) of the SHXS v.2.1 (scale bars are 200  $\mu\text{m}$ ) [Mikhaylov et al. 2020].

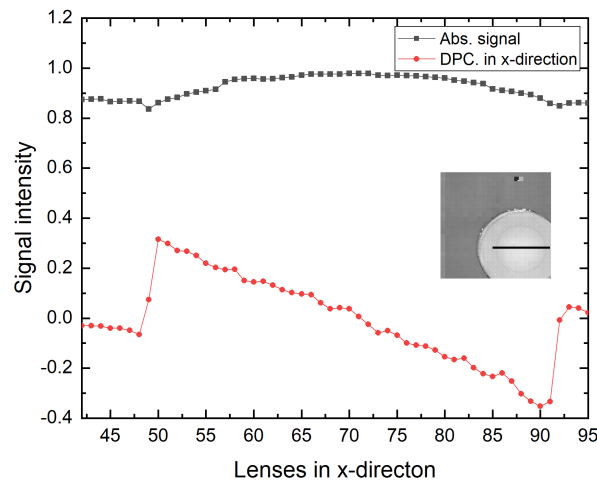


**Figure 5.4:** Comparison of normalized differential phase and absorption signals along shown lines for SHSX v2.1. in HG area [Mikhaylov et al. 2020].

that interleaving takes advantage of the small locally probed area of each beamlet on the sample. Thus, it can gain part of the resolution loss due to sampling one beamlet by several detector pixels.

## 5.2 Multi-contrast X-ray imaging of the polymer composite materials with self-healing properties

Single-shot multi-contrast X-ray imaging of polymer composite materials setup described in section 4.2. The setup (figure 4.3) was used with a distance between the source and the object of 26 mm. Spatial resolution, defined by the projected period of the inverted Hartmann mask, was 24  $\mu\text{m}$ , and the phase detection limit was 0.06  $\mu\text{rad}$  (equation 4.1). The manufacturing procedure for reference composite (RC) and self-healing composite (SHC) is described in section 4.4.1.

Figure 5.5 shows multi-contrast X-ray imaging with the inverted Hartman mask of the RC sample (figures 5.5 a,b,e,f) and the RC sample after DMA (figures 5.5 c,d,g,h). Images in the absorption contrast reveal the tailored structure of the RC sample, evidencing the glass fiber fabric used as reinforcement (figures 5.5 a,c). Bright areas on the absorption images correspond to the overlaid bundles. Due to the routine of the FFT analysis in multi-contrast X-ray imaging, absorption and scattering signals of the highly absorbing specimens could be correlated [Kaeppler et al. 2014, Vittoria et al. 2015]. In the presented measurements, maximum absorption is 30 % with the mean value of  $22 \pm 4$  %, and the thickness of polymer composite samples was ca. 3 mm. The decorrelation procedure was performed according to [Kaeppler et al. 2014], resulting in minor changes.

RC samples before and after dynamic mechanical analysis do not show a significant difference in the mean absorption signal (table 5.1). Dynamic mechanical tests did not induce any changes in the mean absorption of the sample nor a significant impact on the fiber distribution. One can see the microfiber bundles' distribution orthogonally to each other. However, it is visible that borders of vertical microfiber bundles are less defined (lower arrows in figures 5.5 a,c) than horizontal. Diverging microfibers in the vertical gaps between bundles results in the smearing of the absorption. On the other side, gaps containing less material would be more prominent in the differential phase and scattering images.

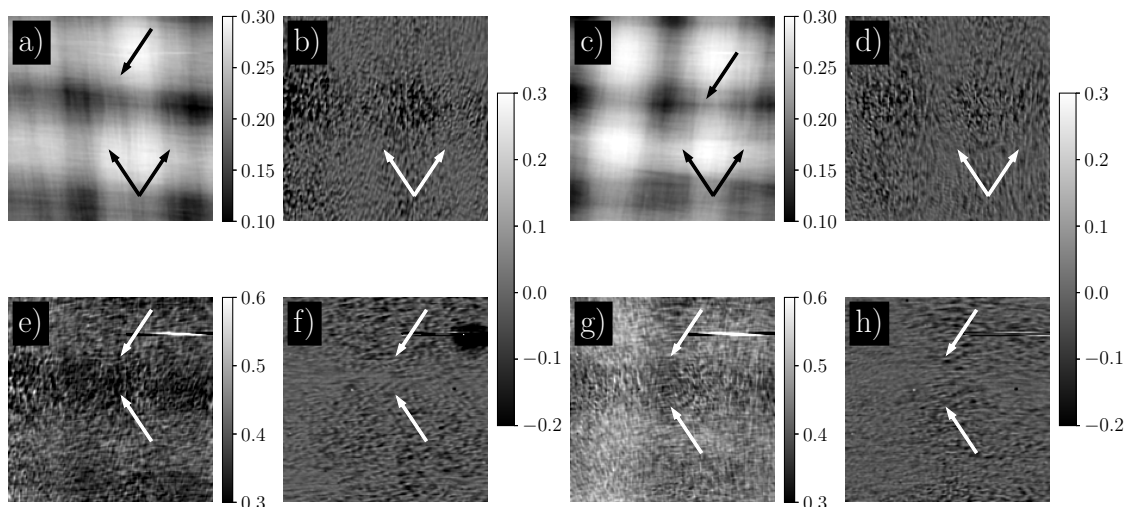


**Figure 5.5:** Multi-contrast X-ray imaging of the reference samples (a,b,e,f) and reference samples after DMA (c,d,g,h). The figures show absorption contrast (a,c); differential phase in vertical direction (b,d); scattering (e,g); differential phase in horizontal direction (f,h).

Due to the directional sensitivity of the differential phase measurements with the inverted Hartmann mask, one could notice complementary areas of high intensity in figures 5.5 a,b,f) for the reference sample and figures 5.5 c,d,h) for the RC after dynamic mechanical analysis. Figures 5.5 b,d) reveal vertical refraction patterns corresponding to the vertical gaps of the microfiber bundles (marked with arrows). Similarly, in figures 5.5 f,h), one could notice horizontal patterns corresponding to the horizontal gaps. In addition, in figures 5.5 e,g), there are horizontal and vertical patterns of lower average signal and brighter spots complementary to the absorption. This could be explained

by the nature of the scattering and the differential phase contrast in multi-contrast X-ray imaging with inverted Hartmann masks. Scattering contrast could be interpreted as a refraction signal below the angular resolution of the setup. High absorption areas containing microfibers in both directions could not be well resolved in the differential phase measurements, unlike in the scattering. On the other hand, separated diverging microfibers in the vertical and horizontal gaps result in vertical and horizontal patterns in the differential phase.

Sample	Mean absorption, $\pm 0.04$	Mean scattering, $\pm 0.03$
RC	0.22	0.38
RC after DMA	0.22	0.44
SHC	0.22	0.43
SHC after DMA	0.22	0.40

**Table 5.1:** Mean absorption and scattering value in arbitrary unit for the reference composite (RC) and self-healing composite (SHC) samples, before and after dynamic mechanical analysis (DMA).

Mean scattering signal in case of the reference sample (figure 5.5 e) is slightly lower than mean scattering signal in the RC after mechanical testing (figure 5.5 g) with values of  $0.38 \pm 0.03$  and  $0.44 \pm 0.03$ , respectively (table 5.1). This could be considered a result of X-ray scattering on the microfractures of glass microfibers and polymer matrix formed under mechanical stress.

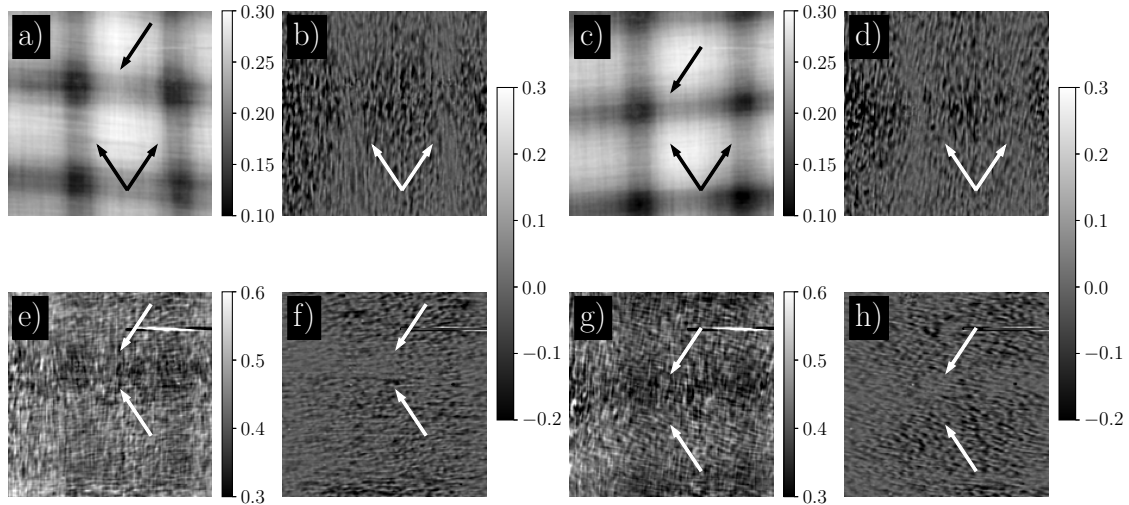


**Figure 5.6:** Multi-contrast X-ray imaging of the samples embedded with microcapsules (a,b,e,f) and sample embedded with microcapsules after DMA (c,d,g,h). The figures show absorption contrast (a,c); differential phase vertical direction (b,d); scattering (e,g); differential phase horizontal direction (f,h).

Figure 5.6 shows multi-contrast X-ray imaging of SHC samples before (figures 5.6 a,b,e,f) and after dynamic mechanical analysis (figures 5.6 c,d,g,h). Similarly to RC samples, there are no changes in mean absorption values (table 5.1). However, one could see that the microfiber bundles are more even and have well-defined borders. It was not possible to resolve microcapsules directly due to their size distribution after curing [Da Costa et al. 2022]. Differential phase images of SHC samples before (figures 5.6 b,f) and after dynamic mechanical analysis (figures 5.6 d,h) are in good

accordance with absorption images (figures 5.6 a,c); it is possible to notice vertical and horizontal stripes corresponding to the gaps between the bundles (marked with arrows). A similar pattern could be observed in the scattering images (figures 5.6 e,g). The mean scattering signal in the case of the sample with the microcapsules is higher in comparison to the reference with mean values of  $0.43 \pm 0.03$  and  $0.38 \pm 0.03$ , respectively. This can be interpreted as scattering on the microcapsules acting as scattering centers. There is no significant change in the mean scattering signal after the induced stress for the SHC samples (table 5.1). However, the RC sample exhibits higher scattering after dynamic mechanical analysis, which can be associated with microfiber fracture. This could be explained by the stress-triggered self-healing mechanism [Weihermann et al. 2019, Da Costa et al. 2022]. Micro-fractions that appeared during dynamic mechanical tests were filled by the healing agent (PDMSa) released from the broken microcapsules, leading to decreased amount of scattering centers.

## 5.3 Multi-contrast X-ray imaging and tomography of the bulk polymer composite materials

### 5.3.1 Setup and data processing strategy

Multi-contrast X-ray imaging and tomography data sets of the bulk fiber-reinforced composite (section 4.4.2) were acquired at the Computed Lamiography/Computed Tomography Lab of the Institute for Photon Science and Synchrotron Radiation (IPS) at the Karlsruhe Institute of Technology (KIT). The imaging setup consisted of a microfocus X-ray tube (XWT-225, X-RAY WorX, Garbsen, Germany) with a tungsten target. An X-ray source was operated at the 60 kVp voltage and 3 W target power which, according to the manufacturer, results in a focal point size of approx.  $1 \mu\text{m}$ . The detector was a unit Perkin Elmer XRD 1621 flat panel coupled to a Gadox scintillator, which has a  $200 \mu\text{m}$  physical pixel size and a  $40 \times 40 \text{ cm}$  area. Exposure time was 4 seconds per frame. For tomography measurements, 1024 projections over 180 degrees were acquired.

We have used the same setup described in section 4.2 and [Mikhaylov et al. 2022] with the addition of a rotary stage. The mask with a  $10 \mu\text{m}$  period, duty-cycle of 0.5, and an average height of  $45.92 \pm 0.07 \mu\text{m}$  allowed to maximize spatial resolution. The visibility shows a high average value of 0.46. Distance from the source to the inverted Hartmann mask  $D1$  was approx. 11 mm, source-to-sample distance  $D2$  was 26 mm, and source-to-detector distance  $D3$  was approx. 1500 mm. The mentioned setup allows us to achieve a mask magnification of approx. 140X (projected period of  $1400 \mu\text{m}$ ), with a sampling of 7 pixels per period of the mask.

Multi-contrast retrieval procedure was performed utilizing the FFT routine [Wen et al. 2010]. Wavefront reconstruction was achieved using the zonal method based on a modified Southwell algorithm with 10 iterations [Pathak and Boruah 2014, Reich 2019]. Directional scattering in both directions combined using equation 5.1 under the condition of isotropic small-angle scattering:

$$I_{m_{scattering}} = \frac{I_{m_{scatt,x}} + I_{m_{scatt,y}}}{2}, \quad (5.1)$$

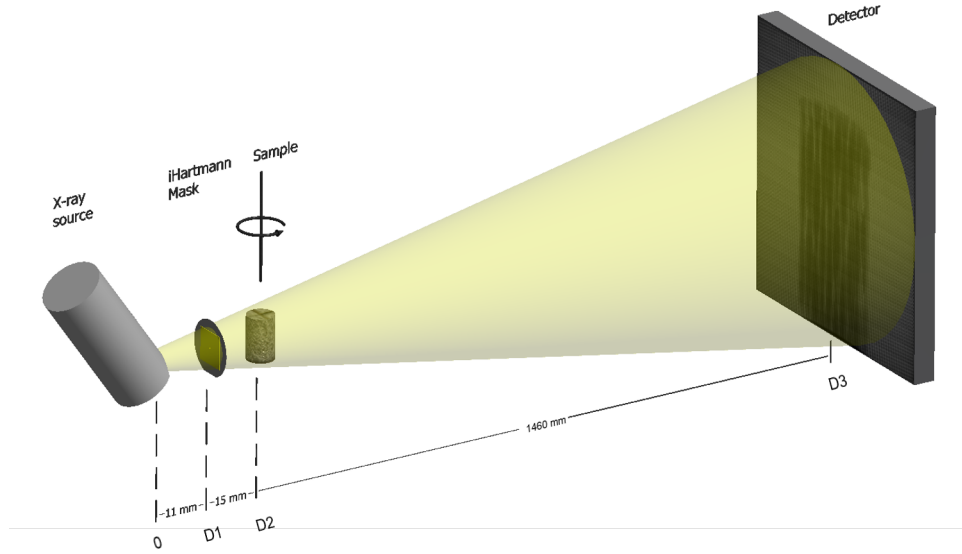


**Figure 5.7:** Experimental laboratory setup for single-shot multi-contrast X-ray imaging and multi-contrast X-ray tomography. The inverted Hartmann mask is located at the distance  $D1$ , the sample at the distance  $D2$ , and detector at the distance  $D3$  from the X-ray source.

where  $Im_{scatt,x}$  and  $Im_{scatt,y}$  are one-directional scattering images. Modification of FBP (Filtered Back Projection) algorithm for cone-beam geometry, known as FDK method [Feldkamp et al. 1984], with ramp filtration was used for tomography reconstruction of absorption and scattering data. The reconstructed volume consists of  $246 \times 246 \times 246$  voxels with a voxel size of  $24 \times 24 \times 24 \mu\text{m}$  and a volume of  $205.79 \text{ mm}^3$ . The point of origin, with respect to which we will specify slicing, is a relative point that is located in figures 5.10(a), 5.11(a), and 5.12(a) in the lower-left corner for axes  $x$  and  $y$ , and in figures 5.10(b,c), 5.11(b,c) and 5.12(b,c) in the lower-left corner for axis  $z$ . Another way to imagine the point of origin is to think of it as the closest lower-left corner of reconstructed volume, the frontal facet of which is attributed to angle 0.

### 5.3.2 Multi-contrast single-shot X-ray imaging

Figure 5.8(a,b,c) show projections in absorption contrast. Due to the tailored design of the glass fiber-reinforced composites, we clearly see a difference in structure between *en face* and *en profile* projections. Figure 5.8(d,e,f) shows bidirectional scattering contrast and (g,h,i) retrieved phase maps, reveal areas with high scattering and refraction signals corresponding to the glass fiber bundles. The interfaces between plain weave fabric tows and resin-rich areas are clearly distinguishable at  $173.52$  degrees (figure 5.8c,f). The presence of the ten layers of glass fiber fabric can be noticed, where tows and deformations are identifiable. Although the spatial resolution of the setup is not enough to resolve single separate fibers, the presence of the scattering and refraction indicates inhomogeneity of the area. On the contrary, absorption projections do not reveal structural information and show just a difference in the density of the material. Fabric reinforced composites can usually present internal microstructure defects, such as voids, fiber misalignment, and resin-rich regions, which can be caused by poor resin impregnation, residual thermal stress, and out-of-plane

stitching [Rashidi et al. 2020]. It is important to notice that in the background of phase-contrast images in figures 5.8(g,h,i), the presence of phase retrieval artifacts is clear.

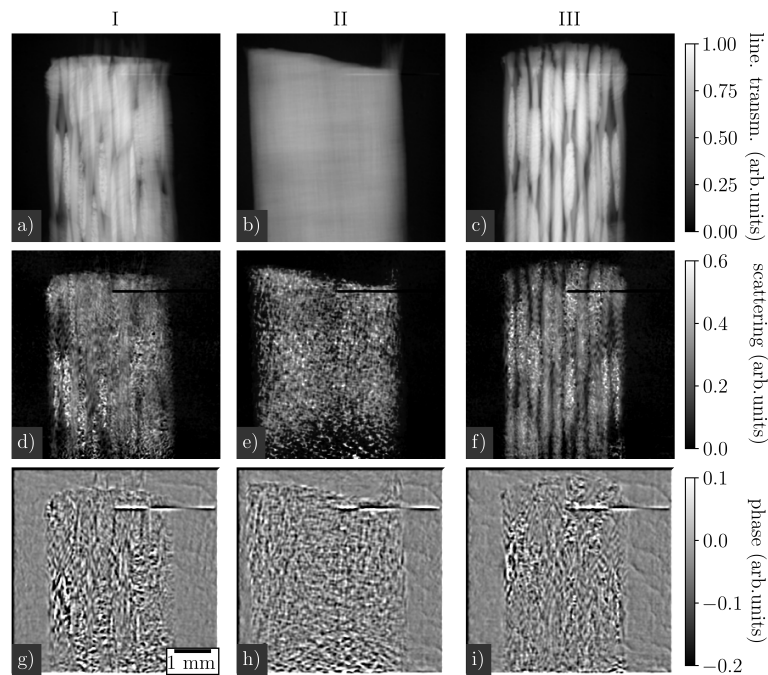


**Figure 5.8:** Multi-contrast single-shot X-ray imaging of a polymer composite. Images in absorption (a,b,c), bidirectional scattering (d,e,f) and bidirectional phase (g,h,i) contrasts at angles 0, 90, 173.52 degrees as I, II, and III, respectively. Bright white areas on the images (a,b,c) represent glass fiber bundles that have higher absorption. Same areas in the phase and scattering contrasts reveal media with higher refraction and scattering signals. Presence of a line of defect pixels might be noticed on the upper right side of each image. The scale bar is shown in image (g).

In areas near the bottom part of the sample in figure 5.8(e), one might notice decrease in scattering signal. In the corresponding area in figure 5.8(h), representing phase image, similar pattern arise. It might be explained by the transition between scattering and phase signals under certain conditions such as relative position of the fiber or fiber bundles, relative orientation etc. [Koenig et al. 2016, Esposito et al. 2022]. Although *en profile* absorption projection figure 5.8(b) shows a uniformly composed material with good density homogeneity, scattering projection figure 5.8(e) and phase projection figure 5.8(h) reveals inhomogeneous distribution of signals.

Figure 5.9 shows differential phase (a,b,c) and scattering signal (d,e,f) in vertical direction at the projection angles 162.25, 168.39 and 175.08 degrees. A background correction was performed to exclude the impact of intensity gradient using Fiji software [Schindelin et al. 2012]. Due to the design of the polymer composite sample and experimental setup, scattering and refraction signals are mixed. Projections reveal complementary information regarding glass fibers distribution. Refraction under angles below the angular resolution of the setup contributes to the scattering contrast available with this method [Koenig et al. 2016, **Mikhaylov** et al. 2022]. In the case of glass fiber-reinforced polymer composite, refraction and scattering occur at the same locations. It is due to the slightly different morphology, size, and alignment of the glass fibers in the bundle. The refraction signal appears at the edges of the fiber agglomerates. In addition, the glass fibers directly

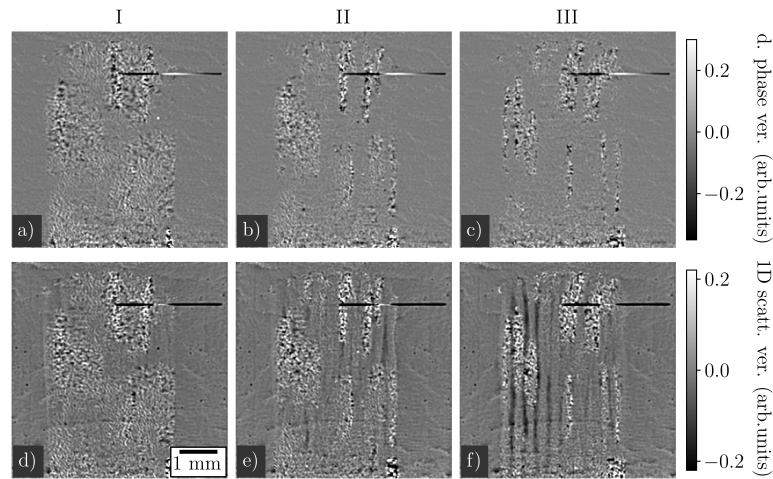


**Figure 5.9:** Differential phase (a,b,c) and scattering signal (d,e,f) in vertical direction at angles 162.25, 168.39 and 175.08 degrees as I, II and III, respectively. One could notice segmented signal of the glass fiber bundles, oriented under a small range of angles in respect to the X-ray propagation axis. Scale bar is shown in image (d).

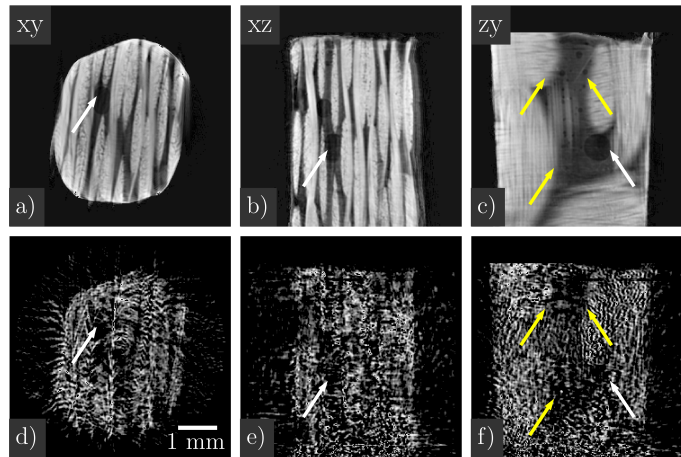
irresolvable by the measuring system show a prominent scattering signal due to their different orientations.

Special attention should be paid to the fact that fibers oriented under a slight angle to the optical axis of the setup generate strong refraction and scattering signals. In contrast, for the differential phase and scattering in vertical direction, we do not record a prominent signal in areas where fibers are vertically oriented. It could be explained by the directional sensitivity of the imaging with an inverted Hartmann mask. This approach can be potentially explored for imaging anisotropic materials. It is possible to focus on one type of feature orientation by suppressing the signal from one of the directions by the alignment of the sample relative to the optical axis. Projection of the sample does not allow one to assess the quality of the polymer composite fabrication procedure. Possible imperfections such as air bubbles, cracks, and misruns are not visible on projection due to the composite's complex structure, the presence of the refractive and scattering media, and the low absorbing properties of the defects. We conducted tomography measurements to perform the all-around examination of the inner structure.

### 5.3.3 Absorption and scattering tomography of the polymer composite

Figure 5.10 shows absorption and scattering tomography slices in positions 2.54, 2.52 and 3.72 mm relative to the point of origin of the composite sample for transverse, coronal and sagittal planes, respectively. One could notice three different density media in the polymer composite: air-containing regions, resin-rich areas with polymer matrix material (media boundaries marked with yellow arrows), and average absorption approx. 10 times higher than air and glass fiber material with average absorption approx. 17 times higher than air. The presence of the molding and curing flaws is clear. Air-containing defect with approx. 450  $\mu\text{m}$  radius, marked with white arrows, was chosen as a reference point for the slicing. Other smaller air-containing defects vary

in radius from  $75 \mu\text{m}$  to  $120 \mu\text{m}$ . Resin-rich areas and air do not show prominent scattering signal due to the absence of scattering centers in contrast to the glass fiber bundles.



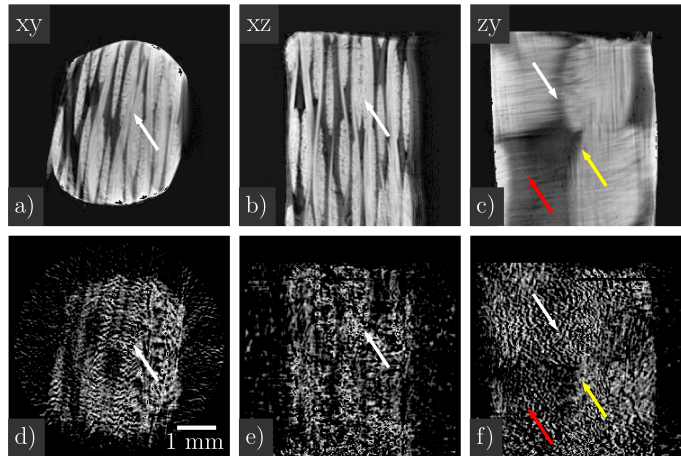
**Figure 5.10:** Absorption (a,b,c) and scattering (d,e,f) tomography slices. Upper left marks represent slicing planes: xy - transverse plane, xz - coronal plane, zy - sagittal plane. The white arrows that signalize the intersection of slicing planes point to the air-containing defect with approx. a radius of  $450 \mu\text{m}$  that were invisible in the projections. The yellow arrows indicate the borders of the different density medias. Scale bar is shown in image (d).

Figure 5.11 shows absorption and scattering tomography slices 3.17, 2.93 and 2.66 mm relative to the point of origin of the composite sample for transverse, coronal, and sagittal planes, respectively. White arrows signalize the intersection of slicing planes. On the zy-slice, one could see the borders of the resin-rich areas. Scattering tomography slice figure 5.11(f) shows a significant scattering signal in the lower-left corner of the area signalized with a red arrow compared to the resin-rich area marked with a yellow arrow. This increase of scattering might be interpreted as the presence of a thin layer of the glass fibers that is barely visible on absorption tomography figure 5.11(c). Resin-rich areas and air-containing defects exhibit, on average, similar scattering signals. At the same time, the scattering signal retrieved in glass fiber-containing regions is approx. 8 times higher.

Figure 5.12 shows absorption and scattering tomography slices 2.42, 3.19 and 3.22 mm relative to the point of origin of the composite sample for transverse, coronal and sagittal planes, respectively. White arrows signalize the intersection of slicing planes. The zy-slice shows orthogonal bundles of glass fibers. They give a prominent absorption and scattering signal. Scattering and density distribution are in good compliance. In the figure 5.12(f), a prominent scattering signal appears in the area marked with a yellow arrow. The same area in figure 5.12(c) has slightly increased absorption signal. That could be explained by the presence of a thin layer of glass fibers, similarly to the one signalized by the red arrow in figures 5.11(c,f).

Segmentation of the acquired tomographic data was performed using Fiji software [Schindelin et al. 2012] and open-source 3D Slicer software, version 4.11.2 (<https://www.slicer.org>) [Fedorov et al. 2012].

Figure 5.13(a) shows a very characteristic profile of the plain weave fabric layers present in the composite, while figures 5.13(b,c,d), taken on transverse, coronal and sagittal planes, respectively,



**Figure 5.11:** Absorption (a,b,c) and scattering (d,e,f) tomography slices. Upper left marks represent slicing direction: xy - transverse plane, xz - coronal plane, zy - sagittal plane. The white arrows signalize the intersection of slicing planes. A thin layer of the scattering media is indicated with the red arrow. The yellow arrows point to the border of the pure resin-rich region. Scale bar is shown in image (d).

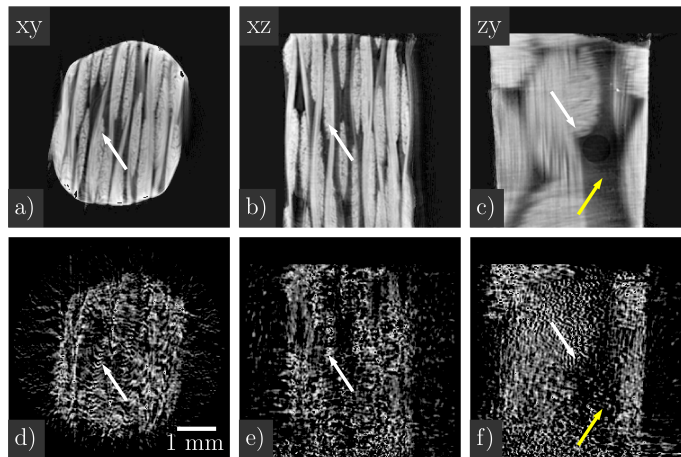


**Figure 5.12:** Absorption (a,b,c) and scattering (d,e,f) tomography slices. Upper left marks represent slicing direction: xy - transverse plane, xz - coronal plane, zy - sagittal plane. White arrows signalize the intersection of slicing planes. Clear presence of the air-containing defect with approx. a radius of  $495 \mu\text{m}$  that were invisible in the projections. Yellow arrow indicate thin layer of glass fibers contributing to scattering signal. Scale bar is shown in image (d).

evidence boundaries of volume-of-interest inside the composite structure. As shown by the rendering of the volume-of-interest (figure 5.13a), segmentation of the absorption signal associated with voluminous glass fiber agglomerates works well in the mentioned composite. This is due to the high difference between glass fiber bundles, polymer base, and air absorption signals, as stated in section 5.3.3. However, the segmentation of separate thin layers that exhibit poor absorption signals could be a challenging task. The fiber orientation information can be extracted from the bidirectional scattering and differential phase signals (figure 5.9), and volumetric scattering data (figures 5.10, 5.11, 5.12(d,e,f)). Applying approaches similar to those described by Kim et al. ([Kim et al. 2020]), serves as a multipurpose tool for predicting the behavior of composite materials with tailored structure, and the volumetric data can be used in computer modeling ([Nikishkov et al.

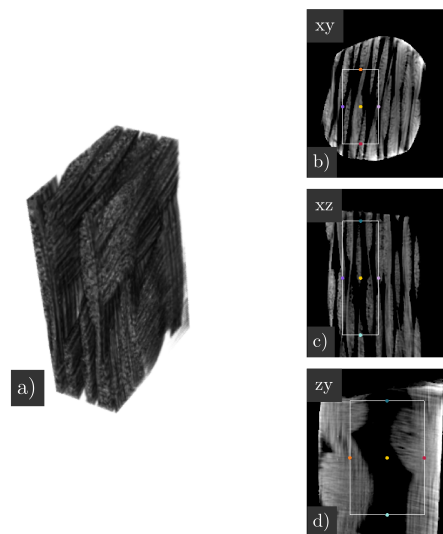


**Figure 5.13:** Segmentation of the glass fiber bundles based on absorption tomography data: (a) volume-of-interest; (b,c,d) are transverse, coronal, and sagittal planes, respectively, with the marked region of interest.

2013, Czabaj et al. 2014, Sencu et al. 2016]). In addition, applying inverted Hartmann masks open a new window to distinguish between composite with similar absorption cross-sections and low-absorbing materials.

## 5.4 Chapter 5 conclusion

This chapter shows the results of implementing Hartmann-based optics for wavefront monitoring, multi-contrast imaging, and tomography. Despite sharing basic general principles, the Shack-Hartmann and Hartmann approaches have different advantages and preferable applications that were observed and proved.

The experiments here demonstrated that the Shack-Hartmann wavefront sensor for hard X-rays based on 2D refractive lens arrays is a good option for fast wavefront monitoring and single-shot multi-contrast imaging, providing an angular resolution of approximately  $0.29 \mu\text{rad}$ . Even in the case of using a sample-shift technique by interleaving measurements to increase the spatial resolution to  $21 \mu\text{rad}$ , the measurement time spent is still in a range of seconds, which is much less than in the case of using other wavefront-sensitive instruments. Despite possible concerns, chromatic aberrations in white-beam illumination are not detrimental to the measurement but only gradually reduce sensitivity.

As proved, the Hartmann wavefront sensors based on inverted Hartmann masks could be used for single-shot multi-contrast imaging and tomography of complex polymer composites with tailored structures.

In section 5.3.3, for the first time, are demonstrated the capabilities of multi-contrast X-ray imaging and computed tomography with an inverted Hartmann mask to investigate fiber-reinforced polymer composite materials in a laboratory environment. Absorption-only data allows the segmentation

of areas with different absorption properties without insight into the structure. With the addition of refraction and scattering information, fine structures with features below spatial resolution are revealed.

The tomographic approach made it possible to resolve density media such as air-containing defects and resin-rich areas with approx. 10 times higher absorption relative to air and bundles of glass fibers with approx. 17 times higher absorption relative to air. Glass fibers exhibit approx. 8 times higher scattering signal than air or resin-rich areas, which enhances the visibility of thin layers of bundles with low absorption. The air-containing defects with radii ranging from 75  $\mu\text{m}$  to 495  $\mu\text{m}$  were not visible on projections due to surrounding media with high absorption, refraction, and scattering properties.

Figure 5.13(a) shows a very characteristic profile of the plain weave fabric layers present in the composite, while figures 5.13(b,c,d), taken on transverse, coronal and sagittal planes, respectively, evidence boundaries of the volume-of-interest inside the composite structure. As shown by the render of the volume-of-interest (figure 5.13a), segmentation of the absorption signal associated with voluminous glass fiber agglomerates works well in the mentioned composite. This is due to the high difference between absorption signals of glass fibers bundles, polymer base, and air, as stated in section 5.3.3. However, the segmentation of separate thin layers that exhibit poor absorption signals could be a challenging task. The information on fiber orientation could be extracted from the bidirectional scattering and differential phase signals (figure 5.9) and volumetric scattering data (figures 5.10, 5.11, 5.12(d,e,f)). Applying approaches similar to those described by Kim et al. ([Kim et al. 2020]), this method can serve as a multipurpose tool for predicting the behavior of composite materials with tailored structure, and the volumetric data can be used in computer modeling ([Nikishkov et al. 2013, Czabaj et al. 2014, Sencu et al. 2016]). In addition, this method opens a new window to distinguish between composite with similar absorption cross-sections and low-absorbing materials.



## 6 Summary and Outlook

### **Shack-Hartmann wavefront sensor for hard X-rays: design evolution, fabrication and characterization**

Adapting the classical Shack-Hartmann sensor approaches for the visible spectrum to the field of hard X-rays resulted in a versatile instrument suitable for multi-contrast imaging and beam monitoring applications. The development of true 3D additive manufacturing techniques, such as Two-photon 3D direct laser writing, has enabled a cost-efficient production of lens arrays with suitable characteristics for focusing X-rays in the 2-30 keV energy range. The periodic surface roughness of the sidewalls of the fabricated Shack-Hartmann sensors, when used in the single-shot configuration, does not influence the final results. Thus, nanoscale 3D additive manufacturing allows a smooth but rapid transition from prototyping to application stages at a fraction of the costs of other lithography technologies.

Lenses with 20  $\mu\text{m}$  radii were successfully manufactured, as shown in section 3.1. The design evolution from circular to parabolic of the 1D hollow cylindrical lenses has reduced the influence of spherical aberrations and increased the average gain of the lens array from 0.962 to 5.776 resulting in the increase in average visibility from 0.407 to 0.903 (section 3.2.4). The field-of-view was increased by a factor of 4 with the adaption of a novel manufacturing strategy (section 3.1.2). However, the photoresin shrinkage has a noticeable effect and require further research to evaluate the possible working time for individual lens array.

As suggestions for the further design development of this technology, the following steps are proposed:

1. The use of low-absorbing substrates such as silicon nitride and polyimide;
2. Development of approaches to account for the block displacement during stitching throughout the printing process by adding custom margins at the 3D modeling step;
3. Development of the implementation approaches of 'skeleton' printing methods, with consecutive post-writing exposure;
4. To combine several lens arrays by aligning manually to increase the field-of-view;
5. Implementation of machine learning methods for data processing: centroid prediction, contrast retrieval, wavefront reconstruction, final image analysis and correlation.

### **Inverted Hartmann masks for multi-contrast imaging and tomography: design, fabrication and characterization**

The X-ray LIGA technology adaptation allowed patterns of inverted Hartmann masks with periods 5.11, 7.97, and 9.96  $\mu\text{m}$  with average errors of 2.22, 0.37, and 0.40 %, respectively. For the first time, patterned free-standing 2D structures with homogeneous distribution in height and smooth side walls were achieved on 2x2 and 2.5x2.5 cm areas. The pillar arrays are defect free, without collapsing structures or waviness. The absence of supporting structures ensures an increase in the final image quality. A low-absorbing substrate leads to a high wavefront modulation, which results in high visibility of 0.46 in the laboratory environment.

From experience gained during the patterning, it is possible to fabricate two-dimensional structures with even larger areas and smaller periods for specified applications using the approaches described in section 4.1.

#### **Wave-front monitoring with Shack-Hartmann sensor for hard X-rays**

The robustness of the Shack-Hartmann sensor was proved by characterizing a refractive diamond lens in the parallel white beam configuration. The angular sensitivity ranged from 0.29 to 0.6  $\mu\text{rad}$ , depending on the detector's chosen distances and pixel size.

The implemented super-resolution approach increased the spatial resolution by a factor of 4 (21  $\mu\text{m}$ ) at the cost of 16 measurements per final frame. However, the overall acquisition time is still in the range of seconds which is better or comparable with similar phase-sensitive methods.

One of the suggestions for further development of the wavefront sensing technology is to manufacture the wavefront sensor with a detection system and stages as a single unit. Accordingly, to mount the lens array on an xy-piezo stage and a motorized stage together with a scintillator, optical magnifying system, and detector. An xy-piezo stage allows super-resolution measurements, and a motorized stage is needed to increase a lens array-scintillator distance for different energies. Thus, such a unit is a ready-to-use tool for wavefront metrology at any beamline.

#### **Multi-contrast X-ray imaging with inverted Hartman mask in laboratory environment**

The multi-contrast imaging of the in-house made phantom revealed the high sensitivity of the single-shot X-ray approach, keeping the simplicity using a sole 2D Hartmann mask. The phase-sensitive signal shows higher SNR compared to the absorption signal. The images in differential phase and scattering contrasts made it possible to observe the inner structure of the phantom sample, which has poor absorption contrast. Furthermore, it was possible to quantify the period of the polymer mesh rolled within the phantom. The significant increase in the scattering signal enhanced the areas with high microstructure concentration.

The implemented imaging approach was used to study fiber-reinforced polymer composite materials with self-healing properties under mechanical stress. The absorption and differential phase contrast showed the tailored structure of the polymer composites and the glass fibers distribution, while the scattering contrast allowed to observe changes in the internal structure below the angular and spatial resolution of the setup. The addition of the healing agent-containing microcapsules and damage associated with the mechanical stress lead to the appearance of the new scattering

centers. The induced scattering signal indicates uniform microfracture propagation and microcapsule distribution across the sample area. The difference between the mean scattering signal of the reference composite material and material with microcapsules containing a healing agent made it possible to track the self-healing process.

The achieved angular sensitivity ranged from 0.06 to 0.16  $\mu\text{rad}$  in the polychromatic cone-beam configuration, depending on the sample-source distances.

### **Multi-contrast X-ray tomography with inverted Hartman mask in laboratory environment**

This research demonstrated the first combination of single-shot multi-contrast X-ray imaging with an inverted Hartmann mask within the tomographic setup. This approach made it possible to obtain volumetric information on the polymer composite material's properties. Along with absorption information, it allowed accessing the distribution of the scattering signal produced by sub-micrometer size structures unresolved by the imaging system.

Although in the case of the investigated material, the absorption coefficients of air, polymer-base, and glass fibers are very distinct, the employment of the inverted Hartmann masks is potentially beneficial for studying composites with similar absorption coefficients and low-absorbing materials.

Single-shot with a sole optical element approach keeps the acquisition rate similar to the conventional absorption CT/ $\mu\text{CT}$ , while benefiting from the simultaneous multi-contrast information. In addition, simplicity and robustness allow the implementation of the presented configuration in commercially available CT/ $\mu\text{CT}$  scanners, existing radiography laboratories, or complex setups for correlative investigations.



## A Phase-contrast and scattering contrast imaging of the diamond lens

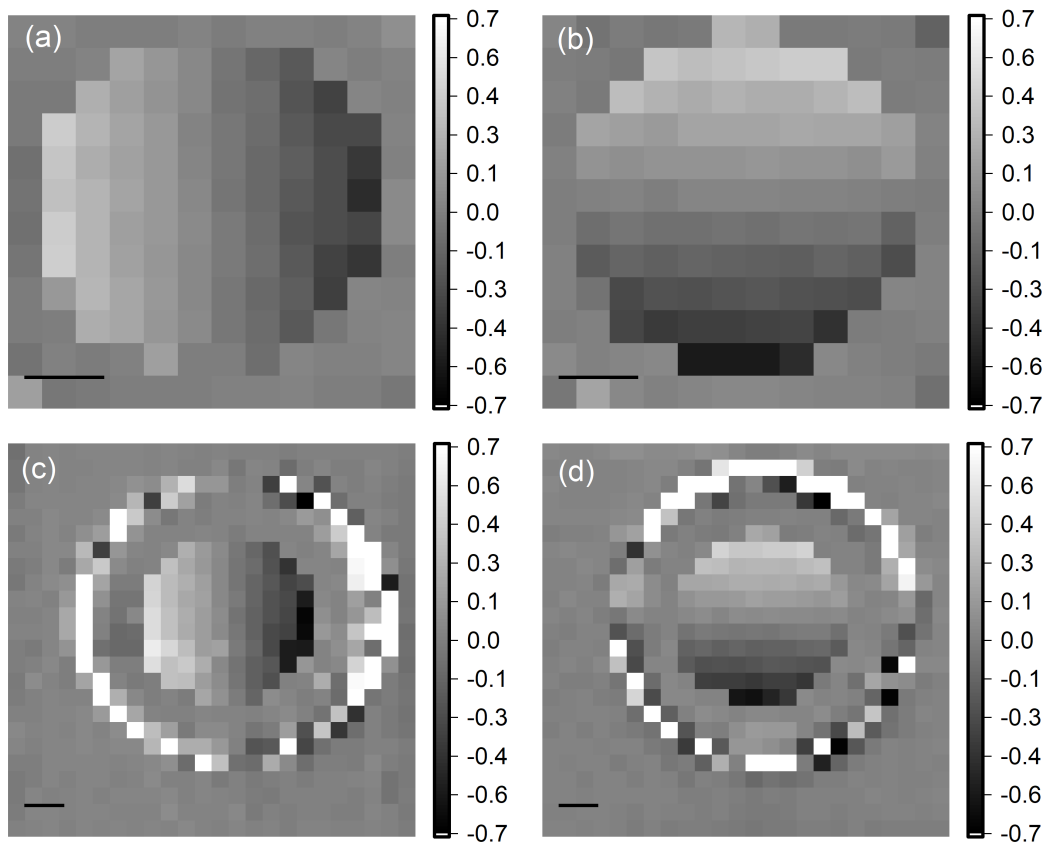


**Figure A.1:** Images of diamond lens in differential phase contrast acquired using SHSX v2.0 (a, b) and SHSX v2.1 (c, d) (scale bars are  $200 \mu\text{m}$ ). SHSX v2.1 has a wider field-of-view maintaining same spatial and, in case of the same experimental conditions, angular resolution. Differential phase data of the central part of the lens retrieved using SHSX v2.0 is in the good agreement with the data retrieved using SHSX v2.1 [Mikhaylov et al. 2020].

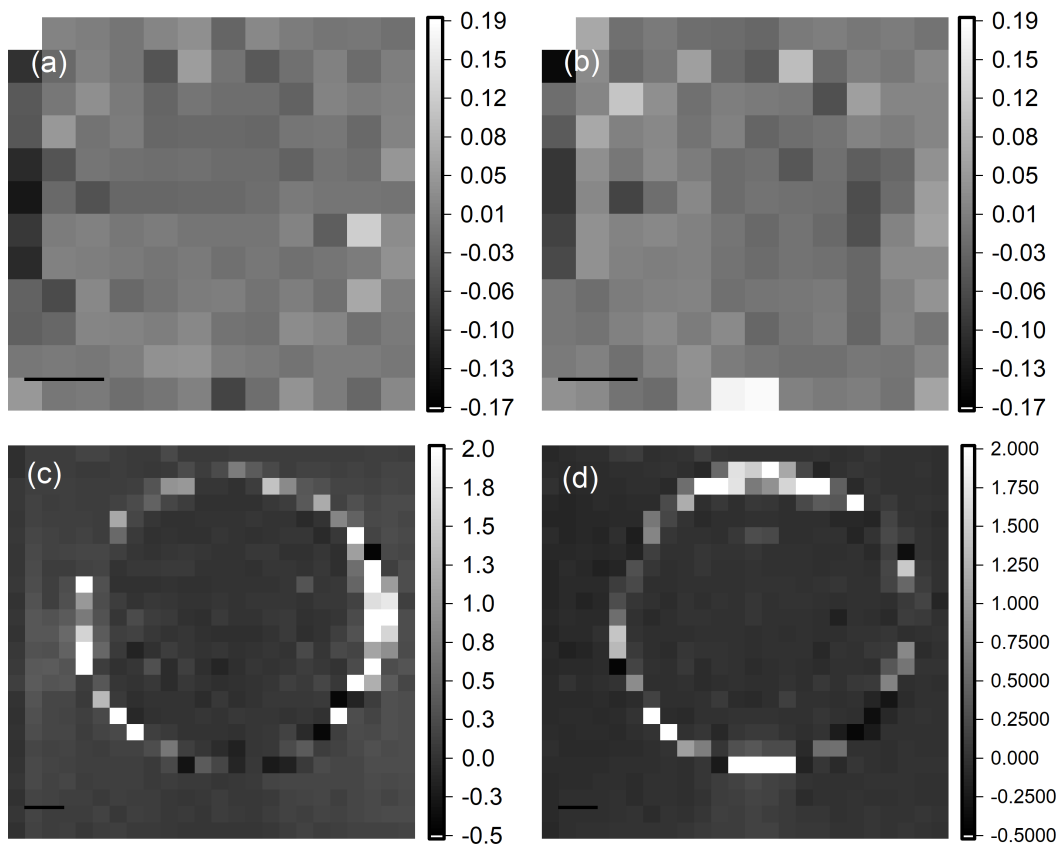


**Figure A.2:** Images of diamond lens in dark-field contrast acquired using SHSX v2.0 (a, b) and SHSX v2.1 (c, d) (scale bars are 200  $\mu\text{m}$ ). Scattering data acquired with the SHSX v2.0 does not show prominent contrast due to high quality of the manufactured lens as well as initial diamond monocrystal. Data acquired with the SHSX v2.1 show similar results in case of the central region. However, the appearance of the strong edge effect is visible [Mikhaylov et al. 2020].

## B Super-resolution scattering contrast imaging of the diamond lens

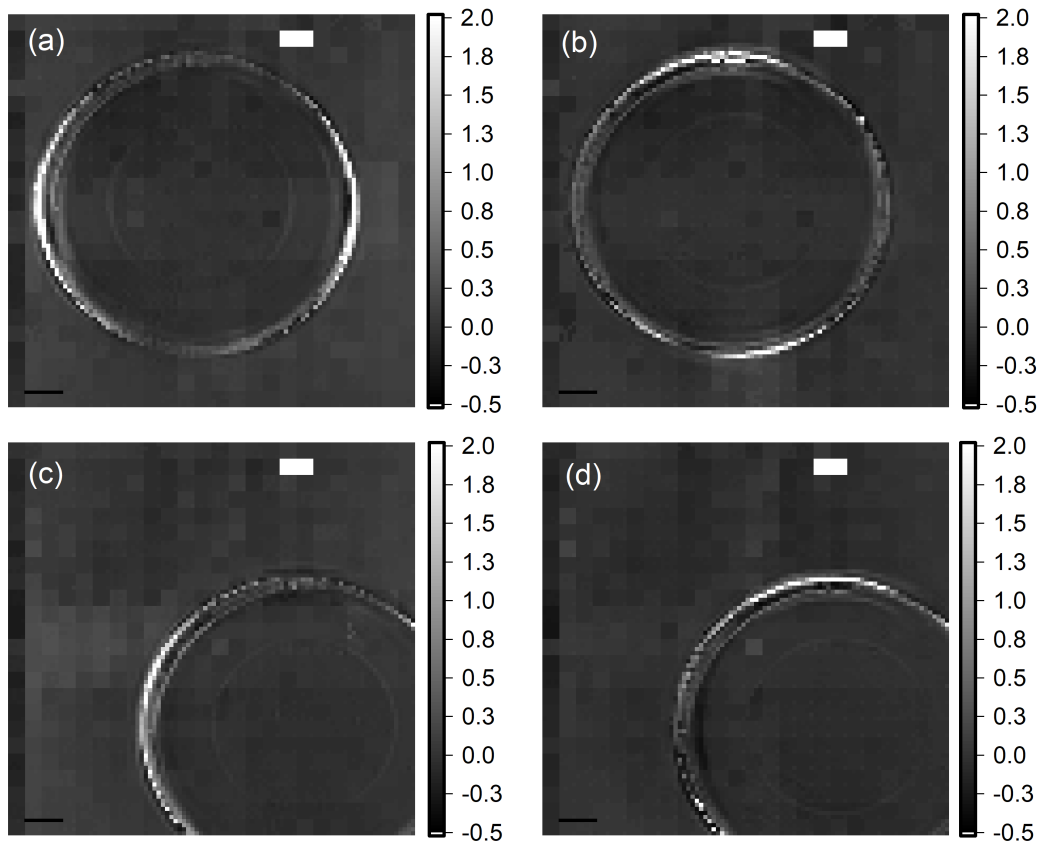


**Figure B.1:** Super-resolution images of diamond lens in scattering contrast acquired using SHSX v2.1 in LG (low gain) area (a, b) and HG (high gain) area (c, d) (scale bars are  $200\ \mu\text{m}$ ). Similarly to the figureA.2, a strong edge effect is visible on the rim of the lens. However, due to super-resolution approach and thus higher spatial resolution, it was possible to detect the edge of the inner concave region of the lens [Mikhaylov et al. 2020].



## C Shack-Hartmann patterns generation routine

```
1
2
3 """
4
5 Shack-Hartmann patterns generation routine.
6
7 Function descriptions:
8
9 image_derivatives(image) - generates gradients of the initial image to
10 simulate differential phase contrast;
11
12 gauss_single_flat(n) - generates single 2-dimensional Gaussian function
13 with the peak in the center position and sigmas equal to unity;
14
15 gauss_single_full(sigma_x,sigma_y,center_x,center_y,height,n,offset,order
16 =1) - generates single 2-dimensional Gaussian function with specified
17 parameters;
18
19 gauss_multiple_flat(n,N,noise=0) - generates array of the 2-dimensional
20 Gaussian functions, that acts as a flat filed image;
21
22 gauss_multiple_full(sigma_x,sigma_y,center_x,center_y,height,n,N, offset,
23 obsc_mask=None,noise=0) - generates array of the 2-dimensional
24 Gaussian functions with specified parameters according to transmission,
25 phase and scattering distribution of a given object.
26
27 Created by Mikhaylov Andrey.
28 Last update 12.04.2022.
29
30 andrey.mikhaylov.kit@gmail.com
31
32 """
33
34 __version__ = '1.8_12.04.2022'
35
36
37 import numpy as np
38 # import matplotlib.pyplot as plt
39 # from skimage.util import random_noise
40 from scipy.signal import unit_impulse
41
42 def image_derivatives(image):
```

```

36     """
37
38
39     Parameters
40     -----
41     image : ndarray of floats
42           your image, specifically absolute phase
43
44     Returns
45     -----
46     Dx : ndarray of floats
47         gradient in x direction\diff. phase in x direction.
48     Dy : ndarray of floats
49         gradient in y direction\diff. phase in y direction.
50
51     """
52
53     Dx = np.gradient(image, axis=1)
54     Dy = np.gradient(image, axis=0)
55     return Dx,Dy
56
57
58
59 def gauss_single_flat(n):
60     sigma_x = 1
61     sigma_y = 1
62     center_x = np.floor(n/2)
63     center_y = np.floor(n/2)
64     height = 1
65     order = 1
66     x,y = np.meshgrid(np.linspace(0,n-1,n),np.linspace(0,n-1,n))
67     gauss = np.ones((n,n))
68     for i in range(gauss.shape[0]):
69         for j in range(gauss.shape[1]):
70             gauss[i,j] = height*np.exp(-(
71                 ((center_x-x[i,j])**2/(2*sigma_x**2)) +
72                 ((center_y-y[i,j])**2/(2*sigma_y**2)) )**order )
73
74     # plt.imshow(gauss)
75     # plt.colorbar()
76     # plt.show()
77     return gauss
78
79
80
81
82 def gauss_single_full(sigma_x,sigma_y,center_x,center_y,height,n,offset,
83 order=1):
84     x,y = np.meshgrid(np.linspace(1,n,n),np.linspace(1,n,n))
85     gauss = np.ones((n,n))
86     center_x +=np.floor(n/2)
87     center_y +=np.floor(n/2)

```

```

88     for i in range(gauss.shape[0]):
89         for j in range(gauss.shape[1]):
90             gauss[i,j] = height*np.exp(-((center_x-x[i,j])**2/
91                 (2*sigma_x**2)) + ((center_y-y[i,j])**2/(2*sigma_y**2)) )
92                 **order ) + offset
93
94     # plt.imshow(gauss)
95     # plt.colorbar()
96     # plt.show()
97     return gauss
98
99 def gauss_multiple_flat(n,N,noise=0):
100     """
101     simulates ideal gaussian pattern.
102
103
104     Parameters
105     -----
106     n: int, preferably even to match FFT restrictions
107         amount of pixels per single unit cell(one gaussian)
108
109     N: int, preferably even to match FFT restrictions
110         amount of gaussians per side
111
112     noise: float
113         random noise in the values of mean image value
114
115
116     Returns
117     -----
118     array of size (N*n,N*n) with N*N gaussians, each sampled by n*n points
119
120     """
121     gauss_full_flat = np.tile(gauss_single_flat(n), (N, N))
122     if noise!=0:
123         gauss_full_flat = gauss_full_flat + np.mean(gauss_full_flat)*
124             noise*np.random.rand(N*n,N*n)
125     # plt.imshow(gauss_full)
126     # plt.colorbar()
127     # plt.show()
128     return gauss_full_flat
129
130
131 def gauss_multiple_full(sigma_x,sigma_y,center_x,center_y,height,n,N,
132 offset,obsc_mask=None,noise=0):
133     """
134     simulates gaussian pattern.
135
136     for ideal case:
137         sigma_x,sigma_y,center_x,center_y,height = arrays of ones,
138         offset = array of zeros, noise = 0.
139         Or just call gauss_multiple_flat

```

```

140
141
142 Parameters
143 -----
144
145 sigma_x,sigma_y: arrays of size N*N
146     gaussian broadening (used for scattering pseudo-simulation)
147
148 center_x,center_y: arrays of size N*N
149     position of the gaussian center within single unit cell (one
150     gaussian) (used for refraction pseudo-simulation)
151
152 height: array of size N*N
153     height of the gaussian (used for absorption pseudo-simulation)
154
155 offset: arrays of size N*N
156     offset of the gaussian, simulates constant background\flux
157
158 n: int, preferably even to match FFT restrictions
159     amount of pixels per single unit cell(one gaussian)
160
161 N: int, preferably even to match FFT restrictions
162     amount of gaussians per side
163
164 obsc_mask: array of size N*N
165     if wavefront has discontinuity, provide mask that covers this
166     region
167
168 noise: float
169     random noise in the values of mean image value
170
171 Returns
172 -----
173 array of size (N*n,N*n) with N*N gaussians, each sampled by n*n points
174
175 """
176
177 gauss_full = np.ones((N*n,N*n))
178 for n_x in range(N):
179     for n_y in range(N):
180         if obsc_mask !=None and obsc_mask[n_x,n_y] == 0:
181             gauss_full[n_x*n:n+n_x*n,n_y*n:n+n_y*n] =
182                 10*unit_impulse((n,n),idx='mid')
183         else:
184             g = gauss_single_full(sigma_x[n_x,n_y],sigma_y[n_x,n_y],
185                 center_x[n_x,n_y],center_y[n_x,n_y],height[n_x,n_y],n,
186                 offset[n_x,n_y],order=1)
187             gauss_full[n_x*n:n+n_x*n,n_y*n:n+n_y*n] = g
188 if noise!=0:
189     gauss_full = gauss_full +
190     np.mean(gauss_full)*noise*np.random.rand(N*n,N*n)

```

```

191     # plt.imshow(gauss_full)
192     # plt.colorbar()
193     # plt.show()
194     return gauss_full
195
196
197 if __name__ == "__main__":
198     import matplotlib.pyplot as plt
199     import numpy as np
200     from skimage.morphology import disk
201     from tifffile import imread, imsave
202     from scipy import constants as const
203     from skimage.transform import rotate
204     from skimage.transform import rescale
205     import os
206
207
208
209
210     n = 8
211     N = 150
212     pix_size = 6.25e-6 #
213     pitch = n*pix_size
214     FoV = pitch*N
215     E = 10007.5039 #energy in ev
216     lambd = const.h * const.c / (E*const.e)
217     beta = 3.70246567E-09
218     delta = 2.66748725E-06
219     mu = 4*const.pi * beta / lambd
220     diameter = 0.9875e-3
221     radius_in_pixels = int(diameter/(2*pix_size))
222     rot_angle = 25
223     save = True
224     path_to_save = r'D:\save'
225
226     print('Amount of lenses per side is {}. Pixel size is {} um. Pitch of
227     the SHSX is {} um. FoV is {} mm per side. Energy of X-rays is {} keV.
228     Material is PMMA. Diameter of the rod is approx. {} mm.'.format(N,
229     pix_size*1e6,pitch*1e6,FoV*1000,E/1000,1))
230
231
232     # creating flat gaussian pattern
233     g = gauss_multiple_flat(n,N)
234
235     plt.imshow(g)
236     plt.colorbar()
237     plt.title('flat pattern')
238     plt.show()
239
240     # creating slice of the 3D object, voxel size == pitch**3 and line
241     projection of the slice
242     slice_3d_object = np.pad(disk(radius_in_pixels),(520, 521), 'constant',

```

```
243     constant_values=(0, 0))
244     line_proj = np.sum(slice_3d_object,axis=0)
245
246     # stacking line projections to create 2d projection and translating
247     values to micrometers. rotation on rot_angle value
248
249     proj = rotate(np.tile(line_proj,(N*n,1)) * pix_size,rot_angle)
250
251
252
253     plt.imshow(proj)
254     plt.colorbar()
255     plt.title('thickness projection')
256     plt.show()
257
258
259     # based on the thickness calculating transmission (T = exp(-mu*d))
260     and phase (Phi = 2*Pi*Delta*d/lambda)
261     transmission = np.exp(-mu*proj)
262     phase = 2 * const.pi * proj * delta / lambda
263
264
265     plt.imshow(transmission)
266     plt.colorbar()
267     plt.title('transmission')
268     plt.show()
269
270     plt.imshow(phase)
271     plt.colorbar()
272     plt.title('phase')
273     plt.show()
274
275     # taking gradients to create differential phase contrasts
276     dpcx,dpcy = image_derivatives(phase)
277
278     # plt.imshow(dpcx)
279     # plt.colorbar()
280     # plt.title('dpcx')
281     # plt.show()
282
283     # plt.imshow(dpcy)
284     # plt.colorbar()
285     # plt.title('dpcy')
286     # plt.show()
287
288     # assuming object without scattering and attenating approx. 50%
289     # in the middle, creating corresponding gaussian pattern
290
291     sigma_x = np.ones((N,N))
292     sigma_y = np.ones((N,N))
293     offset = np.zeros((N,N))
294
```

```
295 height = np.copy(rescale(transmission,1/n))
296 center_x = rescale(dpcx,1/n)
297 center_y = rescale(dpcy,1/n)
298
299 plt.imshow(center_x)
300 plt.colorbar()
301 plt.title('center_x')
302 plt.show()
303
304 plt.imshow(center_y)
305 plt.colorbar()
306 plt.title('center_y')
307 plt.show()
308
309 g_obj = gauss_multiple_full(sigma_x,sigma_y,center_x,center_y,height,
310 n,N,offset)
311
312 plt.imshow(g_obj,vmin=0,vmax=1)
313 plt.colorbar()
314 plt.title('obj pattern')
315 plt.show()
316
317
318 if save:
319     print('Results will be saved to ' + path_to_save)
320     imsave(os.path.join(path_to_save,'transmission.tif'),
321 transmission.astype(np.float32))
322     imsave(os.path.join(path_to_save,'phase.tif'),
323 phase.astype(np.float32))
324     imsave(os.path.join(path_to_save,'proj.tif'),
325 proj.astype(np.float32))
326     imsave(os.path.join(path_to_save,'gauss_ref.tif'),
327 g.astype(np.float32))
328     imsave(os.path.join(path_to_save,'gauss_object.tif'),
329 g_obj.astype(np.float32))
330 else:
331     print('Results will not be saved')
```



## D Shack-Hartmann patterns generation routine with propagation to the lens focal plane

```
1     '''
2     Shack-Hartmann patterns generation routine with propagation to the lens
3     focal plane.
4     Function descriptions:
5
6     para_lens(r,shape,thickness,aperture) - generates parabolic lens
7     aperture_mask(r,shape) - generates aperture mask
8     prop(WF,lam,z,pixsize) - one of two functions to propagate wavefront in the
9     near field
10    free_nf(w, l, z, pixsize=1.) - second of two functions to propagate
11    wavefront in the near field
12
13    Created by Mikhaylov Andrey.
14    Last update 03.05.2023.
15
16    andrey.mikhaylov.kit@gmail.com
17
18    '''
19
20    import numpy as np
21    import matplotlib.pyplot as plt
22    import scipy.constants as const
23    from tiff file import imread,imsave
24    import scipy
25    from tqdm import trange
26    from scipy.optimize import curve_fit
27
28    def para_lens(r,shape,thickness,aperture):
29        '''
30
31        Parameters
32        -----
33        r : float
34            radius of lens apex.
35        shape : int
36            field shape.
37        thickness : float
38            thickness of a lens pedestal.
39        aperture : float
```

```

40     radius of aperture.
41
42     Returns
43     -----
44     z : array of floats
45         lens material thickness projection.
46
47     '''
48
49     sh = (shape, shape)
50     xx, yy = np.indices(sh)
51     xx = xx - int(shape/2)
52     yy = yy - int(shape/2)
53     z = (1/(2*r))*(xx**2+yy**2) + thickness
54     mask = np.ones((shape, shape))
55     mask[(xx)**2 + (yy)**2 >= aperture**2] = 0
56     z[(xx)**2 + (yy)**2 >= aperture**2] = np.max(z*mask)
57     # return z*mask
58     return z
59
60 def aperture_mask(r, shape):
61     '''
62
63
64     Parameters
65     -----
66     r : float
67         aperture radius.
68     shape : int
69         field shape.
70
71     Returns
72     -----
73     mask : array of ints
74         aperture mask as array of ints.
75
76     '''
77
78     sh = (shape, shape)
79     xx, yy = np.indices(sh)
80     xx = xx - int(shape/2)
81     yy = yy - int(shape/2)
82     mask = np.ones((shape, shape))
83     mask[(xx)**2 + (yy)**2 >= r**2] = 0
84     return mask
85
86
87 def prop(WF, lam, z, pixsize):
88     '''
89     propagates wavefront in the near field.
90
91     Parameters

```

```

92     -----
93     WF : array of complex numbers
94         incoming wavefront to propagate.
95     lam : float
96         wavelength.
97     z : float
98         distance to propagate.
99     pixsize : float
100         pixelsize.
101
102     Raises
103     -----
104     RuntimeError
105         raises if incoming wavefront is not square. in future it will be
106         padded automatically to become square.
107
108     Returns
109     -----
110     WF_out : array of complex numbers
111             propagated wavefront.
112
113     '''
114     sh = WF.shape
115     if sh[0] != sh[1]:
116         raise RuntimeError('X and Y dimensions are different, WF should be
117         square matrix')
118
119     WF_f = np.fft.fft2(WF)
120     kx = 2*np.pi * np.fft.fftfreq(sh[0], pixsize)
121     kxv, kyv = np.meshgrid(kx,kx)
122     k = 2*np.pi/lam
123     return np.fft.ifft2(WF_f*np.exp(1j*z*np.sqrt(k**2-kxv**2-kyv**2)))
124
125
126
127
128
129 def free_nf(w, l, z, pixsize=1.):
130     """\
131     Free-space propagation (near field) of the wavefield of a distance z.
132     l is the wavelength.
133
134     taken from https://github.com/pierrethibault/UMPA
135     """
136     # if w.ndim != 2:
137     #     raise RuntimeError("A 2-dimensional wave front 'w' was expected")
138
139     sh = w.shape
140
141     # Convert to pixel units.

```

```

142 z = z / pixsize
143 l = l / pixsize
144
145 # Evaluate if aliasing could be a problem
146 if min(sh)/np.sqrt(2.) < z*l:
147     print(f"Warning: z > N/(sqrt(2)*lamda) = %.6g: this calculation
could fail." % (min(sh)/(l*np.sqrt(2.))))
148     # print f"Warning: z > N/(sqrt(2)*lamda) = %.6g: this calculation
could fail." % (min(sh)/(l*np.sqrt(2.)))
149     # print "(consider padding your array, or try a far field method)"
150
151 q2 = np.sum((np.fft.ifftshift(np.indices(sh).astype(float) - np.reshape
(np.array(sh)//2,(len(sh),) + len(sh)*(1,)), range(1,len(sh)+1)) * np.
array([1./sh[0], 1./sh[1]]).reshape((2,1,1))**2, axis=0)
152
153 return np.fft.ifftn(np.fft.fftn(w) * np.exp(2j * np.pi * (z / l) * (np.
sqrt(1 - q2*l**2) - 1) ) )
154
155
156 r = 20
157 shape = 160
158 thikness = 2
159 aperture=40
160
161
162 N = 8
163 sh = (N*shape,N*shape)
164 E = 6622.12207
165 lam = const.h * const.c / (E * const.e)
166 delta = 6.10839379E-06
167 betta = 1.99929886E-08
168 delta_diam = 1.04523524E-05
169 betta_diam = 2.5941171E-08
170 z = 1.63 # propagation distance
171 psize = 1e-6 # pixel size
172 f_teor = r*1e-6/(2*delta)
173
174 lens_para_profile = para_lens(r,shape,thikness,aperture)
175
176 plt.imshow(lens_para_profile)
177 plt.title('lens_para_profile')
178 plt.colorbar()
179 plt.show()
180
181 # lens_para = aperture_mask(aperture,shape)*np.exp(-2j*np.pi*(delta-1j*
betta)*(1e-6)*(lens_para_profile)/lam)
182 lens_para = np.exp(-2j*np.pi*(delta-1j*betta)*(1e-6)*(lens_para_profile)/
lam)
183
184 plt.imshow(np.abs(np.abs(lens_para)), cmap='Greys_r')
185 plt.title('lens_para')
186 plt.colorbar()

```

```

187 plt.show()
188
189 pattern_parabolic = np.tile(lens_para, (N,N))
190
191
192 plt.imshow(np.abs(pattern_parabolic), cmap='Greys_r')
193 plt.title('pattern_parabolic')
194 plt.colorbar()
195 plt.show()
196
197
198 proped_para_pattern = np.abs(free_nf(pattern_parabolic, lam,
    2.8824239343979974, psize))**2
199
200 plt.imshow(proped_para_pattern, cmap='Greys_r')
201 plt.title('proped_para_pattern')
202 plt.colorbar()
203 plt.show()
204
205
206 diam_lens_profile = para_lens(200,1280,thickness,450)
207 diam_lens_OPD = diam_lens_profile*delta_diam
208 print(f'maximal OPD of DL is {np.max(diam_lens_OPD)}')
209 print(f'minimal OPD of DL is {np.min(diam_lens_OPD)}')
210
211
212 plt.imshow(diam_lens_OPD)
213 plt.title('diam_lens_OPD')
214 plt.colorbar()
215 plt.show()
216
217
218 # diam_lens = aperture_mask(450,1280)*np.exp(-2j*np.pi*(delta_diam-1j*
    betta_diam)*(1e-6)*(diam_lens_profile)/lam)
219 diam_lens = np.exp(-2j*np.pi*(delta_diam-1j*betta_diam)*(1e-6)*
    (diam_lens_profile)/lam)
220
221
222 plt.imshow(np.abs(diam_lens), cmap='Greys_r')
223 plt.title('diam_lens')
224 plt.colorbar()
225 plt.show()
226
227
228 proped = np.abs(free_nf(diam_lens*pattern_parabolic, lam,
    2.8824239343979974, psize))**2
229
230 plt.imshow(proped, cmap='Greys_r')
231 plt.title('diam_lens')
232 plt.colorbar()
233 plt.show()

```



## List of Figures

2.1	Basic Hartmann wavefront sensor principle. Two images are required to extract information on the wavefront: a reference image of the projected pattern (co-called flat-field) and a distorted pattern. Measured shifts of the spots are proportional to the first derivative of the phase. . . . .	10
2.2	Illustration of the presence of absorptive, refractive, scattering, and mixed media on shape and location parameters of the single beamlet. . . . .	11
2.3	Simulated Shack-Hartmann patterns for flat wave (reference pattern) and aberrated wave (final pattern). . . . .	11
2.4	Dark-Field (Scattering) Extinction Coefficient calculated according to [Lynch et al. 2011] for $E=15$ keV, $L = 15$ cm, $P = 100 \mu\text{m}$ and diameters of spheres 10-1500 nm. . .	15
2.5	Interleaving super-resolution approach. Colors red, yellow, magenta, and light blue represent the sequential image acquisitions. . . . .	16
2.6	Example of mask projection and the absolute value of its Fourier transform. Experimental data were acquired in cone beam configuration with $10 \mu\text{m}$ period mask, $\approx 140\times$ magnification and detector Perkin Elmer XRD 1621. . . . .	17
2.7	Fourier Central Slice Theorem states the equality between one-dimensional Fourier transforms of the object projection and the slice through the origin of two-dimensional Fourier transform of the same object parallel to the projection line. . .	19
2.8	Backprojection (BP) vs. Filtered Backprojection (FBP): a) - ground truth of the object, b) - BP, c) - FBP with ramp filtration. . . . .	20
2.9	Ramp filtration effect on sinograms: a) - initial sinogram, b) - ramp filtered sinogram. .	21
3.1	Evolution of SHSX designs. SHSX v1.0 (a) with circular cylindrical holes of diameter $40 \mu\text{m}$ and field-of-view $1 \times 1$ mm. SHSX v2.0 (b) with parabolic cylindrical holes with apex of parabolas $20 \mu\text{m}$ and field-of-view $1 \times 1$ mm, SHSX v2.1 (c) with similar parameters to v2.0 but different printings strategy leading to increase of field-of-view to $2 \times 2$ mm (scale bars are 0.5 mm) [Mikhaylov et al. 2020]. .	26
3.2	Dependence of average gain values for different generations of SHSX on scanning distance [Mikhaylov et al. 2020]. . . . .	27
3.3	Scanning electron microscopy of the produced array: a) - overview image (distortion is due to low voltage mode and large working distance); b) - closeup of the edge showing tiled blocks and cylindrical holes; c) - closeup revealing misalignment of the stitching; d) - closeup showing roughness of the surface. . . . .	29
3.4	Dependence of average spot width in x (a) and y (b) directions for different generations of SHSX on scanning distance [Mikhaylov et al. 2020]. . . . .	30
3.5	Dependence of average visibility for different generations of SHSX on scanning distance [Mikhaylov et al. 2020]. . . . .	30

3.6	Gain maps of different generations of SHSX at focal distances: SHSX v.1.0 (a) at 29.7 cm; SHSX v.2.0 (b) at 37.7 cm; SHSX v.2.1 (c) at 40.7 cm [Mikhaylov et al. 2020].	31
3.7	Visibility maps of different generations of SHSX at specific focal distances: SHSX v.1.0 (a) at 29.7 cm; SHSX v.2.0 (b) at 37.7 cm; SHSX v.2.1 (c) at 40.7 cm [Mikhaylov et al. 2020]. . . . .	32
3.8	White beam spectra at the TOPO-TOMO beamline, KARA synchrotron facility. The maximum intensity energy is 5.1 keV [Mikhaylov et al. 2020]. . . . .	32
3.9	Images of the SHSX v.2.1 spot pattern in white beam at the beginning (a) and after 15 hours exposure (b) (scale bars are 200 $\mu\text{m}$ ) [Mikhaylov et al. 2020]. . . . .	33
3.10	Evolution of the projected pattern pitch of SHSX v.2.1 after 15 hours in the white beam. The bottom side of the lens array, which was attached to the glass substrate, shows different shrinkage trend. Although average spot pitch is decreasing similarly to the other sides, absolute values a lower and abrupt step-like changes are visible [Mikhaylov et al. 2020]. . . . .	33
3.11	SEM images of the break site of SHSX v2.1 showing parabolic cylinders in vertical and horizontal directions. (scale bars are 100 $\mu\text{m}$ ) [Mikhaylov et al. 2020]. . . . .	34
3.12	Influxes of unclear nature on the surface of SHSX v.2.1 after 15 hours exposure, which might stems from unreacted chemicals (scale bars are 50 $\mu\text{m}$ ) [Mikhaylov et al. 2020]. . . . .	34
3.13	Images of a diamond lens in absorption contrast acquired using SHSX v2.0 (a) and SHSX v2.1 (b) (scale bars are 200 $\mu\text{m}$ ) [Mikhaylov et al. 2020]. . . . .	35
4.1	Scanning electron microscopy images of the lithography mask produced with electron beam lithography: 5 $\mu\text{m}$ period (a), 8 $\mu\text{m}$ period (b), and 10 $\mu\text{m}$ period (c). The scale bar is the same for (a), (b), and (c) [Mikhaylov et al. 2022]. . . . .	38
4.2	Deep X-ray lithography schematic sequence for the inverted Hartmann mask manufacturing. The X-ray lithography process was carried out at the LIGA 1 beamline (KARA synchrotron facility, Karlsruhe, Germany) [Mikhaylov et al. 2022]. . . . .	38
4.3	Experimental laboratory setup with mask-before-sample geometry. X-rays are emitted from the X-ray tube with focal spot size $s$ . The inverted Hartmann mask with period $P$ is located at the distance $D_1$ from the source. The detector with physical pixel size $PS$ records the overlapped iHM-object image. Gray divergent lines highlight the penumbral blur (see equation 2.62) introduced by the extended source [Mikhaylov et al. 2022]. . . . .	39
4.4	Scanning electron microscopy images of the inverted Hartmann masks produced with Deep X-ray lithography: 5 $\mu\text{m}$ period (a), 8 $\mu\text{m}$ period (b), 10 $\mu\text{m}$ period (c), isometric view of 10 $\mu\text{m}$ period mask (d). The scale bar for images (a) and (b) is shown in the image (c) [Mikhaylov et al. 2022]. . . . .	41
4.5	Inverted Hartmann mask raw projection with a close-up (a) and visibility map (b). The black horizontal stripe visible in the upper right corner of the image (a) is a line defect of defect pixels. The cross-like pattern in the visibility map (b) is caused by pillar shadowing due to the short distance between the mask and the cone-beam source [Mikhaylov et al. 2022]. . . . .	41

4.6	Phantom manufacturing process. The structures (photoresist meshes and pillars) of different sizes (5-100 $\mu\text{m}$ ) were made by UV lithography on a smooth silicon wafer, as shown in the lower left corner. Meshes and pillars are outlined in red and blue, respectively. The microstructures were lifted off the wafers and collected in a small vial (Eppendorf tube shown in the lower right corner). On top, the optical microscopy and SEM images of the structures are shown, indicating the variability of structure sizes [Mikhaylov et al. 2022]. . . . .	42
4.7	Imaging of the phantom sample: (a) - raw projection, (b) - absorption, (c) - phase map, (d) - sum of scattering signal, (e,f) - scattering in vertical and horizontal directions. The black arrow indicates the location of the micropillars, and the white arrow the location of the micromeshes [Mikhaylov et al. 2022]. . . . .	43
4.8	(a) - absorption contrast; (d,g) - differential phase contrast in horizontal and vertical directions; (b,e,h) - profiles for the mesh locations outlined with red lines; (c,f,i) - profiles for the micropillars locations outlined with blue lines. The SNR value is introduced to compare the signals according to Eq. 4.2 [Mikhaylov et al. 2022].	44
4.9	Preparation of the composite specimens through lamination technique in a vacuum bag [Mikhaylov et al. 2022]. . . . .	45
5.1	Experimental setup for super-resolution multi-contrast X-ray imaging with lens array-before-sample geometry. X-rays are emitted by the synchrotron. The Shack-Hartmann sensor with a period of 85 $\mu\text{m}$ is located at a distance of 107 cm from the detector. The diamond lens is located at a distance of 16 cm from the detector.	50
5.2	Super-resolution images of the diamond lens in absorption contrast acquired using SHSX v2.1: LG area (a) and HG area (b) of the SHXS v.2.1 (scale bars are 200 $\mu\text{m}$ ) [Mikhaylov et al. 2020]. . . . .	50
5.3	Super-resolution images of diamond lens in differential phase contrast acquired using SHSX v2.1: LG area (a) and HG area (b) of the SHXS v.2.1 (scale bars are 200 $\mu\text{m}$ ) [Mikhaylov et al. 2020]. . . . .	51
5.4	Comparison of normalized differential phase and absorption signals along shown lines for SHSX v2.1. in HG area [Mikhaylov et al. 2020]. . . . .	51
5.5	Multi-contrast X-ray imaging of the reference samples (a,b,e,f) and reference samples after DMA (c,d,g,h). The figures show absorption contrast (a,c); differential phase in vertical direction (b,d); scattering (e,g); differential phase in horizontal direction (f,h). . . . .	52
5.6	Multi-contrast X-ray imaging of the samples embedded with microcapsules (a,b,e,f) and sample embedded with microcapsules after DMA (c,d,g,h). The figures show absorption contrast (a,c); differential phase vertical direction (b,d); scattering (e,g); differential phase horizontal direction (f,h). . . . .	53
5.7	Experimental laboratory setup for single-shot multi-contrast X-ray imaging and multi-contrast X-ray tomography. The inverted Hartmann mask is located at the distance $D_1$ , the sample at the distance $D_2$ , and detector at the distance $D_3$ from the X-ray source. . . . .	55

- 
- 5.8 Multi-contrast single-shot X-ray imaging of a polymer composite. Images in absorption (a,b,c), bidirectional scattering (d,e,f) and bidirectional phase (g,h,i) contrasts at angles 0, 90, 173.52 degrees as I, II, and III, respectively. Bright white areas on the images (a,b,c) represent glass fiber bundles that have higher absorption. Same areas in the phase and scattering contrasts reveal media with higher refraction and scattering signals. Presence of a line of defect pixels might be noticed on the upper right side of each image. The scale bar is shown in image (g). . . . . 56
- 5.9 Differential phase (a,b,c) and scattering signal (d,e,f) in vertical direction at angles 162.25, 168.39 and 175.08 degrees as I, II and III, respectively. One could notice segmented signal of the glass fiber bundles, oriented under a small range of angles in respect to the X-ray propagation axis. Scale bar is shown in image (d). . . . . 57
- 5.10 Absorption (a,b,c) and scattering (d,e,f) tomography slices. Upper left marks represent slicing planes: xy - transverse plane, xz - coronal plane, zy - sagittal plane. The white arrows that signalize the intersection of slicing planes point to the air-containing defect with approx. a radius of 450  $\mu\text{m}$  that were invisible in the projections. The yellow arrows indicate the borders of the different density medias. Scale bar is shown in image (d). . . . . 58
- 5.11 Absorption (a,b,c) and scattering (d,e,f) tomography slices. Upper left marks represent slicing direction: xy - transverse plane, xz - coronal plane, zy - sagittal plane. The white arrows signalize the intersection of slicing planes. A thin layer of the scattering media is indicated with the red arrow. The yellow arrows point to the border of the pure resin-rich region. Scale bar is shown in image (d). . . . . 59
- 5.12 Absorption (a,b,c) and scattering (d,e,f) tomography slices. Upper left marks represent slicing direction: xy - transverse plane, xz - coronal plane, zy - sagittal plane. White arrows signalize the intersection of slicing planes. Clear presence of the air-containing defect with approx. a radius of 495  $\mu\text{m}$  that were invisible in the projections. Yellow arrow indicate thin layer of glass fibers contributing to scattering signal. Scale bar is shown in image (d). . . . . 59
- 5.13 Segmentation of the glass fiber bundles based on absorption tomography data: (a) volume-of-interest; (b,c,d) are transverse, coronal, and sagittal planes, respectively, with the marked region of interest. . . . . 60
- A.1 Images of diamond lens in differential phase contrast acquired using SHSX v2.0 (a, b) and SHSX v2.1 (c, d) (scale bars are 200  $\mu\text{m}$ ). SHSX v2.1 has a wider field-of-view maintaining same spatial and, in case of the same experimental conditions, angular resolution. Differential phase data of the central part of the lens retrieved using SHSX v2.0 is in the good agreement with the data retrieved using SHSX v2.1 [**Mikhaylov** et al. 2020]. . . . . 67
- A.2 Images of diamond lens in dark-field contrast acquired using SHSX v2.0 (a, b) and SHSX v2.1 (c, d) (scale bars are 200  $\mu\text{m}$ ). Scattering data acquired with the SHSX v2.0 does not show prominent contrast due to high quality of the manufactured lens as well as initial diamond monocrystal. Data acquired with the SHSX v2.1 show similar results in case of the central region. However, the appearance of the strong edge effect is visible [**Mikhaylov** et al. 2020]. . . . . 68

- 
- B.1 Supper-resolution images of diamond lens in scattering contrast acquired using SHSX v2.1 in LG (low gain) area (a, b) and HG (high gain) area (c, d) (scale bars are  $200\ \mu\text{m}$ ). Similarly to the figureA.2, a strong edge effect is visible on the rim of the lens. However, due to supper-resolution approach and thus higher spatial resolution, it was possible to detect the edge of the inner concave region of the lens [Mikhaylov et al. 2020]. . . . . 69



## List of Tables

3.1	The minimal average width of focal spots at given distances and the astigmatism parameter $\Delta$ [Mikhaylov et al. 2020]. . . . .	30
5.1	Mean absorption and scattering value in arbitrary unit for the reference composite (RC) and self-healing composite (SHC) samples, before and after dynamic mechanical analysis (DMA). . . . .	53



## Peer-reviewed publications

**Andrey Mikhaylov**, Margarita Zakharova, Vitor Vlnieska, Jorge Luis Beltran Diaz, Daniel Münch, Sergio Henrique Pezzin, and Danays Kunka. Single-shot multi-contrast x-ray imaging and tomography of polymer composites with inverted hartmann mask and laboratory source. *Journal of Imaging*, under review, 2023.

Margarita Zakharova, **Andrey Mikhaylov**, Stefan Reich, Anton Plech, and Danays Kunka. Bulk morphology of porous materials at submicrometer scale studied by dark-field x-ray imaging with hartmann masks. *Phys. Rev. B*, 106:144204, Oct 2022. doi: 10.1103/PhysRevB.106.144204. URL <https://link.aps.org/doi/10.1103/PhysRevB.106.144204>.

**Andrey Mikhaylov**, Margarita Zakharova, Vitor Vlnieska, Ankita Khanda, Sabine Bremer, Marcus Zuber, Sergio Henrique Pezzin, and Danays Kunka. Inverted hartmann mask made by deep x-ray lithography for single-shot multi-contrast x-ray imaging with laboratory setup. *Optics Express*, 30(6):8494–8509, 2022.

**Andrey Mikhaylov**, Stefan Reich, Margarita Zakharova, Vitor Vlnieska, Roman Laptev, Anton Plech, and Danays Kunka. Shack–hartmann wavefront sensors based on 2d refractive lens arrays and super-resolution multi-contrast x-ray imaging. *Journal of synchrotron radiation*, 27(3): 788–795, 2020.

Sara Ferreira Da Costa, Marcus Zuber, Margarita Zakharova, **Andrey Mikhaylov**, Tilo Baumbach, Danays Kunka, and Sergio Henrique Pezzin. Self-healing triggering mechanism in epoxy-based material containing microencapsulated amino-polysiloxane. *Nano Select*, 3(3):577–593, 2022.

Margarita Zakharova, **Andrey Mikhaylov**, Vitor Vlnieska, and Danays Kunka. Single-shot multi-contrast x-ray imaging for in situ visualization of chemical reaction products. *Journal of Imaging*, 7(11):221, 2021.

Vitor Vlnieska, Margarita Zakharova, **Andrey Mikhaylov**, and Danays Kunka. Lithographic performance of aryl epoxy thermoset resins as negative tone photoresist for microlithography. *Polymers*, 12(10):2359, 2020.

Vitor Vlnieska, **Andrey Mikhaylov**, Margarita Zakharova, Eva Blasco, and Danays Kunka. Epoxy resins for negative tone photoresists. *Polymers*, 11(9):1457, 2019.

Margarita Zakharova, Stefan Reich, **Andrey Mikhaylov**, Vitor Vlnieska, Tomy dos Santos Rolo, Anton Plech, and Danays Kunka. Inverted hartmann mask for single-shot phase-contrast x-ray imaging of dynamic processes. *Optics letters*, 44(9):2306–2309, 2019b.

**Andrey A Mikhaylov**, Stefan Reich, Anton Plech, Margarita Zakharova, Vitor Vlnieska, and Danays Kunka. 2d lens array for multi-contrast x-ray imaging. In *EUV and X-ray Optics: Synergy between Laboratory and Space VI*, volume 11032, page 1103208. International Society for Optics and Photonics, 2019.

M Zakharova, S Reich, **A Mikhaylov**, V Vlnieska, Marcus Zuber, Sabine Engelhardt, T Baumbach, and D Kunka. A comparison of customized hartmann and newly introduced inverted hartmann masks for single-shot phase-contrast x-ray imaging. In *EUV and X-ray Optics: Synergy between Laboratory and Space VI*, volume 11032, page 110320U. International Society for Optics and Photonics, 2019a.

## Bibliography

- Jens Als-Nielsen and Des McMorrow. *Elements of modern X-ray physics*. John Wiley & Sons, Chichester, United Kingdom, 2011.
- D ASTM. 2344 standard test method for short-beam strength of polymer matrix composite materials and their laminates. *ASTM: West Conshohocken, PA, USA*, 2016.
- Alberto Astolfo, Marco Endrizzi, Fabio A Vittoria, Paul C Diemoz, Benjamin Price, Ian Haig, and Alessandro Olivo. Large field of view, fast and low dose multimodal phase-contrast imaging at high x-ray energy. *Scientific reports*, 7(1):1–8, 2017. doi: 10.1038/s41598-017-02412-w.
- EW Backer, W Ehrfeld, D Münchmeyer, H Betz, A Heuberger, S Pongratz, W Glashauser, HJ Michel, and R v Siemens. Production of separation-nozzle systems for uranium enrichment by a combination of x-ray lithography and galvanoplastics. *Naturwissenschaften*, 69(11):520–523, 1982. doi: 10.1007/BF00463495.
- Alexander Barannikov, Maxim Polikarpov, Petr Ershov, Vladimir Bessonov, Ksenia Abrashitova, Irina Snigireva, Vyacheslav Yunkin, Gleb Bourenkov, Thomas Schneider, Andrey A Fedyanin, et al. Optical performance and radiation stability of polymer x-ray refractive nano-lenses. *Journal of synchrotron radiation*, 26(3):714–719, 2019.
- Martin Bech, O Bunk, T Donath, R Feidenhans, C David, and F Pfeiffer. Quantitative x-ray dark-field computed tomography. *Physics in Medicine & Biology*, 55(18):5529, 2010.
- Eric E Bennett, Rael Kopace, Ashley F Stein, and Han Wen. A grating-based single-shot x-ray phase contrast and diffraction method for in vivo imaging. *Medical physics*, 37(11):6047–6054, 2010. doi: 10.1118/1.3501311.
- Sebastien Berujon, Hongchang Wang, and Kawal Sawhney. X-ray multimodal imaging using a random-phase object. *Physical Review A*, 86(6):063813, 2012. doi: 10.1103/PhysRevA.86.063813.
- Pidassa M Bidola, Irene Zanette, Klaus Achterhold, Christian Holzner, and Franz Pfeiffer. Optimization of propagation-based phase-contrast imaging at a laboratory setup. *Optics express*, 23(23):30000–30013, 2015.
- Pierre Bon, Serge Monneret, and Benoit Wattellier. Noniterative boundary-artifact-free wavefront reconstruction from its derivatives. *Applied optics*, 51(23):5698–5704, 2012.
- U Bonse and M Hart. An x-ray interferometer. *Applied Physics Letters*, 6(8):155–156, 1965.

- Yujia Chen, Weimin Zhou, Charlotte K Hagen, Alessandro Olivo, and Mark A Anastasio. Comparison of data-acquisition designs for single-shot edge-illumination x-ray phase-contrast tomography. *Optics express*, 28(1):1–19, 2020. doi: 10.1364/OE.28.000001.
- Corrine Ying Xuan Chua, Hsuan-Chen Liu, Nicola Di Trani, Antonia Susnjar, Jeremy Ho, Giovanni Scorrano, Jessica Rhudy, Antons Sizovs, Graziano Lolli, Nathanael Hernandez, et al. Carbon fiber reinforced polymers for implantable medical devices. *Biomaterials*, 271:120719, 2021.
- Michael W Czabaj, Mark L Riccio, and William W Whitacre. Numerical reconstruction of graphite/epoxy composite microstructure based on sub-micron resolution x-ray computed tomography. *Composites Science and Technology*, 105:174–182, 2014.
- Christian David, B Nöhammer, H\_H Solak, and E Ziegler. Differential x-ray phase contrast imaging using a shearing interferometer. *Applied physics letters*, 81(17):3287–3289, 2002.
- TJ Davis, D Gao, TE Gureyev, AW Stevenson, and SW Wilkins. Phase-contrast imaging of weakly absorbing materials using hard x-rays. *Nature*, 373(6515):595–598, 1995.
- Bruce H Dean, David L Aronstein, J Scott Smith, Ron Shiri, and D Scott Acton. Phase retrieval algorithm for jwst flight and testbed telescope. In *Space telescopes and instrumentation I: optical, infrared, and millimeter*, volume 6265, pages 314–330. SPIE, 2006.
- Yukun Deng, Xuechen Liang, Xiaopeng Pei, Kankan Zhai, Chao Wang, Baichao Zhang, Yungang Bai, Yanming Zhang, Pixin Wang, Ying Tan, et al. Self-healing ability and application of impact hardening polymers. *Polymer Testing*, 76:43–53, 2019.
- Frederik Desplentere, Stepan V Lomov, DL Woerdeman, Ignaas Verpoest, Martine Wevers, and A Bogdanovich. Micro-ct characterization of variability in 3d textile architecture. *Composites Science and Technology*, 65(13):1920–1930, 2005.
- Tomy dos Santos Rolo, Stefan Reich, Dmitry Karpov, Sergey Gasilov, Danays Kunka, Edwin Fohtung, Tilo Baumbach, and Anton Plech. A shack-hartmann sensor for single-shot multi-contrast imaging with hard x-rays. *Applied Sciences*, 8(5):737, 2018.
- Erik Schou Dreier, C Silvestre, J Kehres, D Turecek, M Khalil, JH Hemmingsen, O Hansen, J Jakubek, R Feidenhans, and UL Olsen. Virtual subpixel approach for single-mask phase-contrast imaging using timepix3. *Journal of Instrumentation*, 14(01):C01011, 2019. doi: 10.1088/1748-0221/14/01/C01011.
- Monica J Emerson, Kristine M Jespersen, Anders B Dahl, Knut Conradsen, and Lars P Mikkelsen. Individual fibre segmentation from 3d x-ray computed tomography for characterising the fibre orientation in unidirectional composite materials. *Composites Part A: Applied Science and Manufacturing*, 97:83–92, 2017.
- Michaela Esposito, Lorenzo Massimi, Ian Buchanan, Joseph D. Ferrara, Marco Endrizzi, and Alessandro Olivo. The transition from refraction to ultra-small-angle x-ray scattering (usaxs) in a laboratory phase-based x-ray microscope for soft tissue imaging. In *15th International Conference on X-ray Microscopy (XRM2022)*, 2022.

- Abrar Faisal, Thomas Beckenbach, Jürgen Mohr, and Pascal Meyer. Influence of secondary effects in the fabrication of submicron resist structures using deep x-ray lithography. *Journal of Micro/Nanolithography, MEMS, and MOEMS*, 18(2):023502, 2019. doi: 10.1117/1.JMM.18.2.023502.
- Andriy Fedorov, Reinhard Beichel, Jayashree Kalpathy-Cramer, Julien Finet, Jean-Christophe Fillion-Robin, Sonia Pujol, Christian Bauer, Dominique Jennings, Fiona Fennessy, Milan Sonka, et al. 3d slicer as an image computing platform for the quantitative imaging network. *Magnetic resonance imaging*, 30(9):1323–1341, 2012.
- Lee A Feldkamp, Lloyd C Davis, and James W Kress. Practical cone-beam algorithm. *Josa a*, 1(6):612–619, 1984.
- Jiemin Feng and Zhansheng Guo. Temperature-frequency-dependent mechanical properties model of epoxy resin and its composites. *Composites Part B: Engineering*, 85:161–169, 2016.
- SC Garcea, Ying Wang, and PJ Withers. X-ray computed tomography of polymer composites. *Composites Science and Technology*, 156:305–319, 2018.
- S Gasilov, A Mittone, T dos Santos Rolo, S Polyakov, S Zholudev, S Terentyev, V Blank, A Bravin, and T Baumbach. Refraction and ultra-small-angle scattering of x-rays in a single-crystal diamond compound refractive lens. *Journal of synchrotron radiation*, 24(6):1137–1145, 2017.
- Habibah Ghazali, Lin Ye, and Amie N Amir. Microencapsulated healing agents for an elevated-temperature cured epoxy: Influence of viscosity on healing efficiency. *Polymers and Polymer Composites*, 29(9\_suppl):S1317–S1327, 2021.
- Jonathan Glinz, Jan Šleichrt, Daniel Kytýř, Santhosh Ayalur-Karunakaran, Simon Zabler, Johann Kastner, and Sascha Senck. Phase-contrast and dark-field imaging for the inspection of resin-rich areas and fiber orientation in non-crimp vacuum infusion carbon-fiber-reinforced polymers. *Journal of Materials Science*, 56(16):9712–9727, 2021. doi: 10.1007/s10853-021-05907-0.
- Regine Gradl, Martin Dierolf, Lorenz Hehn, Benedikt Günther, Ali Önder Yildirim, Bernhard Gleich, Klaus Achterhold, Franz Pfeiffer, and Kaye Susannah Morgan. Propagation-based phase-contrast x-ray imaging at a compact light source. *Scientific reports*, 7(1):1–9, 2017.
- Walan Grizolli, Xianbo Shi, Lahsen Assoufid, and Leslie G Butler. Wavepy-python package for x-ray grating interferometry with applications in imaging and wavefront characterization. In *AIP Conference Proceedings*, volume 2054, page 060017. AIP Publishing LLC, 2019. doi: 10.1063/1.5084648.
- Lukas B. Gromann, Fabio De Marco, Konstantin Willer, Peter B. Noël, Kai Scherer, Bernhard Renger, Bernhard Gleich, Klaus Achterhold, Alexander A. Fingerle, Daniela Muenzel, Sigrid Auweter, Katharina Hellbach, Maximilian Reiser, Andrea Baehr, Michaela Dmochewitz, Tobias J. Schroeter, Frieder J. Koch, Pascal Meyer, Danays Kunka, Juergen Mohr, Andre Yaroshenko, Hanns-Ingo Maack, Thomas Pralow, Hendrik van der Heijden, Roland Proksa, Thomas Koehler, Nataly Wieberneit, Karsten Rindt, Ernst J. Rummeny, Franz Pfeiffer, and Julia

- Herzen. In-vivo x-ray dark-field chest radiography of a pig. *Scientific reports*, 7(1):1–7, 2017. doi: 10.1038/s41598-017-05101-w.
- H Guckel. High-aspect-ratio micromachining via deep x-ray lithography. *Proceedings of the IEEE*, 86(8):1586–1593, 1998. doi: 10.1109/5.704264.
- Alex Gustschin, Mirko Riedel, Kirsten Taphorn, Christian Petrich, Wolfgang Gottwald, Wolfgang Noichl, Madleen Busse, Sheila E Francis, Felix Beckmann, Jörg U Hammel, Julian Moosmann, Pierre Thibault, and Julia Herzen. High-resolution and sensitivity bi-directional x-ray phase contrast imaging using 2d talbot array illuminators. *Optica*, 8(12):1588–1595, 2021. doi: 10.1364/OPTICA.441004.
- J Hartmann. Bermerkungen über den bau und die justierung von spektrographen. *Zeitschrift für Instrumentenkunde*, 20:47, 1900.
- J Hartmann. Über ein neues Kameraobjektiv für spektrographen. *Zeitschrift für Instrumentenkunde*, 24:257–263, 1904.
- Xander KD Hillewaere and Filip E Du Prez. Fifteen chemistries for autonomous external self-healing polymers and composites. *Progress in Polymer Science*, 49:121–153, 2015.
- Takato Inoue, Satoshi Matsuyama, Shogo Kawai, Hirokatsu Yumoto, Yuichi Inubushi, Taito Osaka, Ichiro Inoue, Takahisa Koyama, Kensuke Tono, Haruhiko Ohashi, Makina Yabashi, Tetsuya Ishikawa, and Kazuto Yamauchi. Systematic-error-free wavefront measurement using an x-ray single-grating interferometer. *Review of Scientific Instruments*, 89(4):043106, 2018. doi: 0.1063/1.5026440.
- Torben Haugaard Jensen, Martin Bech, Irene Zanette, Timm Weitkamp, Christian David, Hans Deyhle, Simon Rutishauser, Elena Reznikova, Jürgen Mohr, Robert Feidenhans, et al. Directional x-ray dark-field imaging of strongly ordered systems. *Physical Review B*, 82(21):214103, 2010. doi: 10.1103/PhysRevB.82.214103.
- Sebastian Kaeppler, Florian Bayer, Thomas Weber, Andreas Maier, Gisela Anton, Joachim Hornegger, Matthias Beckmann, Peter A. Fasching, Arndt Hartmann, Felix Heindl, Thilo Michel, Gueluemser Oezguel, Georg Pelzer, Claudia Rauh, Jens Rieger, Ruediger Schulz-Wendtland, Michael Uder, David Wachter, Evelyn Wenkel, and Christian Riess. Signal decomposition for x-ray dark-field imaging. In Polina Golland, Nobuhiko Hata, Christian Barillot, Joachim Hornegger, and Robert Howe, editors, *International Conference on Medical Image Computing and Computer-Assisted Intervention*, pages 170–177. Springer, 2014. doi: 10.1007/978-3-319-10404-1\_22.
- Matias Kagias, Zhentian Wang, Pablo Villanueva-Perez, Konstantins Jefimovs, and Marco Stampanoni. 2d-omnidirectional hard-x-ray scattering sensitivity in a single shot. *Physical Review Letters*, 116(9):093902, 2016.
- Matias Kagias, Zhentian Wang, Mie Elholm Birckbak, Erik Lauridsen, Matteo Abis, Goran Lovric, Konstantins Jefimovs, and Marco Stampanoni. Diffractive small angle x-ray scattering imaging for anisotropic structures. *Nature communications*, 10(1):1–9, 2019.

- Nand Jee Kanu, Eva Gupta, Umesh Kumar Vates, and Gyanendra Kumar Singh. Self-healing composites: A state-of-the-art review. *Composites Part A: Applied Science and Manufacturing*, 121:474–486, 2019.
- MR Kessler. Self-healing: a new paradigm in materials design. *Proceedings of the Institution of Mechanical Engineers, Part G: Journal of Aerospace Engineering*, 221(4):479–495, 2007.
- Jisoo Kim, Matias Kagias, Federica Marone, and Marco Stampanoni. X-ray scattering tensor tomography with circular gratings. *Applied Physics Letters*, 116(13):134102, 2020.
- Jisoo Kim, Azat Slyamov, Erik Lauridsen, Mie Birckbak, Tiago Ramos, Federica Marone, Jens W Andreasen, Marco Stampanoni, and Matias Kagias. Macroscopic mapping of microscale fibers in freeform injection molded fiber-reinforced composites using x-ray scattering tensor tomography. *Composites Part B: Engineering*, 233:109634, 2022.
- F.J. Koch, F.P. O’Dowd, M.B. Cardoso, R.R. Da Silva, M. Cavicchioli, S.J.L. Ribeiro, T.J. Schröter, A. Faisal, P. Meyer, D. Kunka, and J. Mohr. Low energy x-ray grating interferometry at the brazilian synchrotron. *Optics Communications*, 393:195–198, 2017. doi: 10.1016/j.optcom.2017.02.055.
- Frieder Johannes Koch. *X-ray optics made by X-ray lithography*. PhD thesis, Karlsruhe Institute of Technology, 2017.
- Thomas Koenig, Marcus Zuber, Barbara Trimborn, Tomas Farago, Pascal Meyer, Danays Kunka, Frederic Albrecht, Sascha Kreuer, Thomas Volk, Michael Fiederle, et al. On the origin and nature of the grating interferometric dark-field contrast obtained with low-brilliance x-ray sources. *Physics in Medicine & Biology*, 61(9):3427, 2016.
- Maria Kosarli, Dimitrios G Bekas, Kyriaki Tsirka, Dimitrios Baltzis, Dimitrios T Vaimakis-Tsogkas, Savvas Orfanidis, Georgios Papavassiliou, and Alkiviadis S Paipetis. Microcapsule-based self-healing materials: Healing efficiency and toughness reduction vs. capsule size. *Composites Part B: Engineering*, 171:78–86, 2019.
- C Kottler, C David, F Pfeiffer, and O Bunk. A two-directional approach for grating based differential phase contrast imaging using hard x-rays. *Optics express*, 15(3):1175–1181, 2007.
- Martin Krenkel, Mareike Töpperwien, Christian Dullin, Frauke Alves, and Tim Salditt. Propagation-based phase-contrast tomography for high-resolution lung imaging with laboratory sources. *AIP Advances*, 6(3):035007, 2016.
- Danays Kunka, Jürgen Mohr, Vladimir Nazmov, Jan Meiser, Pascal Meyer, Maximilian Amberger, Frieder Koch, Joachim Schulz, Marco Walter, Thomas Duttonhofer, et al. Characterization method for new resist formulations for har patterns made by x-ray lithography. *Microsystem technologies*, 20(10-11):2023–2029, 2014.
- T-H Le, Pierre JJ Dumont, L Orgéas, D Favier, Luc Salvo, and Elodie Boller. X-ray phase contrast microtomography for the analysis of the fibrous microstructure of smc composites. *Composites Part A: Applied Science and Manufacturing*, 39(1):91–103, 2008.

- Alexander Letzel, Stefan Reich, Tomy dos Santos Rolo, Alexander Kanitz, Jan Hoppius, Alexander Rack, Margie P Olbinado, Andreas Ostendorf, Bilal Gökce, Anton Plech, et al. Time and mechanism of nanoparticle functionalization by macromolecular ligands during pulsed laser ablation in liquids. *Langmuir*, 35(8):3038–3047, 2019.
- Susanna K Lynch, Vinay Pai, Julie Auxier, Ashley F Stein, Eric E Bennett, Camille K Kemble, Xianghui Xiao, Wah-Keat Lee, Nicole Y Morgan, and Han Harold Wen. Interpretation of dark-field contrast and particle-size selectivity in grating interferometers. *Applied optics*, 50(22):4310–4319, 2011.
- Mingming Ma, Liang Guo, Daniel G Anderson, and Robert Langer. Bio-inspired polymer composite actuator and generator driven by water gradients. *Science*, 339(6116):186–189, 2013.
- A Malecki, G Potdevin, and F Pfeiffer. Quantitative wave-optical numerical analysis of the dark-field signal in grating-based x-ray interferometry. *EPL (Europhysics Letters)*, 99(4):48001, 2012.
- Andreas Malecki, Elena Eggl, Florian Schaff, Guillaume Potdevin, Thomas Baum, Eduardo Grande Garcia, Jan S Bauer, and Franz Pfeiffer. Correlation of x-ray dark-field radiography to mechanical sample properties. *Microscopy and Microanalysis*, 20(5):1528–1533, 2014.
- Giovanni Mana. Applications of x-ray interferometry in metrology and phase-contrast imaging. In *Seventh International Symposium on Laser Metrology Applied to Science, Industry, and Everyday Life*, volume 4900, pages 257–268. International Society for Optics and Photonics, 2002. doi: 10.1117/12.484565.
- CL Mangun, AC Mader, NR Sottos, and SR White. Self-healing of a high temperature cured epoxy using poly (dimethylsiloxane) chemistry. *Polymer*, 51(18):4063–4068, 2010.
- Timo Mappes, Sven Achenbach, and Juergen Mohr. Process conditions in x-ray lithography for the fabrication of devices with sub-micron feature sizes. *Microsystem technologies*, 13(3):355–360, 2007. doi: 10.1007/s00542-006-0182-3.
- Shashidhara Marathe, Lahsen Assoufid, Xianghui Xiao, Kyungmin Ham, Warren W Johnson, and Leslie G Butler. Improved algorithm for processing grating-based phase contrast interferometry image sets. *Review of Scientific Instruments*, 85(1):013704, 2014. doi: 10.1063/1.4861199.
- Sheridan Mayo, Andrew Stevenson, Stephen Wilkins, Da Chao Gao, Steven Mookhoek, Sam Meure, Tony Hughes, and James Mardel. X-ray phase-contrast tomography for quantitative characterisation of self-healing polymers. In *Materials Science Forum*, volume 654, pages 2322–2325. Trans Tech Publ, 2010.
- Sheridan C Mayo and Brett Sexton. Refractive microlens array for wave-front analysis in the medium to hard x-ray range. *Optics letters*, 29(8):866–868, 2004.
- Sheridan C Mayo, Andrew W Stevenson, and Stephen W Wilkins. In-line phase-contrast x-ray imaging and tomography for materials science. *Materials*, 5(5):937–965, 2012.

- Edwin C McCullough. Photon attenuation in computed tomography. *Medical Physics*, 2(6): 307–320, 1975.
- Erin A Miller, Timothy A White, Benjamin S McDonald, and Allen Seifert. Phase contrast x-ray imaging signatures for security applications. *IEEE Transactions on Nuclear Science*, 60(1): 416–422, 2013.
- Jürgen Mohr, Thomas Grund, Danays Kunka, Johannes Kenntner, Juerg Leuthold, Jan Meiser, Joachim Schulz, and Marco Walter. High aspect ratio gratings for x-ray phase contrast imaging. In *AIP Conference proceedings*, volume 1466, pages 41–50. American Institute of Physics, 2012. doi: 10.1063/1.4742267.
- Atsushi Momose. Phase-sensitive imaging and phase tomography using x-ray interferometers. *Optics express*, 11(19):2303–2314, 2003.
- Atsushi Momose, Shinya Kawamoto, Ichiro Koyama, Yoshitaka Hamaishi, Kengo Takai, and Yoshio Suzuki. Demonstration of x-ray talbot interferometry. *Japanese journal of applied physics*, 42(7B):L866, 2003.
- Steven D Mookhoek, Sheridan C Mayo, Anthony E Hughes, Scott A Furman, Hartmut R Fischer, and Sybrand Van der Zwaag. Applying sem-based x-ray microtomography to observe self-healing in solvent encapsulated thermoplastic materials. *Advanced engineering materials*, 12(3):228–234, 2010.
- Kaye S Morgan, David M Paganin, and Karen KW Siu. Quantitative single-exposure x-ray phase contrast imaging using a single attenuation grid. *Optics express*, 19(20):19781–19789, 2011. doi: 10.1364/OE.19.019781.
- Kaye S Morgan, David M Paganin, and Karen KW Siu. X-ray phase imaging with a paper analyzer. *Applied Physics Letters*, 100(12):124102, 2012. doi: 10.1063/1.3694918.
- N Morimoto, K Kimura, T Shirai, T Doki, S Sano, A Horiba, and K Kitamura. Talbot-lau interferometry-based x-ray imaging system with retractable and rotatable gratings for non-destructive testing. *Review of Scientific Instruments*, 91(2):023706, 2020. doi: 10.1063/1.5131306.
- Ramasamy Murugan, R Ramesh, and Krishan Padmanabhan. Investigation on static and dynamic mechanical properties of epoxy based woven fabric glass/carbon hybrid composite laminates. *Procedia Engineering*, 97:459–468, 2014.
- Gennadiy Nikishkov, Yuri Nikishkov, and Andrew Makeev. Finite element mesh generation for composites with ply waviness based on x-ray computed tomography. *Advances in Engineering Software*, 58:35–44, 2013.
- A. Olivo, F. Arfelli, G. Cantatore, R. Longo, R. H. Menk, S. Pani, M. Prest, P. Poropat, L. Rigon, G. Tromba, E. Vallazza, and E. Castelli. An innovative digital imaging set-up allowing a low-dose approach to phase contrast applications in the medical field. *Medical physics*, 28(8):1610–1619, 2001. doi: 10.1118/1.1388219.

- A Olivo, D Chana, and R Speller. A preliminary investigation of the potential of phase contrast x-ray imaging in the field of homeland security. *Journal of Physics D: Applied Physics*, 41(22):225503, 2008.
- Alessandro Olivo. Edge-illumination x-ray phase-contrast imaging. *Journal of Physics: Condensed Matter*, 33(36):363002, 2021.
- Alessandro Olivo and Robert Speller. A coded-aperture technique allowing x-ray phase contrast imaging with conventional sources. *Applied Physics Letters*, 91(7):074106, 2007. doi: 10.1063/1.2772193.
- Alessandro Olivo, Konstantin Ignatyev, Peter RT Munro, and Robert D Speller. Noninterferometric phase-contrast images obtained with incoherent x-ray sources. *Applied Optics*, 50(12):1765–1769, 2011.
- David Paganin et al. *Coherent X-ray optics*. Number 6. Oxford University Press on Demand, Oxford, United Kingdom, 2006.
- RH Pantell, J Feinstein, HR Beguiristain, MA Piestrup, CK Gary, and JT Cremer. The effect of unit lens alignment and surface roughness on x-ray compound lens performance. *Review of Scientific Instruments*, 72(1):48–52, 2001.
- Jae Man Park, Jong Hyun Kim, Jun Sae Han, Da Seul Shin, Sung Cheol Park, Seong Ho Son, and Seong Jin Park. Fabrication of tapered micropillars with high aspect-ratio based on deep x-ray lithography. *Materials*, 12(13):2056, 2019. doi: 10.3390/ma12132056.
- Biswajit Pathak and Bosanta R Boruah. Improved wavefront reconstruction algorithm for shack-hartmann type wavefront sensors. *Journal of Optics*, 16(5):055403, 2014.
- Konstantin M Pavlov, Heyang Thomas Li, David M Paganin, Sebastien Berujon, H el ene Roug e-Labriet, and Emmanuel Brun. Single-shot x-ray speckle-based imaging of a single-material object. *Physical Review Applied*, 13(5):054023, 2020.
- Georg Pelzer, Gisela Anton, Florian Horn, Jens Rieger, Andr e Ritter, Johannes Wandner, Thomas Weber, and Thilo Michel. A beam hardening and dispersion correction for x-ray dark-field radiography. *Medical physics*, 43(6Part1):2774–2779, 2016. doi: 10.1118/1.4948671.
- Sandeep S Pendhari, Tarun Kant, and Yogesh M Desai. Application of polymer composites in civil construction: A general review. *Composite structures*, 84(2):114–124, 2008.
- Franz Pfeiffer, Timm Weitkamp, Oliver Bunk, and Christian David. Phase retrieval and differential phase-contrast imaging with low-brilliance x-ray sources. *Nature physics*, 2(4):258–261, 2006.
- Franz Pfeiffer, Martin Bech, Oliver Bunk, Philipp Kraft, Eric F Eikenberry, Ch Br onnimann, Christian Gr unzweig, and Christian David. Hard-x-ray dark-field imaging using a grating interferometer. *Nature materials*, 7(2):134–137, 2008.

- Abdollah Pil-Ali, Sahar Adnani, Christopher C Scott, and Karim S Karim. Evaluation of edge-illumination and propagation-based x-ray phase contrast imaging methods for high resolution imaging application. In *Medical Imaging 2021: Physics of Medical Imaging*, volume 11595, page 115951N. International Society for Optics and Photonics, 2021. doi: 10.1117/12.2582225.
- Ben C Platt and Roland Shack. History and principles of shack-hartmann wavefront sensing, 2001.
- F Prade, A Yaroshenko, J Herzen, and F Pfeiffer. Short-range order in mesoscale systems probed by x-ray grating interferometry. *EPL (Europhysics Letters)*, 112(6):68002, 2016.
- Friedrich Prade, Florian Schaff, Sascha Senck, P Meyer, Jürgen Mohr, Johann Kastner, and Franz Pfeiffer. Nondestructive characterization of fiber orientation in short fiber reinforced polymer composites with x-ray vector radiography. *NDT & E International*, 86:65–72, 2017. doi: 10.1016/j.ndteint.2016.11.013.
- Zhi Qiao, Xianbo Shi, Michael J Wojcik, Luca Rebuffi, and Lahsen Assoufid. Single-shot x-ray phase-contrast and dark-field imaging based on coded binary phase mask. *Applied Physics Letters*, 119(1):011105, 2021. doi: 10.1063/5.0053553.
- S Ramakrishna, J Mayer, E Wintermantel, and Kam W Leong. Biomedical applications of polymer-composite materials: a review. *Composites science and technology*, 61(9):1189–1224, 2001.
- Armin Rashidi, Tina Olfatbakhsh, Bryn Crawford, and Abbas S Milani. A review of current challenges and case study toward optimizing micro-computed x-ray tomography of carbon fabric composites. *Materials*, 13(16):3606, 2020.
- Stefan Reich. *Hierarchical imaging of the dynamics during pulsed laser ablation in liquids*. PhD thesis, KIT-Bibliothek, 2019.
- Stefan Reich, Tomy dos Santos Rolo, Alexander Letzel, Tilo Baumbach, and Anton Plech. Scalable, large area compound array refractive lens for hard x-rays. *Applied Physics Letters*, 112(15):151903, 2018.
- André Ritter, Peter Bartl, Florian Bayer, Karl C Gödel, Wilhelm Haas, Thilo Michel, Georg Pelzer, Jens Rieger, Thomas Weber, Andrea Zang, et al. Simulation framework for coherent and incoherent x-ray imaging and its application in talbot-lau dark-field imaging. *Optics express*, 22(19):23276–23289, 2014.
- François Roddier and Claude Roddier. Wavefront reconstruction using iterative fourier transforms. *Applied Optics*, 30(11):1325–1327, 1991.
- Lucia Romano, Joan Vila-Comamala, Konstantins Jefimovs, and Marco Stampanoni. High-aspect-ratio grating microfabrication by platinum-assisted chemical etching and gold electroplating. *Advanced Engineering Materials*, 22(10):2000258, 2020. doi: 10.1002/adem.202000258.
- N Saba, MT Paridah, and M Jawaid. Mechanical properties of kenaf fibre reinforced polymer composite: A review. *Construction and Building materials*, 76:87–96, 2015.

- Timo Saha, Scott Rohrbach, Theo Hadjimichael, and William W Zhang. Wavefront sensing of x-ray telescopes. In *Space Telescopes and Instrumentation 2010: Ultraviolet to Gamma Ray*, volume 7732, pages 930–937. SPIE, 2010.
- Volker Saile, Ulrike Wallrabe, Osamu Tabata, and Jan G Korvink. *LIGA and its Applications*, volume 7. Wiley Online Library, Weinheim, Germany, 2009. doi: 10.1002/9783527622573.
- Margaret Scheiner, Tarik J Dickens, and Okenwa Okoli. Progress towards self-healing polymers for composite structural applications. *Polymer*, 83:260–282, 2016.
- Paul J Schilling, BhanuPrakash R Karedla, Arun K Tatiparthi, Melody A Verges, and Paul D Herrington. X-ray computed microtomography of internal damage in fiber reinforced polymer matrix composites. *Composites science and technology*, 65(14):2071–2078, 2005.
- Johannes Schindelin, Ignacio Arganda-Carreras, Erwin Frise, Verena Kaynig, Mark Longair, Tobias Pietzsch, Stephan Preibisch, Curtis Rueden, Stephan Saalfeld, Benjamin Schmid, et al. Fiji: an open-source platform for biological-image analysis. *Nature methods*, 9(7):676–682, 2012.
- Moreira Diego Schlemper and Henrique Sérgio Pezzin. Self-healing organic coatings based on microcapsules - a patent-based review. *Current Applied Polymer Science*, 4:175–189, 2021.
- Maria Seifert, Veronika Ludwig, Michael Gallersdörfer, Christian Hauke, Katharina Hellbach, Florian Horn, Georg Pelzer, Marcus Radicke, Jens Rieger, Sven-Martin Sutter, Thilo Michel, and Gisela Anton. Single-shot talbot-lau x-ray dark-field imaging of a porcine lung applying the moiré imaging approach. *Physics in Medicine & Biology*, 63(18):185010, 2018. doi: 10.1088/1361-6560/aadafe.
- Sascha Senck, Michael Scheerer, Vincent Revol, Katharina Dobes, Bernhard Plank, and Johann Kastner. Non-destructive evaluation of defects in polymer matrix composites for aerospace applications using x-ray talbot-lau interferometry and micro ct. In *58th AIAA/ASCE/AHS/ASC Structures, Structural Dynamics, and Materials Conference*, page 0355, 2017. doi: 10.2514/6.2017-0355.
- RM Sencu, Z Yang, YC Wang, PJ Withers, Christopher Rau, A Parson, and Constantinos Soutis. Generation of micro-scale finite element models from synchrotron x-ray ct images for multidirectional carbon fibre reinforced composites. *Composites Part A: Applied Science and Manufacturing*, 91:85–95, 2016.
- Roland V Shack. Production and use of a lecticular hartmann screen. *J. Opt. Soc. Am.*, 61:656–661, 1971.
- Anatoly Snigirev, Victor Kohn, Irina Snigireva, and Bruno Lengeler. A compound refractive lens for focusing high-energy x-rays. *Nature*, 384(6604):49–51, 1996.
- William H Southwell. Wave-front estimation from wave-front slope measurements. *JOSA*, 70(8): 998–1006, 1980.

- Wolfgang Stark, Matthias Jaunich, and Jarlath McHugh. Dynamic mechanical analysis (dma) of epoxy carbon-fibre prepregs partially cured in a discontinued autoclave analogue process. *Polymer Testing*, 41:140–148, 2015.
- Markus Strobl. General solution for quantitative dark-field contrast imaging with grating interferometers. *Scientific reports*, 4(1):1–6, 2014.
- Naxi Tian, Hui Jiang, Aiguo Li, Dongxu Liang, and Fucheng Yu. High-precision speckle-tracking x-ray imaging with adaptive subset size choices. *Scientific Reports*, 10(1):1–12, 2020. doi: 10.1038/s41598-020-71158-9.
- Jeroen Van Stappen, Tom Bultreys, Francisco A Gilabert, Xander KD Hillewaere, David Garoz Gómez, Kim Van Tittelboom, Jelle Dhaene, Nele De Belie, Wim Van Paepegem, Filip E Du Prez, et al. The microstructure of capsule containing self-healing materials: A micro-computed tomography study. *Materials Characterization*, 119:99–109, 2016.
- Joan Vila-Comamala, Lucia Romano, Vitaliy Guzenko, Matias Kagias, Marco Stampanoni, and Konstantins Jefimovs. Towards sub-micrometer high aspect ratio x-ray gratings by atomic layer deposition of iridium. *Microelectronic Engineering*, 192:19–24, 2018. doi: 10.1016/j.mee.2018.01.027.
- Joan Vila-Comamala, Lucia Romano, Konstantins Jefimovs, Hector Dejea, Anne Bonnin, Andrew C Cook, Ivo Planinc, Maja Cikes, Zhentian Wang, and Marco Stampanoni. High sensitivity x-ray phase contrast imaging by laboratory grating-based interferometry at high talbot order geometry. *Optics Express*, 29(2):2049–2064, 2021. doi: 10.1364/OE.414174.
- Fabio A Vittoria, Gibril KN Kallon, Dario Basta, Paul C Diemoz, Ian K Robinson, Alessandro Olivo, and Marco Endrizzi. Beam tracking approach for single-shot retrieval of absorption, refraction, and dark-field signals with laboratory x-ray sources. *Applied Physics Letters*, 106(22):224102, 2015. doi: 10.1063/1.4922189.
- Wanessa RK Weihermann, Marcia M Meier, and Sergio H Pezzin. Microencapsulated amino-functional polydimethylsiloxane as autonomous external self-healing agent for epoxy systems. *Journal of Applied Polymer Science*, 136(23):47627, 2019.
- Timm Weitkamp, Ana Diaz, Christian David, Franz Pfeiffer, Marco Stampanoni, Peter Cloetens, and Eric Ziegler. X-ray phase imaging with a grating interferometer. *Optics express*, 13(16):6296–6304, 2005a.
- Timm Weitkamp, Bernd Nöhammer, Ana Diaz, Christian David, and Eric Ziegler. X-ray wavefront analysis and optics characterization with a grating interferometer. *Applied Physics Letters*, 86(5):054101, 2005b. doi: 10.1063/1.1857066.
- Timm Weitkamp, Christian David, Oliver Bunk, Jens Bruder, Peter Cloetens, and Franz Pfeiffer. X-ray phase radiography and tomography of soft tissue using grating interferometry. *European journal of radiology*, 68(3):S13–S17, 2008. doi: 10.1016/j.ejrad.2008.04.031.

- Han Wen, Eric E Bennett, Monica M Hegedus, and Stefanie C Carroll. Spatial harmonic imaging of x-ray scattering—initial results. *IEEE transactions on medical imaging*, 27(8):997–1002, 2008.
- Harold H Wen, Eric E Bennett, Rael Kopace, Ashley F Stein, and Vinay Pai. Single-shot x-ray differential phase-contrast and diffraction imaging using two-dimensional transmission gratings. *Optics letters*, 35(12):1932–1934, 2010.
- Scott R White, Nancy R Sottos, Philippe H Geubelle, Jeffrey S Moore, Michael R Kessler, SR Srim, Eric N Brown, and S Viswanathan. Autonomic healing of polymer composites. *Nature*, 409(6822):794–797, 2001.
- SW Wilkins, Ya I Nesterets, TE Gureyev, SC Mayo, A Pogany, and AW Stevenson. On the evolution and relative merits of hard x-ray phase-contrast imaging methods. *Philosophical Transactions of the Royal Society A: Mathematical, Physical and Engineering Sciences*, 372(2010):20130021, 2014.
- Johannes Wolf, Jonathan I Sperl, Florian Schaff, Markus Schüttler, Andre Yaroshenko, Irene Zanette, Julia Herzen, and Franz Pfeiffer. Lens-term-and edge-effect in x-ray grating interferometry. *Biomedical optics express*, 6(12):4812–4824, 2015.
- Dong Yang Wu, Sam Meure, and David Solomon. Self-healing polymeric materials: A review of recent developments. *Progress in polymer science*, 33(5):479–522, 2008.
- Grace X Gu, Isabelle Su, Shruti Sharma, Jamie L Voros, Zhao Qin, and Markus J Buehler. Three-dimensional-printing of bio-inspired composites. *Journal of biomechanical engineering*, 138(2), 2016.
- Yang Yang, Lei Gao, Jiaye Xie, Yao Zhou, Jun Hu, Qi Li, and Jinliang He. Defect-targeted self-healing of multiscale damage in polymers. *Nanoscale*, 12(6):3605–3613, 2020.
- Yi Yang and Xiangyang Tang. The second-order differential phase contrast and its retrieval for imaging with x-ray talbot interferometry. *Medical physics*, 39(12):7237–7253, 2012.
- Wataru Yashiro and Atsushi Momose. Effects of unresolvable edges in grating-based x-ray differential phase imaging. *Optics express*, 23(7):9233–9251, 2015.
- Wataru Yashiro, Y Terui, K Kawabata, and A Momose. On the origin of visibility contrast in x-ray talbot interferometry. *Optics express*, 18(16):16890–16901, 2010.
- Z Yousaf, P Potluri, F Léonard, and PJ Withers. Meso scale analysis of 2d glass woven preforms under compaction. *ICCM19, Montreal, Canada*, pages 1–8, 2013.
- B Yu, RS Bradley, C Soutis, and PJ Withers. A comparison of different approaches for imaging cracks in composites by x-ray microtomography. *Philosophical Transactions of the Royal Society A: Mathematical, Physical and Engineering Sciences*, 374(2071):20160037, 2016.

- 
- Margarita Zakharova, Vitor Vlnieska, Heike Fornasier, Martin Börner, Tomy dos Santos Rolo, Jürgen Mohr, and Danays Kunka. Development and characterization of two-dimensional gratings for single-shot x-ray phase-contrast imaging. *Applied Sciences*, 8(3):468, 2018.
- I Zanette, Tunhe Zhou, Anna Burvall, Ulf Lundström, Daniel H Larsson, M Zdora, P Thibault, Franz Pfeiffer, and Hans M Hertz. Speckle-based x-ray phase-contrast and dark-field imaging with a laboratory source. *Physical review letters*, 112(25):253903, 2014. doi: 10.1103/PhysRevLett.112.253903.
- Irene Zanette, Timm Weitkamp, Tilman Donath, Simon Rutishauser, and Christian David. Two-dimensional x-ray grating interferometer. *Physical review letters*, 105(24):248102, 2010. doi: 10.1103/PhysRevLett.105.248102.
- Cui Zhang, Xiaodong Pan, Hongjie Shang, and Gongping Li. Alternative edge illumination set-up for single-shot x-ray phase contrast imaging. *Journal of Applied Physics*, 124(16):164906, 2018. doi: 10.1063/1.5040062.
- Tunhe Zhou, Hongchang Wang, and Kawal Sawhney. Single-shot x-ray dark-field imaging with omnidirectional sensitivity using random-pattern wavefront modulator. *Applied Physics Letters*, 113(9):091102, 2018.